

ACETALDEHYDE ADSORPTION ON ACTIVATED CARBONS

Yehya El-Sayed, and Teresa J. Bandoz

Department of Chemistry, the City College of New York and the Graduate School of the City University of New York, 138th street and Convent Ave, New York, NY 10031; e-mail: tbandosz@ccny.cuny.edu

Introduction

One of the applications of activated carbons in purification processes is removal of odoriferous substances from air [1]. Nowadays each car contains at least one activated carbon filter to adsorb such environmental dangerous species as gasoline vapors. Moreover, filters installed in clean rooms contain activated carbon adsorbents to remove odors. The odor causing compounds may be removed by several mechanisms. For example, the odor causing substance can chemically react with the surface and form a non odoriferous and /or non volatile compound or be sorbed. For a sorbent to be effective for deodorizing, especially for compounds with very low olfactory thresholds, it is essential to be capable of removing, in its environment, virtually all the odoriferous compounds regardless of the concentration of the compound. Thus, the sorbent must be able to sorb an odoriferous compound when it is present in even trace amounts. It also must be able to retain the sorbed odoriferous compound at even close to saturation conditions.

Adsorption of formaldehyde on activated carbons was studied by of Domingo-Garcia et al. [2]. They found that formaldehyde is strongly adsorbed with isosteric heat between 15-33 kJ/mol. The retention volumes obtained in that study increased with an increase in the surface areas of activated carbons.

The objective of this study is to evaluate which features of activated carbon surfaces are important for adsorption of acetaldehyde. The evaluation is based on the values of isosteric heats of adsorption, which reflect the strength of molecule interaction with activated carbon surface. Since the experiments are done at infinite dilution the results are helpful to assess the performance of adsorbents when only traces of molecules to be removed are present in air. Another quantity analyzed is amount adsorbed at saturation conditions.

Experimental

Materials. Three activated carbons were chosen for this study. They are as follows: BPL (Calgon, bituminous coal origin), MVP (Norit, bituminous coal origin), and BAX (Westvaco-wood origin, chemical activation with phosphoric acid). Before experiments, the initial carbons were washed in a Soxhlet apparatus to remove water-soluble species. The samples were oxidized with nitric acid (10 grams of the initial sample were oxidized with 100 ml of 15 N HNO₃ for 24 hours). Then washing in a Soxhlet apparatus was done to remove excess oxidizing agent and water-soluble compounds. After this process the samples are referred to as BPL-O, MVP-O and BAX-O. For comparison carbon black, carbopack, supplied by Suppelco was also used as an adsorbent of acetaldehyde.

Methods. The chromatographic experiments were performed with an SRI gas chromatograph equipped with a flame ionization detector with helium as a carrier gas. The range of experimental temperatures was: 313-473K (20 K step).

The basic quantity determined from IGC experiment is the net retention volume, V_N . It is calculated from the retention time using the flow rate of the carrier gas and compressibility correction factor [17, 18].

The isosteric heat of adsorption Q_{st} at zero surface coverage can be found from the measurements of V_N at various temperatures using the expression

$$Q_{st} = R \frac{\partial \ln \frac{V_N}{T}}{\partial \frac{1}{T}}$$

The standard enthalpy of adsorption, $\Delta H^\circ = -Q_{st}$.

To evaluate amount adsorbed at saturation conditions a beaker with 10 mL of acetaldehyde was placed in a dessicator along with several 10 mL weighting dishes containing 1g of powdered carbon samples. The samples were kept in the atmosphere saturated with acetaldehyde vapors for 13 days (vapor pressure of acetaldehyde at 293 K is equal to 760 torr).

Nitrogen adsorption isotherms were measured using an ASAP 2010 analyzer at -193 °C. Before the experiment the samples were degassed at 120 °C to constant pressure of 10⁻⁵ torr. The isotherms were used to calculate the specific surface area, S_{N_2} ; micropore volume, V_{mic} , total pore volume, V_t , and pore size distributions (PSDs).

To evaluate the surface pH a 0.4 g sample of dry adsorbent was added to 20 mL of deionized water and the suspension stirred overnight to reach equilibrium. The sample was filtered and the pH of solution was measured using an Accumet Basic pH meter.

Thermal analysis was carried out using TA Instruments Thermal Analyzer. The heating rate was 10 deg/min in a nitrogen atmosphere at 100 mL/min flow rate.

Results and Discussion

At infinite dilution small molecules will adsorb in the smallest pores of activated carbons. The values of the surface areas and pore volumes calculated from the nitrogen adsorption isotherms using DFT [3] are collected in Table 1. It is clearly seen that BAX has the higher surface area due to the largest pore volume. In the case of PBL these parameters are the smallest. After oxidation the volumes of pores for BAX and MVP carbons decreased. This decrease is the most pronounced for the BAX-O sample. In the case of this carbon the total pore volume decreased almost threefold. In the case of BPL the structural parameters are not altered significantly.

Table 1. Structural Parameters calculated from nitrogen adsorption isotherms using DFT

Sample	S_{DFT} [m ² /g]	$V_{(DFT)}$ [cm ³ /g]	$V_{<20\text{\AA}}$ [cm ³ /g]	S_{BET} [m ² /g]
BAX	1370	1.339	0.528	2266
BAX-O	873	0.521	0.362	1105
BPL	764	0.376	0.319	901
BPL-O	810	0.404	0.337	938
MVP	838	0.483	0.355	1061
MVP-O	723	0.365	0.300	813

Based on the analysis of PSDs, the BPL sample is the microporous one whereas BAX has a significant contribution of mesopores. The MVP carbon has a porous structure placed between those of BPL and BAX. Based on this, we expect that energetics of acetaldehyde adsorption will also differ.

Oxidation also affects surface chemistry [4, 5]. After treatment with nitric acid the pH decreased, especially for BAX-O, as a result of the introduction of oxygen-containing groups.

All of the above-described differences in the carbons studied, and changes after oxidation should affect the adsorption of acetaldehyde. Acetaldehyde is a small molecule with chemical formula CH₃CH = O. Its van der Waals diameter is around 3.8 Å [6].

Due to the presence of aldehyde groups it is able to interact with oxygen containing groups on the surface via hydrogen bonding. Moreover, acetaldehyde should also interact in a dispersive way via hydrocarbon moiety with basal plane of carbons [7]. These interactions should reflect on the values of isosteric heats of adsorption (Table 2). Comparison of two significantly different samples, BPL and BAX, indicate the differences in the mechanism of adsorption. The heat of acetaldehyde adsorption on BAX is about 8 kJ greater than that for BPL. In fact the comparison of PSDs indicates that the smaller pores, and in a higher volume, are present in the BPL carbon, which leads to the higher heat of adsorption than that for BAX. The reverse results suggest that in the case of the wood based carbon the oxygen containing groups present on the surface contribute to the energetic of the process. We expect the heat of acetaldehyde adsorption on activated carbon to be in the range of 33-51 kJ/mol [2, 7]. Indeed, the values reported in Table 2 are in the expected range. When contribution of hydrogen bonding exists, the heat should be even greater of about 10 kJ/mol [7]. In such a situation hydrogen bonding between aldehyde group and functional groups on the carbon surface and aldehyde-aldehyde functional groups can be formed. For comparison, the heat of acetaldehyde adsorption on graphitized carbon black was found to be equal to 25.8 kJ/mol suggesting that on microporous activated carbons the heat should be around 52 kJ/mol.

Table 2. Heats of acetaldehyde adsorption on the carbons studied [kJ/mol].

Sample	Q_{st}
BAX	69.4
BAX-O	32.4
BPL	61.6
BPL-O	50.3
MVP	51.2
MVP-O	35.9

The presence of functional groups in the very small pores of carbons results in a decrease in the heat of adsorption. This is due to the weaker interactions of hydrocarbon moiety with the sorbent matrix. Another reason for the decrease may be in inaccessibility of very small pores to acetaldehyde molecule. If functional groups are located at the edge of graphite-like layers their high density may result in blocking the smallest pores for adsorptive molecule. The observed decrease in the heat of acetaldehyde adsorption for BPL carbon after oxidation may also be related to inaccessibility of pores, combined with higher density of acidic groups. This is supported by the fact that in the case of this carbon the pore structure is left almost intact after oxidation.

One can see an apparent discrepancy between the explanation of a decrease in the heat of adsorption and the results obtained from adsorption of nitrogen. When N_2 is adsorbed the amount of adsorbate is much greater than in our IGC experiment. Moreover, nitrogen covers much larger range of pore sizes than acetaldehyde does at infinite dilution. All of these causes that the nitrogen adsorption is affected less by the oxidation process.

Interesting results were obtained when the adsorption of acetaldehyde at saturation conditions was analyzed. Figure 1 visualizes the differences between the carbon before and after acetaldehyde adsorption. On the curves two well-defined peaks are present at about 400 and 450 K with various intensities. The intensity of the first peak increased for all carbons after oxidation whereas the intensity of the second peak is almost constant. Taking into account the changes in carbons' structure and surface chemistry it is likely that the first peak represents weaker adsorption of acetaldehyde via

hydrogen bonding on functional groups. The second peak is related to adsorption in small pores via dispersive interactions. After oxidation this peak is almost unchanged for BPL and MVP carbons. In the case of BAX the most pronounced decrease in intensity of the second peak is noticed which may be related to the partial destruction of the micropore structure of this carbon.

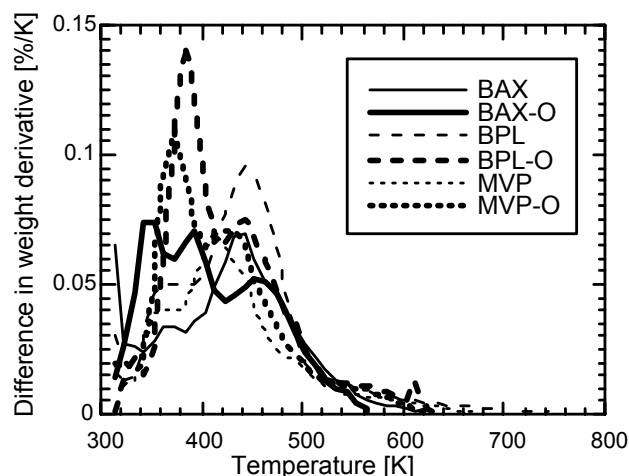


Figure 1. Difference in DTG curves for carbons after and before acetaldehyde adsorption.

Conclusions

The results presented in this paper show that the adsorption of acetaldehyde on activated carbons depends strongly on the pore size distributions of adsorbents and their surface chemistry. When very small pores, close to the size to acetaldehyde molecule, and oxygen containing groups are present (to certain extent) the heat of adsorption reaches its maximum value. Small density of surface groups can enhance the heat of adsorption whereas extensive oxidation leads to a decrease in the strength of adsorption forces. This happens due to the blocking of the pore entrances with functional groups and a decrease in the accessibility of hydrophobic surface where the dispersive interactions of hydrocarbon moiety with small pore walls can be enhanced. Oxidation of carbon surfaces results in an increase in the amount of acetaldehyde adsorbed at saturation conditions.

References

- (1) Bansal, R. C.; Donnet, J. B.; Stoeckli, F. *Active Carbon*, Marcel Dekker, New York, 1988.
- (2) Domingo-Garcia, M.; Fernandez-Morales, F.J.; Lopez-Garzon, F.J.; Moreno-Castilla, C.; Perez-Mendoza, M. *Langmuir* **1999**, *15*, 3226
- (3) Olivier, J.P. *J. Porous Materials* **1995**, *2*, 9.
- (4) Leon y Leon, C. A.; Radovic, L. R. In *Chemistry and Physics of Carbon*, Thrower, P. A. Ed.; Dekker, New York, 1992.
- (5) Bandosz, T. J.; Jagiello, J.; Contescu, C.; Schwarz, J. A. *Carbon* **1993**, *31*, 1193.
- (6) Handbook of Chemistry and Physics, Weast, R.C. Ed., CRC Press, 62nd edition, Boca Raton, FL, 1981.
- (7) Avgul, N. N.; Kiselev, A. V. In *Chemistry and Physics of Carbon*, Walker, P. J., Jr., Ed.; Dekker, New York, 1970.

APPLICATION OF DOEHLERT DESIGN TO OPTIMISE THE PREPARATION OF A NEW ACTIVATED CARBON

Baçaoui*, K. Nyazi*, A. Yaacoubi*, A. Dahbi*, C. Bennouna*,
F.J. Maldonado-Hodar**, J. Rivera-Utrilla**,
F. Carrasco-Marín** and C. Moreno-Castilla**

* Université Cadi Ayyad, Faculté des Sciences-Semlalia,
Département de Chimie, B.P. 2390 Marrakech, Maroc

** Departamento de Química Inorgánica, Facultad de Ciencias,
Universidad de Granada, 18071 Granada, Spain

Introduction

Previous papers¹⁻³ have reported that olive-waste cake is an excellent precursor for the production of activated carbon. Indeed, these activated carbons have proved more effective to adsorb pollutants contained in drinking water and to decolorize sugar syrup than have some commercial activated carbons.

The main objective of the present paper is to obtain activated carbons from olive-waste cakes, which are abundant waste materials in Morocco and Spain, by means of a one-step method, which combines the above two steps (carbonization and activation) in one step, consisting of the pyrolysis of the raw material at high temperature in a steam flow.

Once the activated carbons were obtained, they were characterized, and we investigated the optimal experimental conditions required to prepare activated carbons suitable for use as adsorbents to remove pollutants from water. These results were compared with those obtained for both activated carbons obtained by the two-step method and a commercial activated carbon used by the National Office of Drinking Water (ONEP) in Morocco.

Experimental

Raw material. Olive-waste cakes were obtained from olive oil processing.

Activated carbon preparation. The activation of the raw material was done in a thermolyne silica electric oven. The steam flow was $140 \text{ cm}^3 \text{ min}^{-1}$. The activation temperatures were between 750°C and 850°C and the activation times between 30 and 80 min.

Adsorption tests from aqueous solutions. The adsorption capacities of the carbon samples for methylene blue (Y_2) and iodine (Y_3) were calculated applying the Langmuir equation⁴. The methylene blue were dosed spectrophotometrically at 680 nm. The iodine concentrations were determined using the sodium thiosulfate volumetric method.

Response Surface Methodology. The analysis was achieved by response surface methodology, which gave satisfactory results⁵⁻⁷. Each response (Y) can be described by a second order model adequate to predict responses in all experimental regions:

$$Y = a_0 + a_1X_1 + a_2X_2 + a_{11}X_1^2 + a_{22}X_2^2 + a_{12}X_1X_2$$

where X_1 is the coded variable related to the natural variable U_1 (activation temperature) and X_2 is related to the natural variable U_2 (activation time). Values for the coefficients "a" are chosen so that the model fits the experimental data as closely as possible.

Results and discussion

The responses studied were the total yield in the activated carbon preparation (Y_1), the capacity of the activated carbon to adsorb methylene blue (Y_2) and iodine (Y_3). The choice of these parameters was based on their characteristics. The methylene blue test can be used to predict organic compound adsorption and is a simple method for screening for a specific carbon in water treatment. The iodine adsorption test indicates the total surface area of the carbon and is also a performance indicator for water treatment applications⁸.

Response analysis and interpretation. Following the model established for each response, we can represent graphically the surface of the corresponding responses. The values of the

coefficients provide information on the influence of the factors and the curves obtained show the extreme, or at least privileged, directions (zones of interest of the factors).

Total yield (Y_1). Analysis of this response (**Figure 1.**) showed that at low activation temperatures, the increase in activation time from 30 to 80 min induces little variation in the total yield. In contrast, at high activation temperatures, the increase in activation time produced a major reduction in yield. These results indicate that the gasification rate of olive-waste cakes with steam is very low at low temperatures (around 750°C) and high at high temperatures (around 850°C).

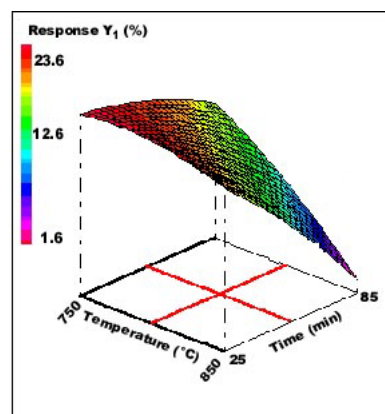


Figure 1. Variation of total yield (Y_1 , %) as a function of X_1 and X_2 .

Adsorption capacity of methylene blue (Y_2) and iodine (Y_3). As shown in **Figure 2**, the capacity of the carbon samples to adsorb methylene blue (Y_2) and iodine (Y_3) is highly dependent on the activation temperature (X_1) and time (X_2) used to prepare the carbon samples.

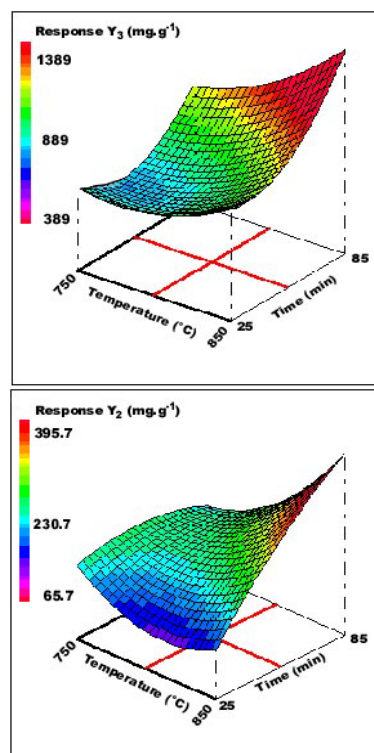


Figure 2. Variation of the adsorption capacity, mg g^{-1} , of activated carbon, as a function of X_1 and X_2 . a) Methylene blue (Y_2); b) Iodine (Y_3).

The effect of activation time on these characteristics is noticeable only at high activation temperatures, especially in the case of methylene blue adsorption.

Thus, at activation temperatures below 770 °C the activation time did not affect the capacity of the carbon sample to adsorb this compound, whereas at high activation temperatures, a small increase in activation time brings about a major increase in methylene blue adsorption. At high temperatures, the activation reaction of the olive-waste cakes may take place rapidly producing a development of the porosity of the activated carbon obtained, and, therefore, an increase in its capacity to adsorb methylene blue (**Figure 2.a**) and iodine (**Figure 2.b**).

Optimization. The main objective of the optimization was to determine the optimal conditions of activated temperature and residence time for the preparation of active carbons from olive waste cakes in one step. Because this material will be used in the process of drinking water treatment, it was necessary to establish domains of variation of each response in relation to the activate carbon characteristics required.

From an economical point of view, the total yield of the process (Y_1) is a positive parameter. The total yield of 10 - 20% is compares well with the average yield of 8% in the industrial sector.

With respect to quality characteristics (Y_1 and Y_2), we established a range of variation for these two responses of 180 - 450 mg/g for methylene blue and 900 - 1450 mg/g for iodine.

The optimization of a process depends on a number of constraints. In the present study, the objective was to enhance the yield in the manufacture of an activated carbon of given characteristics. These requirements cannot be differentiated in the interest zones of the factors. Thus, it is difficult to optimise all responses under the same conditions because the interest region of factors is different. Indeed, when Y_1 increases, the other two responses (Y_2 and Y_3) decrease. This situation led us to seek a compromise (domain depicted in **Figure 3**) between the quality and quantity of the active carbon prepared. It can be observed that there is an extensive range of both temperature and time of activation in which activated carbons with the required characteristics can be obtained.

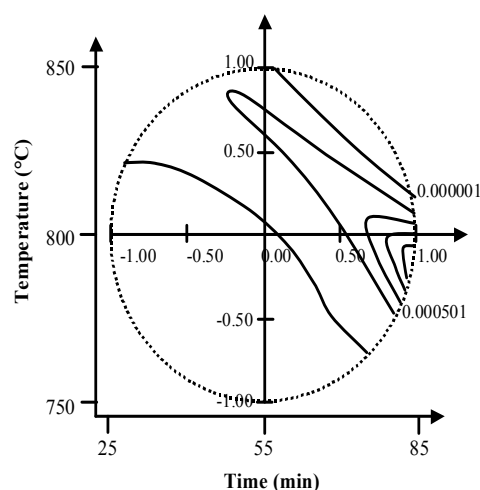


Figure 3. Domain of compromise

The optimal point indicated by the model corresponds to a temperature of 785°C and a residence time of 85 min (**Figure 3**). The response values of the carbon calculated from the model for these experimental conditions are given in **Table 3** (Sample AC-1). In order to test the validity of the results, an activated carbon sample (optimal activated carbon) was obtained at these experimental conditions following the one step

method (Sample AC-1) and its characteristics (Y_1 , Y_2 and Y_3), were experimentally determined (**Table 3**). The experimental values of these parameters show a good agreement with those calculated from the model.

Table 3 also shows the calculated and experimental response values of the “optimal” activated carbon obtained by two steps³ (Sample AC-2) and the experimental response values of the activated carbon AC-ONEP. Comparing the responses of these “optimal” activated carbons, it is clear that carbon obtained by the two-step method has a greater capacity to adsorb methylene blue (Y_2) and iodine (Y_3) than those obtained by the one-step method. Both of these activated carbons showed higher values of Y_2 and Y_3 than those of the commercial activated carbon AC-ONEP.

Table 3. Calculated and experimental response values corresponding to a compromise between Y_1 , Y_2 and Y_3 for the “optimal” activated carbons

Activated carbon	Responses	Y_1 (%)	Y_2 (mg g ⁻¹)	Y_3 (mg g ⁻¹)
AC-1	Calculated	15.5	288	1116
	Experimental	15.1	268	1125
AC-2	Calculated	16.2	433	1422
	Experimental	15.8	426	1390
AC- ONEP	Experimental		250	1100

Acknowledgement

This work was supported by PARS (Projet Chimie52 du Programme d'Appui à la Recherche Scientifique, Maroc) and the Agencia Española de Cooperación Internacional and the MCT-DGI (Project: PPQ2001-3246-C02-01).

REFERENCES

- (1) Bacaoui, A., Yaacoubi, A., Dahbi, A., Bennouna, C., Ayele, J., Mazet M. *J. Water SRT-Aqua* **1998**, 47(2), 68.
- (2) Bacaoui, A., Yaacoubi, A., Dahbi, A., Bennouna, C., Ayele, J., Mazet, M. *Environmental Technogy* **1998**, 19, 1203.
- (3) Bacaoui, A., Yaacoubi, A., Dahbi, A., Bennouna, C., Phan Tan Luu, R., Maldonado-Hodar, F.J., Rivera-Utrilla, J., Moreno-Castilla, C. *Carbon* **2001**, 39, 425.
- (4) Stumm, W., Morgan J.J., “Aquatic Chemistry”, Wiley, 2nd Ed. New York, **1981**.
- (5) Langer T., Köpsel R., Kuchling T. and Klose E., *Fuel*, **1989**, 68, 361.
- (6) Salhi N., Bennouna C., Bitar H., Sergeant M., Phan Tan Luu R., *Quimica Analitica*, **1997**, 16, 67.
- (7) Wachter R., Cordery A., *Carbon*, **1999**, 37, 1529.
- (8) AWWA Standard of Powder activated carbon, **1990** B600-90.

ASSEMBLY MECHANISMS IN MESOPHASE-BASED CARBON MATERIALS

Robert Hurt[†], Gernot Krammer^{††}, Gregory Crawford[†],
Kengqing Jian[†], Christopher Rulison^{†††}

[†] Brown University, Providence, RI, 02912 USA

^{††} Technical University of Graz, Graz Austria

^{†††} Kruss, USA, Charlotte, North Carolina

Introduction

Fullerenes, carbon blacks, glassy carbons, and many other carbon forms have outer surfaces rich in graphene basal planes¹. An alternative carbon form with “inverted” crystal structure is found in some carbons prepared by controlled heat treatment of condensed phase precursors that pass through a fluid state^{2,3} (see Fig. 1). The fundamental molecular assembly principles that govern structure selection in these carbon forms not completely understood, although it is clear that the inverted form involves discotic polyaromatic compounds as liquid crystalline intermediate phases^{2,3}. Here we present a basic investigation of the molecular orientation of large polyaromatic molecules on a variety of interfaces (“surface anchoring⁴) and of wetting behavior that provides information on interfacial energies. The results are used to understand the assembly mechanisms of large PAH and to identify the mechanism that selects concentric vs. bipolar structures in carbon spheres.

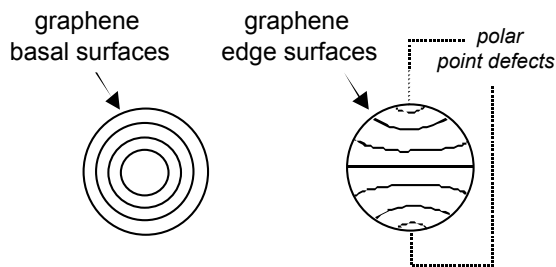


Figure 1. Two classes of crystal symmetries in carbon bodies. Lines are drawn parallel to aromatic planes or graphene layers. Left: concentric symmetry of “closed” carbon forms: carbon black, nested fullerenes. Right: bipolar symmetry of Brooks-Taylor carbon spheres with “inverted” crystal structure.

Experimental

Experiments were conducted with the naphthalene homopolymer AR mesophase (Mitsubishi Gas Chemical, HP grade). AR has molecular weights from 200-1400 Daltons with an MW distribution peak about 600 Daltons⁵. It has a C/H atomic ratio of 1.6, and softens at 280-350 °C to form a homogeneous discotic liquid crystalline phase. The AR liquid surface tension was measured by the pendent drop method at 325 °C in N₂ using the Kruss DSA10 drop shape analysis system. Surface anchoring states (see Fig. 2) were determined experimentally by coating molten AR films onto transparent, removable, or etchable substrates followed by direct microscopic examination of the interface. Edge-on and face-on anchoring states were identified through the presence or absence of optical anisotropy at the interface respectively. AR contact angles were measured at 325 °C in N₂ also using the DSA10. The same set of solid surfaces were characterized for surface energy and its dispersive and polar components by application of the standard Owens-Wendt theory⁶ to contact angles of standard reference liquids (diiodomethane and water) measured by the Schultz technique.

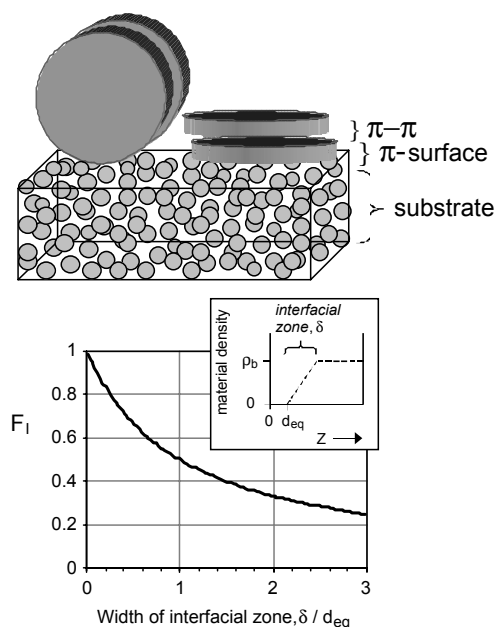


Figure 2. Edge-on and face-on anchoring states in discotic liquid crystals. Sketch shows the geometric mismatch responsible for inhibited dispersion upon anchoring at an amorphous solid surface. Graph gives inhibition factor, F_l , for face-on disks as a function of the degree of surface irregularity expressed as a width of the interfacial zone. This model calculation assumes linear density profile in the interfacial zone (shown in inset) and an inverse square dependence of Lennard-Jones forces between two infinite slabs.

Results and Discussion

We observe polyaromatic molecules in AR mesophase to anchor edge on at the free surface (gas interface) in agreement with White⁷, a result that indicates the edge-on plane in mesophase has a lower surface free energy than the face-on (basal) plane. Similar edge-on orientation is observed on most of the substrates examined: borosilicate glass, aluminum, copper, indium tin oxide, quartz, sapphire, and PTFE. The sole exception to this trend is the basal plane of highly oriented pyrolytic graphite (HOPG), which produces a liquid interface that is featureless and directionally invariant, indicating strict face-on orientation of the disk-like molecules.

Measured values of polyaromatic liquid (AR) surface tension and its contact angle on various substrates are reported in Table 1. Several features of this data are anomalous. First, a standard assignment of liquid polarity derived by applying the Fowkes theory⁸ to the surface tension and contact angle on non-polar PTFE yields a dispersive component of 20 mJ/m² and by difference a polar component of 7.2 mJ/m² (26% of the total). This apparent 26% polarity is quite surprising in light of the purely hydrocarbon nature of this liquid (C,H > 99 wt-%, O = 0.33 wt-%). A further aspect of the anomalous wetting behavior is the increase in contact angle as substrate surface energy increases from 65 to 78 mJ/m² in Table 1. This increase is inconsistent with the notion of a polar component in these liquids, and is also inconsistent with the general practice of surface treatment in composite fillers, used to increase surface energy and thus enhance filler/matrix adhesion. Quantitative treatment of the wetting data set shows it to be inconsistent with the Owens-Wendt theory⁶, which predicts complete wetting ($\theta=0$) of all surfaces but PTFE. In general AR exhibits an weaker interaction with surfaces than is predicted by common interfacial theories.

Table 1. Surface Energies and AR Contact Angles

substrate	surface dispers. energy [†]	dispers. part [†]	polar part [†]	contact angle	inhib. factor	effective disp. energy
				degrees	F_I	$F_I^2 \gamma_s^d$
PTFE	18	18	0	66.5	0.86	13.3
Borosilic. glass	67.5	33.9	33.6	26.8	0.84	23.9
Aluminum	72.4	34.6	37.8	35.9	0.80	22.1
Iron	72.5	33.8	38.7	37.0	0.80	21.6
Bisque alumina	78.0	33.1	44.9	40.6	0.79	20.6

[†] bare-solid surface energies and their components in mJ/m²;

A π - π -Bond Theory of Wetting, Anchoring, and Assembly

We propose that both the poor wetting and the favored edge-on anchoring state are the result of strong non-covalent face-face interactions involving aromatic π clouds — so-called “ π - π interactions”⁹. Aromatic π - π interactions are of intense interest for their role in molecular recognition, DNA base pair interactions, the tertiary structure of proteins, and a host of other phenomena⁹. Critical examination of this literature indicates that in the absence of strongly electron donating or withdrawing groups, π - π interactions are dominated by dispersion and quadrupolar forces, the latter being responsible for the tilted and offset arrangements in smaller molecules¹². Charge transfer or orbital overlap affects electrical conductivity in π - π stacks¹⁰, but does not typically determine overall energy or configuration in the absence of very strong electron donating or withdrawing groups^{9,11}. As molecular size increases, the dispersion forces prevail over the weak quadrupolar forces, producing face-to-face stacking with only slight offset among large molecules, as confirmed experimentally by TEM studies of polyaromatic liquids and young carbon solids².

The distinctive structural feature of large polyaromatics is extended molecular planarity, gives rise to a high area-density of dispersive centers for interaction with adjacent atomic planes. In the case of face-on anchoring, atomic-scale surface irregularity many carbon atoms from achieving the optimal interatomic distances across the interface (see Fig. 2). This geometric effect can be expected on all solids except crystals cleaved along planes of high atomic surface density (graphite, mica). In the edge-on state, the disk/surface interactions are also limited by the fixed geometry of the solid surface, which would rarely conform closely to the circular geometry of large, edge-on disks. Here we describe interfacial energies for non-polar liquids with the classical approach modified to account for geometric mismatch:

$$\gamma_{sl}(\theta) = \gamma_s + \gamma_l(\theta) - 2F_I(\theta) \sqrt{\gamma_s^d \gamma_l^d(\theta)} \quad (1)$$

where F_I is an inhibition factor. For the particular example of face-on anchored disks F_I is governed by the atomic irregularity:

$$F_I = \frac{(\sum \sum U_{ij}(r_{ij}))}{(\sum \sum U_{ij}(r_{ij}))} \quad (2)$$

where i and j are dispersion centers in the liquid and solid, respectively. Figure 2 shows that the total dispersion energy falls off very sharply with increasing irregularity, and the inhibition is significant even when the sparse interfacial zone is thinner than one interatomic distance in the bulk solid

Table 1 shows inhibition factors calculated from the wetting data using Eq. 1 and the classical Young equation. Minimizing interfacial free energy, $\gamma_{sl}(\theta)$, in Eq. 1 results in a particularly simple and insightful anchoring criterion: If $F_I^2 \gamma_s^d < \gamma_l$, then interfacial energy effects favors face-on anchoring, and if $F_I^2 \gamma_s^d > \gamma_l$, then interfacial energies favor edge-on anchoring. The criterion introduces the quantity $F_I^2 \gamma_s^d$ as an effective solid surface energy for the inhibited dispersion interaction with large rigid, non-polar molecular disks. Since $F_I^2 \gamma_s^d$ is always less than γ_l in Table 1, edge-on anchoring predominates.

A direct consequence of this inhibition is that internal π - π bonds in polyaromatic liquids will be stronger than π /non- π surface bonds in most cases, and polyaromatics will assemble in a way that preserves π - π bonding — a simple rule with the power explain a number of observations. First, edge-on anchoring is favored because it preserves internal π - π bonds at the expense of potential π -surface bonds — the exception being the graphite basal plane which offers π - π bonding across the interface. A second application of the π - π preservation principle Brooks-Taylor spheres. During heating the largest disk-like polyaromatics assemble in face-to-face to maximize π - π bonding. This π - π interaction is further enhanced by expelling small or defective weak- π -bond-formers to a surrounding isotropic phase. Within the droplets of the high-molecular weight ordered fluid, the particular bipolar configuration arises as a requirement of edge-on surface anchoring, selected by the same underlying rule: it preserves internal π - π bonds at the expense of the weaker potential π bonds with the surrounding disordered liquid. Indeed the observed bipolar structure achieves all possible internal π - π interactions except for two point defects at the polar caps (see Fig. 1), and is thus favored over the alternative, symmetry-allowed concentric, “onion” structure (see Fig. 1), which would sacrifice a full set of internal π - π bonds at the periphery.

Acknowledgments

Funding from the ACS Petroleum Research Fund, the NSF, the U.S. DOE, NETL, and the Fulbright Program (G. Krammer) are gratefully acknowledged. We also acknowledge sample donation by Mitsubishi Gas Chemical and technical discussions with Dr. Chris Hunter.

References

1. Oberlin, A., Chap. 1 in *Chemistry and Physics of Carbon*, Vol. 22, Marcel Dekker: New York, 1989.
2. Brooks, J.D.; Taylor, G.H., *Carbon* **1965**, 3, 185.
3. Hurt, R.H.; Chen, Z.-Y., *Physics Today*, **2000**, 53(3) 39.
4. Sonin, A.A., *The Surface Physics of Liquid Crystals*, Gordon and Breach Publishers: Luxembourg, 1995.
5. Mochida I.; Korai, Y.; Ku C.H.; Watanabe, F.; Sakai Y. *Carbon* **2000**, 38, 305.
6. Owens, D.K.; Wendt, R.C., *J. Applied Polymer Sci.*, **1969**, 13, 1741.
7. White, J.L.; Buecheler, M.; Ng, C.B., *Carbon* **1982**, 20, 536.
8. Fowkes, F.M., *Ind. Eng. Chem.*, **1964**, 56(12) 41.
9. Hunter, C.A.; Sanders, J.K.M., *J. Am. Chem. Soc.* **1990**, 112(14) 5525.
10. Marcek, A., *Carbon* **2000**, 368, 1863.
11. Cozzi F.; Cinquini M.; Annuziata, R.; Siegel, J., *J. Am. Chem. Soc.*, **1993**, 115, 5330.

Carbon Materials as Electrodes of Electrochemical Capacitors— Effects of Surface Oxides

Yau-Ren Nian and Hsisheng Teng

Department of Chemical Engineering, National Cheng Kung University, Tainan 70101, Taiwan

Introduction

Because of the high energy storage capability, electrochemical capacitors (ECs), which still retain the high power density feature of conventional capacitors, have received considerable attention for serving as peak-power or backup energy sources.¹ Porous carbon is the electrode material used most frequently for ECs. Use of high surface-area carbon electrodes results in large capacitance, mainly due to the formation of double layer at the electrode surface.² In addition to the charge accumulation mechanism that forms double layer on carbon surface, there are possible contributions from hetero-atom surface complexes that would provide sites for reversible chemisorption of a working ion and thus give rise to pseudocapacitance.³

The presence of oxygen surface complexes on carbon electrodes of an EC has been shown to affect the performance of the capacitor.^{4,5} Some types of oxygen functional groups may provide redox activity to enhance the pseudocapacitance.³ In this study surface oxides are introduced to porous carbons, and the electrochemical performances of the resulting capacitors are examined, in the attempt to identify the effects of different oxygen groups on double layer formation.

Experimental

Oxidation of activated carbon.—Polyacrylonitrile (PAN)-based activated carbon fabric was employed as the basic electrode material for the capacitors in the present work. The fabric has a thickness of 0.4–0.6 mm. The carbon fabric was cleaned by calcination at 900 °C in N₂ for 20 min prior to any measurement or further treatment. The thermally treated carbon fabric (CFT) was served as the fresh carbon in the present work.

Nitric acid was used in the oxidation treatment of CFT. The treatment was initiated by stirring one gram of the carbon in a 2 N nitric acid solution. The stirring was performed at 90 °C for 1 h. The oxidized product was then dried in vacuum at 110 °C for 7 h, to give the nitric acid-oxidized fabric. To prepare carbons containing different populations of surface complexes, the oxidized fabric was subjected to calcination at temperatures of 150, 300, 450, 600, and 750 °C under N₂ flow for 1 h.

Surface characterization.—Specific surface areas and pore volumes of the carbon fabric were determined by N₂ gas adsorption at –196 °C. Temperature programmed desorption (TPD) technique was employed to analyze the population of carbon-oxygen complexes on the fabric samples. The evolution of CO and CO₂ during TPD was continuously monitored using a non-dispersive infrared analyzer.

Electrochemical measurements.— Electrochemical measurements were carried out at ambient temperature using 1 M H₂SO₄ as electrolyte. The capacitance of the electrodes was measured by charging the cells at 0.5 mA to 0.6 V, followed by discharging to 0 V at different currents of 0.5, 1, 2, and 3 mA.

Results and Discussion

Surface characteristics of the carbon samples.—The physical characteristics of the carbon samples determined from N₂ adsorption are given in **Table I**. These carbon samples were designated using the nomenclature of the carbon fabric treated with nitric acid, CFN, followed by the calcination temperature. The data show that the pore volumes of these samples are predominantly contributed by micropores. The influence of physical characteristics will be considered to be minor in the present work,

since the changes in porosity and pore size distribution caused by the treatment are not obvious.

Table I.
Physical characteristics of the carbon fabric samples obtained from different treatment processes.

Carbon sample	Surf. area (m ² g ⁻¹)	Pore vol. (cm ³ g ⁻¹)	Pore size distribution	
			micro(%)	meso(%)
CFN150	925	0.44	100	0
CFN300	1030	0.49	100	0
CFN450	1080	0.52	100	0
CFN600	1140	0.55	100	0
CFN750	1060	0.51	98	2
CFT	1170	0.56	100	0

The population of oxygen functional groups present on the carbon surface was evaluated using TPD. It has been well known that upon thermal treatment in an inert environment oxygen functional groups such as carboxyl, anhydride and lactone groups would desorb as CO₂ while hydroxyl, carbonyl and quinone groups would desorb as CO.⁴

The accumulated amounts of CO₂ and CO evolutions during TPD are given in **Table II**. The results show that the amount of CO₂ evolved from these carbon samples decreases with the increasing calcination temperature, while that of CO evolved increases slightly with the temperature and passes through a maximum at 450 °C before showing a decreasing trend. The total O evolution calculated from the amounts of CO₂ and CO decreases monotonically with the calcination temperature. The decrease in the amounts of CO₂- and CO-desorbing complexes with the calcination temperature is expected, since the oxidized sites would undergo decomposition and become vacant upon calcination. The increase in CO-desorbing complexes in the low calcination temperature regime is not expected. This may probably result from the transformation of some CO₂-desorbing complexes into CO-desorbing during the period of calcination.

Table II.
Accumulated amounts of CO₂, CO and total O evolutions from the carbon fabrics during temperature programmed desorption

Carbon type	CO ₂ evolution (mmol g ⁻¹)	CO evolution (mmol g ⁻¹)	Total O evolution (mmol g ⁻¹)
CFN150	0.21	0.46	0.88
CFN300	0.14	0.52	0.80
CFN450	0.07	0.53	0.67
CFN600	0.03	0.35	0.41
CFN750	0.03	0.17	0.23
CFT	0.03	0.08	0.14

Electrochemical performance of the resulting capacitors.—To illustrate the influence of the surface oxides on the capacitance of carbon fabric samples, constant current charge-discharge cycling was conducted to measure the capacitance of the resulting capacitor cells. The specific discharge capacitance of the electrodes in the cells was calculated according to

$$C = (2 \times I \times t) / (W \times \Delta E)$$

where I is the discharge current, t the discharge time, W the carbon fabric mass on an electrode and ΔE the potential difference in discharge, excluding the portion of IR drop. The factor of 2 comes from the fact that the total capacitance measured from the test cells is the addition of two equivalent single-electrode capacitors in series.

Fig. 1 shows the specific capacitances of the samples calcined at different temperatures. As to the effect of oxidation, the results reflect that the specific capacitance of the carbon fabric

increases upon nitric acid treatment, except that CFN750 has capacitances slightly lower than those of CFT. The extent of calcination in N_2 following the oxidation shows a great influence on the performance of the resulting cells. The capacitance increases with the calcination temperature and reaches a maximum value at a temperature of 450 °C before decreases with the temperature. Obviously, not only the population but also the type of surface oxides affects the capacitance.

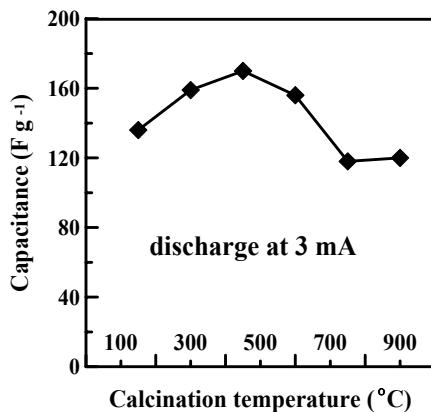


Figure 1. Variation of specific discharge capacitance for different calcination temperature.

Comparing the specific capacitance and the accumulated amount of CO-desorbing complexes of the samples, both quantities show similar variation trends with the calcination temperature and both have a maximum value at 450 °C. This indicates that the electrochemical capacitance of carbon can be improved through the introduction of CO-desorbing complexes, such as carbonyl and quinone.³ However, the variation of capacitance was not solely determined by the amount of CO-desorbing complexes. For example, CFN150 has a larger amount of CO-desorbing complexes than CFN600, but has a lower capacitance. Furthermore, the slight increase in the amount of CO-desorbing complexes with temperature for calcination temperatures lower than 450 °C cannot explain the sharp increase in capacitance with the temperature. On the other hand, the amount of CO₂-desorbing complexes shows a rapid decreasing trend within this temperature range. This indicates that CO₂-desorbing complex might play an inhibitor role in this energy storage process.

The effects of the CO- and CO₂-desorbing complexes on the charge-discharge mechanism can be further illustrated by plotting the capacitance against the difference of CO evolution minus CO₂ evolution. The results are shown in **Fig. 2**, showing that the capacitance is an increasing function of the difference between the amounts of the two types of complexes. This has demonstrated the positive and the negative roles that the CO- and the CO₂-desorbing complexes, respectively, act in improving the capacitance. On the basis of the preceding results, one can conclude that more than 40% of capacitance increase can be achieved through nitric acid oxidation in combination with 450 °C thermal treatment that would remove the majority of CO₂-desorbing complexes while leave the CO-desorbing unchanged.

The stability of the prepared capacitors can be examined by conducting repeated charge-discharge cycling. A capacitor equipped with CFN450 electrodes was charged and discharged between 0 and 0.6 V at 3 mA to confirm the stability. The variations of the discharge capacitance and coulombic efficiency⁶ with cycle number are shown in **Fig. 3**. The results exhibit that the capacitor has stable capacitance (about 166 F g⁻¹) and coulombic efficiency (about 99.5 %) over 100 cycles.

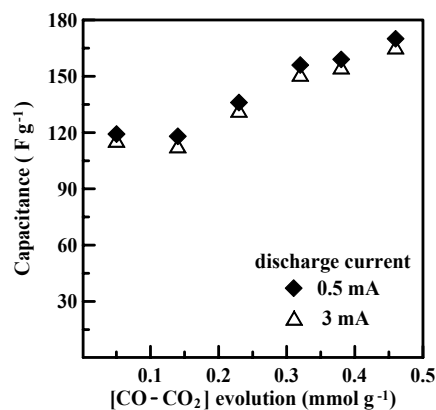


Figure 2. Variation of specific capacitance with the difference of CO evolution minus CO₂ evolution ([CO - CO₂]) in TPD.

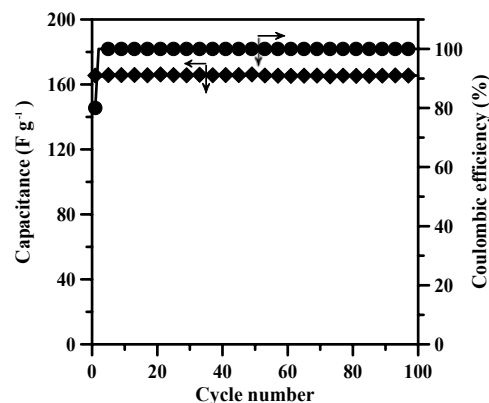


Figure 3. Variation of capacitance and coulombic efficiency with cycle number for the CFN450 electrode (2 cm²) charged and discharged at 3 mA in 1M H₂SO₄

Acknowledgments. Financial support from the National Science Council of Taiwan is gratefully acknowledged. The project number is NSC 90-2214-E-006-008.

References

- (1) R. Kötz and M. Carlen, *Electrochim. Acta*, **45**, 2483 (2000).
- (2) T.-C. Weng and H. Teng, *J. Electrochem. Soc.*, **148**, A368 (2001).
- (3) T. Nagaoka and T. Yoshino, *Anal. Chem.*, **58**, 1037 (1986).
- (4) K. Kinoshita, *Carbon: Electrochemical and Physicochemical Properties*, p. 302, John Wiley & Sons, New York (1988).
- (5) B. E. Conway, *Electrochemical Supercapacitors*, p. 259, Kluwer Academic / Plenum Publishers, New York (1999).
- (6) T. Osaka, X. Liu, M. Nojima, and T. Momma, *J. Electrochem. Soc.*, **146**, 1724 (1999).

CHARACTERIZATION OF A NEW REFRACTORY OXIDATIVE-RESISTANT CERAMIC CARBON INSULATION MATERIAL

Kristina A. Skokova* and Daniel B. Leiser

NASA Ames Research Center, Moffett Field, CA 94035

* ELORET Corporation, same address as above

Introduction

The current study addresses the problem of oxidation protection of low density porous carbon/carbon composites. These materials are attractive in several applications, including thermal protection systems for several NASA missions.

One method of oxidation protection of carbon could be the coating of the carbon surface with a protective substance such as organosilicon compounds and silicon oxycarbide [1-3]. Leiser et al. [4] proposed protection of a porous carbon substrate by its impregnation with silicon oxycarbide derived from siloxane gel, and the resulting material was called Refractory Oxidative-Resistant Ceramic Carbon Insulation (ROCCI). The subject of the current study is the extent of oxidation resistance in ROCCI before and after extended heat treatment.

Experimental

Carbon Substrates. Some typical properties of the porous carbon substrate used to produce ROCCI material are shown in Table 1.

Table 1. Some Properties of Carbon Substrates

Bulk Density	0.23 g/cm ³
Porosity	83 vol%
Average fiber diameter	8 μ m
Carbon content	99.9 wt%

ROCCI Material. The ROCCI material was provided by HC Chem Research and Service Corporation, courtesy of Dr. Ming-ta Hsu and Dr. Timothy Chen. It is prepared by the impregnation of the porous carbon substrate with a siloxane gel derived from organoalkoxy silanes in the base medium. The gel is dried and pyrolyzed at temperatures of 1000 - 1500 °C to obtain an insulation material containing approximately 32 wt% of carbon, 31 wt% of oxygen, and 37 wt% of silicon. A standard three-step process was employed. ROCCI material is black in color and has average density and average tensile strength of 0.95 g/cm³ and 0.53 MPa, respectively. In addition to the as-received ROCCI, a sample of ROCCI heat treated in argon at 1500 °C for 24 hours was studied. The latter sample lost about 58% of its weight and changed its color to gray after the heat treatment.

Procedures. Scanning Electron Microscopy (SEM) images were taken on an Amray 1810 instrument; samples were coated with gold/palladium before the SEM analysis. X-Ray Diffraction (XRD) spectra were obtained on a Scintag XGEN-4000 instrument using 0.05° step and 2°/min step rate. Oxidation properties were studied by thermal gravimetric analysis (TGA) and by isothermal heating the material at 1700°C in air for 30 min. TGA runs were done in 13% oxygen/argon mixture with a heating rate of 10 °C/min. using a Luxx STA 409PC apparatus from Netzsch.

Results and Discussion

SEM Characterization. A micrograph image of the three-step ROCCI is shown in Figure 1. Carbon fibers and the matrix material can be clearly seen; however, there is no immediate coating of carbon fibers with the silicon oxycarbide. Figure 2 and Figure 3 present images of ROCCI after the treatment in air at 1700 °C and in argon at 1500 °C, respectively. The air-oxidized sample shows no presence of carbon fibers which were gasified due to oxidation. The argon-treated sample does show the presence of the initial fibrous structure; however, the fibers are covered with a product of decomposition of silicon oxycarbide matrix which had a distinctive whisker-like structure. The nature of these whiskers is revealed by the XRD analysis.

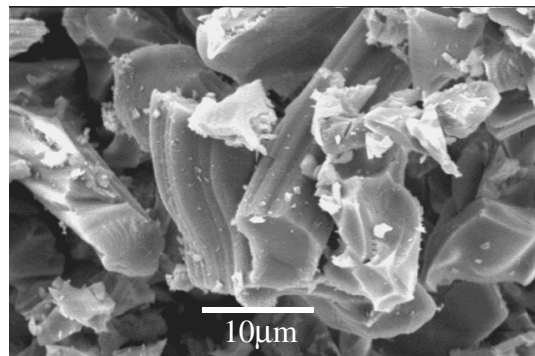


Figure 1. Micrograph of the three-step ROCCI material.

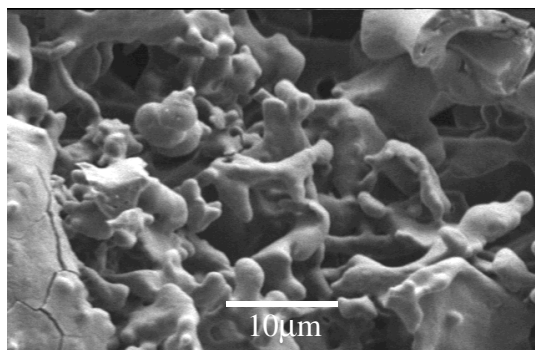


Figure 2. Micrograph of the three-step ROCCI heat treated in air at 1700 °C for 30 min.

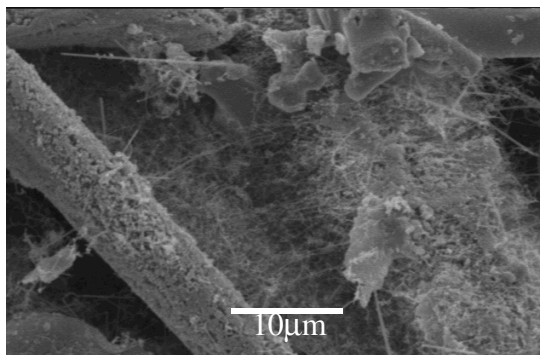


Figure 3. Micrograph of the three-step ROCCI after heat treatment in Argon at 1500 °C for 24 hours.

XRD Analysis. Three XRD patterns of the as-received ROCCI sample, after oxidation in air at 1700 °C, and after heat treatment in argon at 1500 °C are shown in Figure 4. Before the oxidation, there are no distinctive peaks which suggests amorphous glass-like structure of silicon oxycarbide matrix in ROCCI. After the heat treatment in air, there is a distinctive presence of SiO₂ (cristobalite) which is most likely formed due to high temperature oxidation of silicon oxycarbide. After heat treatment in argon, all the peaks in the XRD spectrum coincide with SiC peaks. It is therefore concluded that silicon oxycarbide changes its structure to silicon carbide upon the heat treatment in inert atmosphere. It is also evident that the whiskers seen on SEM image of the heat treated ROCCI sample (see Figure 3) is silicon carbide.

Oxidation Stability. Figure 5 shows the TGA weight loss curves of three samples (as described in the figure caption). The ROCCI sample appears to be slightly more stable to oxidation than the carbon substrate, however complete gasification of both samples due to the reaction with oxygen starts at approximately 600 °C and is finished by the time the temperature reaches 820 °C. Therefore, there is no great effect of silicon oxycarbide matrix as an oxidation protection system. The absence of

adequate protection is most likely due to the fact that the matrix does not cover the surface of the fiber as is evident from the SEM images. However, the heat treatment of ROCCI at 1500 °C in an inert atmosphere leads to the formation of SiC as follows from the XRD analysis described above, and thus reduces significantly the oxidation rate.

The fact that polysilanes and polycarbosilanes could be converted into silicon carbide upon heat treatment is known in the literature [5]. The mechanism of conversion of silicon oxycarbide to silicon carbide in the current study remains unclear. It is possible that silicon oxycarbide is subject to pyrolysis and the products of pyrolysis get deposited on the carbon fiber in a manner similar to a chemical vapor deposition process. The fact that the sample heat treated at 1500 °C in argon, does not lose any weight at 1000 °C in air suggests that the thickness of the SiC coating on the fibers is sufficiently high to protect them from oxidation. It is also possible that the outer layer of carbon fibers gets converted into SiC during the sample pyrolysis. Clarification of these questions is the subject of future research.

Conclusions

The oxidation stability of the new ROCCI material was studied. High temperature oxidation of ROCCI at 1700 °C leads to the formation of cristobalite and the loss of carbon fibers. It was shown that the oxidation resistance can be enhanced by high temperature treatment in an inert atmosphere due to the formation of SiC coating on the carbon fibers. The exact nature of the interaction of carbon fibers with the silicon oxycarbide matrix is the topic of future research.

References

- (1) Harris, M.; Chaudhary, T.; Drzal, L.; Laine, R.M. *Mater. Sci. Eng. A*, **1995**, 195, 223.
- (2) Manocha, L.M.; Manocha, S.M. *Carbon*, **1995**, 33, 435.
- (3) Keller, T.M. *Carbon*, **2002**, 40, 225.
- (4) Leiser, D.B.; Hsu, M.S.; Chen, T.S. U.S. Pat., No. 6,225,248, **2001**.
- (5) Brook, M.A In *Silicon in Organic, Organometallic, and Polymer Chemistry*; John Wiley & Sons: New York, 1995; p. 366.

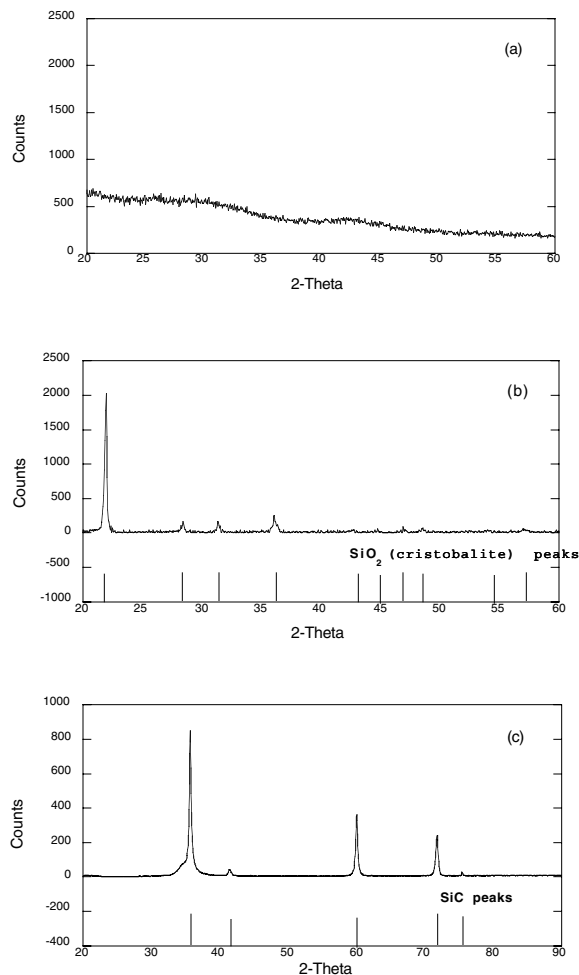


Figure 4. XRD patterns of (a) as-received ROCCI; (b) ROCCI oxidized at 1700 °C; (c) ROCCI heat treated in argon at 1500 °C.

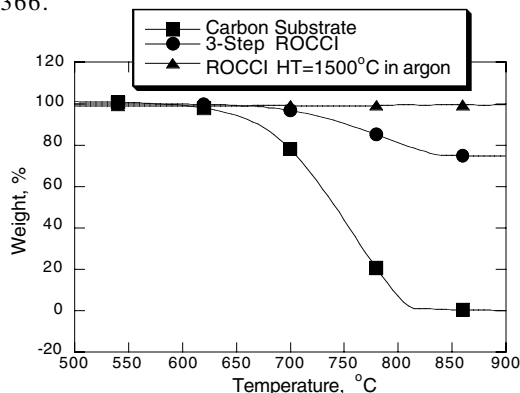


Figure 5. TGA weight loss curves due to oxidation in a 13 % oxygen/argon mixture for the samples of starting carbon substrate, three-step ROCCI, and ROCCI heat treated at 1500 °C in argon.

COMPARISON OF THE MERCURY-FLUE GAS-SORBENT INTERACTIONS ON CARBONS FROM NORTH DAKOTA AND TEXAS LIGNITES

*E.S. Olson, J.D. Laumb, S.A. Benson, G.E. Dunham, R.K. Sharma,
S.J. Miller, J.H. Pavlish*

Energy & Environmental Research Center
University of North Dakota
Box 9018
Grand Forks, ND 58202-9018

Introduction

Effective sorbents are needed for the control of mercury emissions in flue gas from coal-burning utilities. The commercial powdered carbon Norit flue gas desulfurization (FGD) sorbent has been thoroughly investigated at the Energy & Environmental Research Center (EERC) as a sorbent for elemental mercury (Hg^0) in flue gas streams (1, 2). Extensive factorial evaluations of powdered sorbents were conducted in a bench-scale system consisting of a thin fixed-bed reactor in gas streams containing $15 \mu\text{g}/\text{m}^3$ of Hg^0 in various simulated flue gas compositions consisting of acidic SO_2 , NO_2 , and HCl gases plus a base mixture of N_2 , O_2 , NO , CO_2 , and H_2O (1). In an atmosphere containing HCl or NO_2 , the Norit FGD, which is a Texas lignite-derived activated carbon (AC), was effective for capture of Hg^0 from the gas phase at temperatures of 100° to 150°C . Without either HCl or NO_2 in the gas stream, the carbon sorbents are ineffective, and immediate breakthrough occurred.

Mercury-Flue Gas Interactions with FGD Sorbent

In tests conducted with the FGD sorbent in the simulated flue gas containing NO_2 but not SO_2 , very little breakthrough was observed over an extended time period, indicating that the bound mercury form is quite stable. The capture is attributed to oxidation of the Hg^0 and concomitant reduction of NO_2 with formation of a low-volatile oxidized mercury species that remains bonded to the sorbent (3). Reactions of Hg^0 with NO and NO_2 in a glass container were previously reported to form mercuric oxide and mercuric nitrate/nitrite mixtures (4).

When SO_2 was added to the gas mixture containing the NO_2 , the mercury sorption rate was initially high (98% of inlet Hg^0 was sorbed); however, breakthrough occurred at times inversely proportional to the concentration of SO_2 ; that is, the higher the concentration of SO_2 is, the shorter the breakthrough time. This sensitivity is consistent with the hypothesis that SO_2 poisons the basic binding site for $\text{Hg}(\text{II})$ on the sorbent surface. With typical flue gas SO_2 concentrations (1500 ppm), the breakthrough occurs after 1 hour at the 107°C conditions. The breakthrough curve was relatively steep, increasing to 100% or greater emission after about 2 hours. Not only is mercury no longer sorbed, but mercury sorbed earlier in the experiment is released. The mercury that is emitted from the sorbent after breakthrough is entirely an oxidized mercury species. In reactions conducted with NO_2 and SO_2 and no HCl , this volatile oxidized mercury product was identified as mercuric nitrate (5, 6). We recently showed that sequential removal of the inorganic matter from the FGD sorbent did not significantly affect the breakthrough behavior (7); thus the basic groups, such as calcium oxide present in the FGD sorbent, played no role in the mercury-flue gas interactions that determine the breakthrough capacity.

Mercury-Flue Gas Interactions with EERC Activated Carbon Sorbent

ACs were prepared at the EERC from a high-sodium North Dakota (ND) lignite by mild steam activation. The BET surface area

was low ($245 \text{ m}^2/\text{g}$), owing to sodium-catalyzed burnout of micropores in the highly reactive char and creation of macropores. Mercury sorbent experiments were performed with a high-sodium ND lignite AC in simulated flue gas compositions to determine the mercury-flue gas interactions and sensitivities to SO_2 concentrations as were performed with the FGD carbon. Initially, a large amount of sorbent was used to provide samples for x-ray photoelectron spectroscopy (XPS) and x-ray absorption near edge structure (8). Later, a small sample of the EERC sorbent was compared with the FGD sample under similar conditions. These runs were performed with SO_2 and NO_2 plus the base composition and both with and without HCl . In the presence of HCl , the breakthrough times for the two sorbents were similar. However, in the absence of HCl in the gas stream, no breakthrough was observed for the EERC high-sodium carbon sample, in contrast to the typical 1-hour breakthrough characteristic of the very low-sodium FGD sorbent as well as several other carbons. Thus the sensitivity to SO_2 is different for the EERC carbon. This behavior is hypothesized to result from the effect of sodium oxide on the sorbent surface in helping to defeat the interference caused by the SO_2 .

XPS Analysis of Flue Gas-Exposed Sorbents

Further insights into the mechanisms of the mercury-flue gas-sorbent interactions were derived from the XPS data obtained from sorbents exposed to various flue gas compositions for time periods before and after breakthrough of mercury (8). Although it was not possible to determine mercury speciation of the bound mercury, information on the forms of sulfur and chlorine was especially important in constructing a model for the interactions. For this study, the two ACs, Norit FGD and the EERC AC, were placed in a fixed bed and subjected to simulated flue gas atmosphere environments containing $15 \mu\text{g}/\text{m}^3$ of Hg^0 with various levels of SO_2 , NO_2 , HCl , and H_2O . The XPS analysis determined the abundance and form of sulfur, chlorine, oxygen, nitrogen, silicon, iron, and carbon on the surfaces of the exposed sorbents. Detailed, high-resolution XPS scans were performed for S, Cl, N, and Fe.

The XPS analysis indicated that sulfur(VI) (sulfate or bisulfate) is the major sulfur species on all the sorbent samples exposed to flue gas compositions. The longer the exposure to SO_2 , the more sulfate is found in the sample. When NO_2 was omitted from the flue gas, less sulfate was accumulated. A decrease in sulfate was also observed when H_2O was omitted from the gas composition. The presence or absence of HCl had no effect on the sulfate formed. Based on these analyses, several adsorption as well as chemisorption events must occur during the exposure of carbon sorbents to flue gas components. The adsorbed SO_2 is clearly oxidized on the sorbent surface, resulting in bound bisulfate. The continued accumulation observed for sulfate or bisulfate should occur at basic sites, including basic sites on carbon that are responsible for binding the Lewis acid $\text{Hg}(\text{II})$. This is consistent with the large sensitivity of Hg breakthrough observed for SO_2 concentrations. The SO_2 oxidation reaction is influenced strongly by the availability of NO_2 , a good oxidizing agent. Although O_2 may also serve as the electron sink, or even the carbon structure itself, the reaction in the absence of NO_2 gives much less sulfate. These data also indicate that the SO_2 oxidation reaction involves water.

The XPS data showed that chlorine is present as both chloride ion and covalent (organic) chlorine. If mercuric chloride were present on the surface, the very small amount could not be seen owing to the interference of these forms. More chlorine was present on the exposed sorbent when no SO_2 was used in the gas composition. Importantly, the chlorine forms disappear from the carbon surface when breakthrough occurs. Thus the HCl in the flue gas can donate a hydrogen ion to a basic site (Bronsted acidity), as well as add both

hydrogen and chlorine to a basic site to form two covalent bonds (a type of Lewis acidity). This addition is well known in olefin chemistry where alkyl halides are formed. A basic aromatic system, especially one containing nitrogen or oxygen, could react similarly, reversibly forming an organochloro intermediate. The accumulation of chlorine in the absence of SO₂ as well as the disappearance of chlorine after continued exposure is explained by competition of HCl with bisulfate. As more bisulfate is generated from SO₂ at the carbon surface, it competes with the HCl, and the equilibrium shifts toward displacement of the chlorine, owing to the high volatility of the HCl.

Current Model for Sorbent Interactions

Because of the interference caused by silicon, XPS data could not be obtained for the mercury species present in the exposed sorbents. Nevertheless, the understanding gained about the flue gas interactions at the carbon basic sites contributes to the current model of mercury–flue gas–sorbent interactions involving the basic sites on the carbons. The interactions that appear to be adequate for explaining much of the behavior of the FGD sorbent are summarized in the scheme shown in Figure 1. Further details are needed for explaining the defeat of the SO₂ poisoning in the EERC sorbent, and these are currently under investigation.

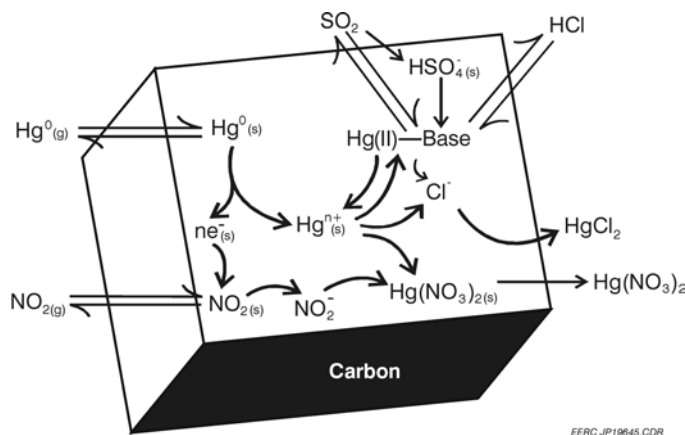


Figure 1. Mechanism for mercury capture on FGD sorbent.

Acknowledgments

Support is gratefully acknowledged from the EERC Center for Air Toxic Metals Industrial Affiliates Program and the Consortium for Premium Carbon Products from Coal (The Pennsylvania State University) under the U.S. Department of Energy Contract DE-FC26-98FT40350.

References

- (1) Miller, S.J.; Dunham, G.E.; Olson, E.S.; Brown, T.D. Flue Gas Effects on a Carbon-Based Mercury Sorbent. In *Air Quality: Mercury, Trace Elements, and Particulate Matter*, Special Issue of *Fuel Process. Technol.* **2000**, 65–66, 343–363.
- (2) Miller, S.J.; Dunham, G.E.; Olson, E.S.; Miller, S.J. Impact of Flue Gas Constituents on Carbon Sorbents. In *Proceedings of the Air Quality II: Mercury, Trace Elements, and Particulate Matter Conference*; McLean, VA, Sept 19–21, 2000; Paper A4-3.
- (3) Olson, E.S.; Miller, S.J.; Sharma, R.K.; Dunham, G.E.; Benson, S.A. *J. Hazard. Mater.* **2000**, 74, 61–79.
- (4) Freeman, E.S.; Gordon, S. *J. Amer. Chem. Soc.* **1956**, 78, 1813.
- (5) Olson, E.S.; Sharma, R.K.; Miller, S.J.; Dunham, G.E. Mercury in the Environment. In *Proceedings of a Specialty Conference*; VIP-91, Air & Waste Manag. Assoc., Minneapolis, MN, Sept 15, 1999; p 121.
- (6) Olson, E.S.; Thompson, J.S. Cryogenic and Solvent Trapping of Oxidized Mercury Species in Flue Gas. In *Proceedings of the EPA–DOE–EPRI Combined Power Plant Air Pollutant Control Symposium*:

"The Mega" Symposium; Chicago, IL, Aug 21–23, 2001; Session 16, No. 212.

- (7) Olson, E.S.; Dunham, G.E.; Sharma, R.K.; Miller, S.J. *Prepr. Pap.—Am. Chem. Soc., Div. Fuel Chem.* **2000**, 45 (4), 886.
- (8) Laumb, J.D.; Benson, S.A.; Olson, E.S.; Dunham, G.E. Characterization of Coal-Derived Mercury Sorbents. Presented at the 26th International Technical Conference on Coal Utilization and Fuels Systems, Clearwater, FL, March 5–8, 2001.

CVD SYNTHESIS OF SINGLE WALL CARBON NANOTUBES

Bhabendra K. Pradhan, Avetik R. Harutyunyan, U. J. Kim,
Gugang Chen, and P.C. Eklund

Dept. of Physics, 104 Davey Laboratory, The Pennsylvania
State University, University Park, Pennsylvania 16802, USA

Introduction

Single wall carbon nanotubes (SWNTs) were first discovered by scientists at NEC and IBM in 1993 [1,2]. Today SWNTs are synthesized by three main methods: arc discharge [1,2], pulsed laser vaporization [3], and chemical vapor deposition [4,6]. The growing interest of SWNTs for applications and fundamental science [6,7] demands new approaches and flexibility for the synthesis. Many researchers consider chemical vapor deposition (CVD) as the only viable approach to large-scale production. As a result, research is underway to optimize the CVD growth, i.e., to investigate the effect of catalyst composition, variation of supporting/substrate materials, synthesis temperature and hydrocarbon gases. Discovering CVD growth conditions that favor lower temperature and lower hydrocarbon flow is clearly important for the economical scale-up production.

In this research work, we have investigated the use of Fe and Fe/Mo metallic and oxide catalysts for the low temperature CVD production of SWNTs from methane under low flow. We find that Mo exhibits a significant synergistic behavior in this regime and that Fe/Mo functions well at low temperature (680°C), even as an oxide catalyst.

Experimental

(Fe) or (Fe/Mo) catalysts supported on $\sim 2 \mu\text{m}$ diameter Alumina (Al_2O_3) particles were prepared following reference [5]. Metal salts (99.999%, Alpha AESAR), i.e., $\text{Fe}(\text{NO}_3)_3 \cdot 9\text{H}_2\text{O}$, $\text{FeSO}_4 \cdot 5\text{H}_2\text{O}$, and $(\text{NH}_4)_6\text{Mo}_7\text{O}_{24} \cdot 4\text{H}_2\text{O}$, were dissolved in methanol, and mixed thoroughly (1h) with methanol suspensions of alumina (99.9%, Alpha AESAR). The solvent was then evaporated and the resultant cake heated to 90-100°C for 3 hours, removed from the furnace and ground in an agate mortar. The fine powders were then calcined for 1 hour at 400-500°C and then re-ground before loading into the CVD apparatus. The catalyst composition was confirmed using Energy Dispersive X-Ray (EDX) analysis in a scanning electron microscope. The CVD growth of SWNT used in this work was carried out in a quartz tube flow reactor (38mm inside diameter, and 90cm long) centered in a three-zone horizontal tube furnace. Carefully weighed catalyst samples (30-80mg) were placed in a quartz boat at the center of the reactor tube in the furnace. In some cases, a catalyst reduction step (or "activation") was performed *in situ* in the CVD reactor by first passing 100 cc/min flow of 10% H_2 /90% He (99.9%) at 500°C for 10-20 h. The reducing atmosphere was then replaced by argon (99.99%) and the temperature was raised at $\sim 10^\circ\text{C}/\text{min}$ to the desired growth temperature. SWNTs were then grown by passing a mixture of methane (40cc/min) diluted in argon (350 cc/min) over the catalyst at a temperature in the range 680-900°C for $\sim 1\text{h}$. The reactor was then allowed to cool to room temperature with argon gas flowing. The carbon product on the alumina support was then weighed to determine the carbon yield of the CVD process. We define carbon yield here as the fractional mass increase $(m_f - m_o)/m_o$, where m_f and m_o are, respectively, the final mass of the catalyst with carbon deposit and the initial mass of the catalyst. Of course, not all the car-

bon mass is in the form of SWNTs. Nevertheless, the amount of amorphous carbon detected in electron microscope images was small, and our practical definition of the relative yield is believed to provide a reasonable assessment of SWNT production in these experiments.

The structure of the SWNTs was studied with transmission electron microscopy (JEOL JEM 1200EX) at 120 KV. Raman Spectra were collected using a Bomem DA3+ FT Raman Spectrometer using Nd:YAG laser excitation ($\lambda=1064.5\text{nm}$) at 0.4mW power. A JY-ISA HR460 single grating spectrometer with CCD detector with a "supernotch" filter (Kaiser Optical) was used to collect Raman spectra with 488nm excitation from an Argon ion laser. All spectra were collected in air in the backscattering geometry at room temperature on the alumina-supported material taken from a cool CVD reactor.

Results and Discussion

In Fig.1 we display TEM images of SWNTs grown at 900°C in CH_4 for 90 min using Fe-oxide (Fig. 1a) and Fe/Mo-oxide (Fig. 1b) catalysts. The compositions were: $\text{Fe}:\text{Al}_2\text{O}_3 = 1:16$ and $\text{Fe}:\text{Mo}:\text{Al}_2\text{O}_3 = 1:0.2:16$, where the Al_2O_3 refers to the alumina support, and the ratio a:b:c refers to the wt% loading (e.g., $\text{Fe}:\text{Mo}:\text{Al}_2\text{O}_3 = 1:0.2:16$ indicates the wt. ratios $\text{Fe}/\text{Mo} = 5$, $\text{Al}_2\text{O}_3/\text{Fe} = 16$, etc.). Our preliminary CVD studies on the

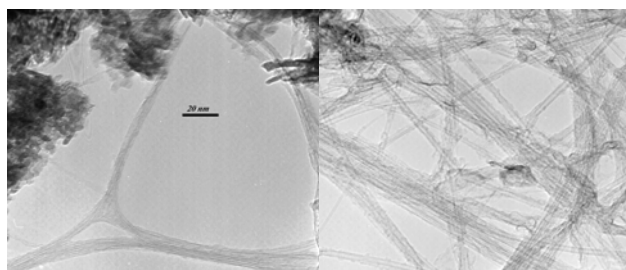


Fig.1 TEM images of bundles of SWNTs synthesized at 900°C (40 cc/min methane) using supported Fe (a) and Fe/Mo (b) catalysts in oxide form: ($\text{Fe}:\text{Al}_2\text{O}_3=1:16$) and ($\text{Fe}:\text{Mo}:\text{Al}_2\text{O}_3=1:0.2:16$).

Fe/Mo system indicated that 20 wt% Mo (relative to Fe) seemed to produce the maximum synergistic benefit. All the data on Fe/Mo catalysts presented here are for the "optimized" ($\text{Fe}:\text{Mo}:5:1$) weight ratio. The images in Fig. 1 are included to show the typical SWNT bundle structure observed. The dark, particle-like structure near the top of Fig. 1a comes from the alumina support. For both oxide catalysts at 900 °C, we observed an abundance of SWNTs. Analysis of many TEM images of SWNTs bundles produced with Fe-oxide exhibit an average bundle diameter of $\sim 10 \text{ nm}$. At high resolution, no amorphous carbon could be detected on the bundle exterior. It is interesting to note that TEM images taken on SWNTs produced at 900 °C with the Fe/Mo oxide catalyst (Fig1b) also showed many individual SWNT. They exhibited an average diameter of $\sim 1.5 \text{ nm}$ although large diameter individual tubes ($\sim 3 \text{ nm}$) were also observed. We did not observe the co-production of multi-walled carbon nanotubes in any of the samples at this temperature, or at lower temperatures.

In general, at the same CVD operating temperature, the bi-metallic Fe/Mo catalyst (oxide or reduced) was found to produce higher SWNT mass yields than the Fe catalyst. The synergism between Mo and Fe was very evident. At 800 °C and 680°C, Mo was required to activate the oxide catalyst for

SWNT growth (Fe-oxide alone could not produce tubes). Only at our highest temperature (900 °C) could Fe-oxide (without Mo) produce significant quantities of SWNTs. Furthermore, for the reduced Fe and Fe/Mo catalysts, the mass yields were always higher when Mo was present in the catalyst particle.

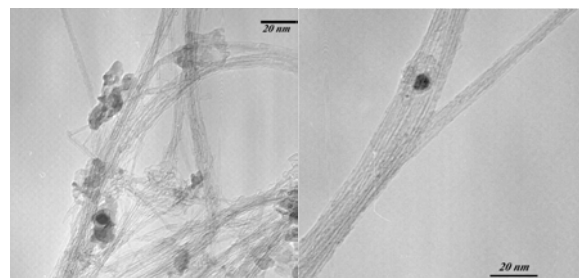


Fig.2 TEM images of bundles of SWNTs synthesized at 680°C (40 cc/min methane) using supported Fe (a) and Fe/Mo (b) catalysts in *reduced* (metallic) form: (Fe:Al₂O₃=1:16) (Fe:Mo:Al₂O₃ =1: 0.2:16). The catalysts were reduced *in situ* under flowing H₂ at 500°C.

A second series of experiments were conducted using the same Fe and Fe/Mo-oxide catalysts. This time, they were first reduced under flowing 10%H₂/90%He gas at 500 °C, reduction was found to activate the Fe catalyst at CVD growth temperatures as low as 680 °C. In Fig.2, we show TEM images of SWNTs grown at 680°C with the reduced Fe (Fig.2a) and reduced Fe/Mo (Fig.2b) catalysts. As in Fig. 1, we can only observe the “free” end of either an individual tube or a bundle of tubes. The other end is buried in the support and presumably is terminated on a catalyst particle. Importantly, we did not observe any metal particles at the “free” end of the tubes, and when individual tube ends were found, they appeared to be closed with a hemispherical fullerene cap. The addition of Mo in the reduced catalyst form seemed to produce better quality tubes, many in long straight bundles, as shown in Fig. 2b.

In Fig. 3 we display Raman spectra (1064 nm excitation) for the reaction products produced at various CVD growth temperatures with Fe-oxide and an optimized Fe/Mo-oxide catalyst (1:0.2:16). The region between 350 cm⁻¹ and 1300 cm⁻¹ is not shown, as no structure was evident in this region. The strongest peak of the high frequency tangential C-atom displacement band (or T-band) of SWNTs appears at ~1591cm⁻¹ [7]. It should be noted that changing the excitation frequency changes the sub-population of nanotubes observed in the spectrum. This follows from the observation that the Raman scattering from SWNTs is a resonant scattering process [7, 8]. For a particular excitation frequency, only a small subset of tubes in the sample whose diameter (or symmetry (n,m) [7]) provide for strong optical absorption at this excitation frequency can resonantly scatter [8]. Therefore, the changes in the Raman spectrum with excitation frequency, that are most easily detected, are observed in the low frequency region where the frequency of the radial mode bands are strongly related to tube diameter ($\omega_r \sim 1/d$). From the Raman spectra displayed in Fig. 3, we can conclude that the Fe-oxide (without Mo) produces tubes only at 900°C. Furthermore, with Mo added to the Fe-oxide catalysts, the spectra show clearly that SWNTs could be grown at temperatures as low as 680°C, a dramatic improvement in the catalyst performance with added Mo. Finally, it is worth men-

tioning that the Raman T-band spectrum shows that the optimized Fe/Mo-oxide catalyst is not active at 600 °C.

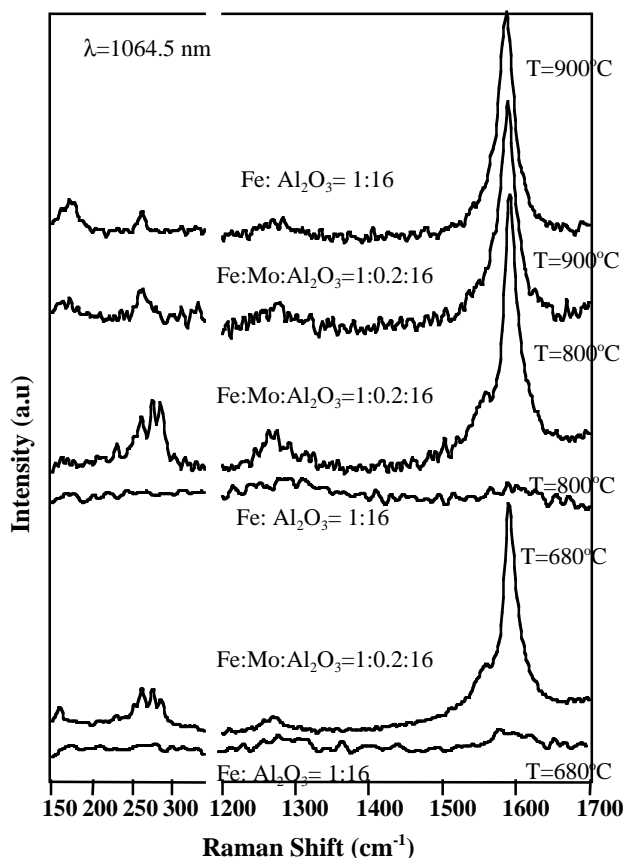


Fig.3 Raman spectra for carbon materials grown at various CVD temperatures with Fe and Fe/Mo catalysts in *oxide* form. The CVD growth temperatures and catalyst composition are indicated above each spectrum. The T~ 300 K spectra were collected using 1064 nm excitation with carbon still on the alumina support.

an additional constant term (12 cm⁻¹) is needed to include the effect of tube-tube interactions within a bundle. In this case, $\omega_r = 12 + 224(\text{cm}^{-1} \cdot \text{nm})/d$ [8]. Some small differences in the SWNT radial breathing mode region in Fig. 3 (Fe-oxide, Fe/Mo-oxide; 1064 nm excitation; variable growth temperature) can be observed. However, no real trends in these radial mode bands can be detected for the oxide catalysts as a function of CVD reaction temperature.

Using the SWNT T-band intensity and bandshape as our caliper, and consistent with the Raman spectra collected with 1064 nm excitation (Fig.3), we find that the tubes participating in the resonant scattering with 488 nm radiation confirm that the Fe/Mo-oxide catalyst is active down to 680°C. In Fig. 3, the notch in the T-band at ~1575 cm⁻¹ is seem to be deepest at the CVD growth temperature of 800°C. In some sense, the depth of this notch is a measure of sample quality, as it must deepen when the Raman linewidths decreases (tube wall disorder would increase these Raman linewidths; amorphous carbon coating on the tube walls might also serve as a line broadening mechanism). Using this qualitative “T-band notch” criterion,

the 800°C CVD reaction appears to have produced the “best” tubes.

The broad band at $\sim 1280\text{ cm}^{-1}$ with 1064 nm excitation seen in the spectra displayed in Fig's 3 and 4 are well known to stem from in various forms of disordered sp^2 carbon [7-9]. The band is “dispersive”, i.e., it's position (cm^{-1}) depends on excitation frequency. The cross section for scattering at this frequency requires disorder. It is usually referred to as the “disorder”-band or “D-band”. Here, the band can be associated with scattering from all disordered sp^2 carbon in the sample (including the SWNTs). Consistent with our discussion above regarding disorder and the depth of the T-band “notch”, when the T-band notch is deep, we can also observe that the D-band is weak, and vice versa. It should be pointed out that the intensity of the carbon D-band is normally suppressed using 1064 nm excitation; the spectra collected at 488 nm are, as a consequence, more sensitive to this D-band contribution.

Conclusions

SWNTs were synthesized by CVD in methane at very “soft” conditions, i.e., low temperature (680°C) and low methane flow rate (40 cc/min). Under these soft conditions, even the reduced Fe catalyst was active. Also under these conditions ($T = 680^\circ\text{C}$, 40 cc/min) the addition of 20 wt% Mo (i.e. Fe:Mo=5:1) was sufficient to make the catalyst active in oxide form, i.e., no activation in H_2 was found necessary, *even at 680 °C*. As the reduction (or activation) of the growth catalyst in H_2 represents an expensive, additional step in the CVD process, this is an important result from the present study. In general, we find a synergistic benefit from the addition of 20 wt% Mo to the Fe-catalyst. No evidence for the co-production of multi-walled tubes was found.

Acknowledgement

This work was supported, in part, by Honda Motors Fundamental Research Laboratories (A. R. H. and B. K. P) and by the NSF MRSEC (DMR-0080019) Program at PennState (G.C.).

References

1. S. Iijima, T. Ichihashi, *Nature* **1993**, 363, 603.
2. D. S. Bethune, C. H. Kiang, M. S. de Vries, G. Gorman, R. Savoy, J. Vasquez, R. Beyers *Nature* **1993**, 363, 605.
3. T. Guo, P. Nikolaev, A. Thess, D. T. Colbert, R. E. Smalley *Chem. Phys. Lett.* **1995**, 243, 49.
4. J. F. Hafner, M. J. Bronikowski, B. R. Azamiam, P. Nikolaev, A. G. Rinzler, D. T. Colbert, R. E. Smalley, *Chem. Phys. Lett.* **1998**, 296, 195,
5. K. Tanaka, T. Yamabe, K. Fukui, *The Science and Technology of Carbon Nanotubes*, Elsevier, (Oxford, 1999).
6. A.M. Cassell, J.A. Raymakers, J.Kong, H. Dai, *J. Phys. Chem.B* **1999**, 103, 6484.
7. M. S. Dresselhaus, G. Dresselhaus, P.C. Eklund, *Science of Fullerenes and Carbon Nanotubes*, Academic Press: New York, 1996.
8. M. S. Dresselhaus, P. C. Eklund, *Advances in Physics* **2000**, 49, 705.
9. A. R. Harutyunyan, B. K. Pradhan, U. J. Kim, G. Chan and P. C. Eklund, *Nanoletter*, 2002 (*in press*)

Effect of metal-loading upon nano-structure of carbon aerogel prepared from resorcinol and formaldehyde

Noriko Yoshizawa¹, Hiroaki Hatori¹, Yohko Hanzawa², Katsumi Kaneko², and Mildred S. Dresselhaus³

- 1) National Institute of Advanced Industrial Science and Technology, 16-1 Onogawa, Tsukuba 305-8569 JAPAN
- 2) Chiba University, 1-33 Yayoi, Inage, Chiba 263-8522 JAPAN
- 3) Massachusetts Institute of Technology, 77 Massachusetts Ave., Cambridge, MA 02139 USA

Introduction

Carbon aerogels, synthesized for the first time by Pekala¹, are novel mesoporous carbon materials with a low mass density, a large amount of mesopores, a high surface area, a high electrical conductivity, and other interesting properties.

Porous structure of carbon aerogel can be modified by several methods. Before preparation of aerogel, mixing ratio and concentration of starting materials, and a type and amount of catalyst are considered as important factors in sol-gel process. Furthermore, introduction of metal into their structure has other possibility to control pore structure as well as surface property of the aerogel samples. So far, loading of some types of transition metals, TiO₂, Ce and Zr etc. have been reported mainly for catalytic applications²⁻⁴. Meanwhile, Cu has been pointed out as one of the candidates for electrochemical applications. It was indicated⁵ that porous carbon material prepared by carbonization of commercial ion-exchanged resin with Cu²⁺ ion showed very high performance for an electronic double-layer capacitor. Carbon aerogel itself, actually, attracts much attention in this field because of its ideal pore structure.

We attempted to obtain Cu-loaded carbon aerogel by sol-gel method to achieve high dispersion of the metal. In this paper, structural dependences of samples upon preparation condition are summarized in detail.

Experimental

Preparation of Cu-loaded carbon aerogel. 1,3-dihydroxybenzene (resorcinol) and formaldehyde was dissolved in distilled ion-exchange water with a molar ratio of 1:2 ([resorcinol]=2.0mol/l) in the presence of Na₂CO₃ as a catalyst. Copper nitride was then added to the solution in order to obtain gel samples including 0.01, 0.05, 0.1 and 0.2 wt% of Cu. Hereinafter, each Cu-loaded sample is indicated as Cu-Cax-t (x: wt% of Cu, t: carbonized temperature if applied). After supercritical drying process, some of the gel samples were then carbonized at 600, 800 and 1000 °C. Attempts were also made to incorporate Cu more than 0.25 wt%, but it only provided precipitation of Cu compounds in the solution. A blank sample (CA0-t), i.e., aerogel sample prepared without Cu, was also prepared for comparison.

Characterization methods. N₂ adsorption isotherms of samples were measured at 77K by the gravimetric method to evaluate their pore structure. Observation with transmission electron microscope (TEM) was carried out at an accelerating voltage of 200kV. Carbon 002 lattice image, bright field image at low magnification, and electron diffraction pattern of every sample were taken. X-ray diffraction patterns were measured with CuK α radiation under 40kV-80mA condition. STAC-XRD (standardized analysis of coal by XRD)^{6,7} was applied to the peak in 2 θ =10-41° to study carbon 002 peak.

Results and Discussion

TEM observations for carbonized samples at 1000 °C demonstrated that, like the blank sample, Cu-loaded samples up to 0.1wt% have microcellular texture in which carbon nano-particles are interconnected each other. Typical TEM images of Cu-CA0.1 and Cu-CA-1000 are shown in Fig. 1. Carbon nano-particles constructing the network consist of less-crystalline,

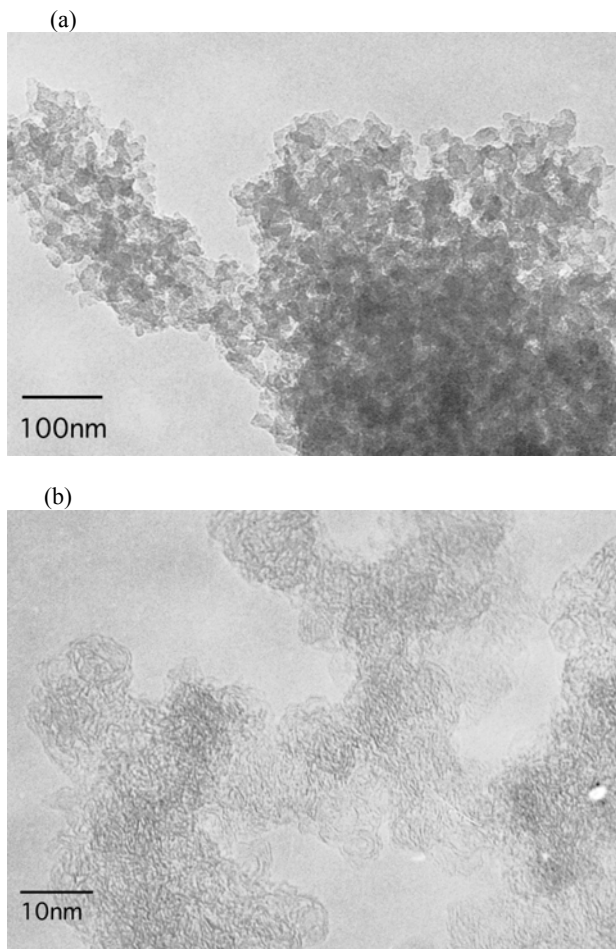


Figure 1. Typical TEM images for (a) CuCA0.1 (bright-field image) and (b) CuCA0.1-1000 (carbon 002 lattice image).

Table 1. Porosity parameters of Cu-loaded carbon aerogels and blank sample estimated by α_s -plot analysis.

Sample	$a_{\text{total}}/\text{m}^2\cdot\text{g}^{-1}$	$a_{\text{micro}}/\text{m}^2\cdot\text{g}^{-1}$	$V_{\text{micro}}/\text{cm}^3\cdot\text{g}^{-1}$	$a_{\text{ext}}/\text{m}^2\cdot\text{g}^{-1}$
CA0-1000	702	300	0.10	402
Cu-CA0.1-600	875	607	0.20	268
Cu-CA0.1-800	834	496	0.16	348
Cu-CA0.1-1000	866	633	0.20	253

a_{total} : total specific surface area

a_{micro} : specific surface area due to micropore

V_{micro} : specific micropore volume

a_{ext} : external specific surface area, including contribution of mesoporosity

Table 2. Structural parameters evaluated by STAC-XRD analysis for Cu-loaded carbon aerogels and blank sample.

Sample	d_{002}/nm	SI	N_{av}
CA0-1000	0.383	0.233	2.45
Cu-CA0.1-600	0.388	0.218	2.30
Cu-CA0.1-800	0.390	0.216	2.39
Cu-CA0.1-1000	0.404	0.203	2.47

isotropic microtexture, and their diameters clearly depend upon the amount of Cu; less than 10nm for 0.01%, 10-15nm for 0.05%, and 15-20nm for 0.1%. For Cu-CA0.2-1000, on the other hand, huge carbon spheres in 3-5 micrometer are observed. Similar relationship between diameter of carbon particle and amount of metal has reported for Zr/Ce-loaded carbon aerogels⁴. At present, we think this phenomenon is associated with pH conditions of solution during sol-gel process. Concerning Cu, presence of it in Cu-loaded samples was confirmed by ICP measurements. But neither Cu metal nor any other compounds was found by the TEM observation, which can be related to a fine dispersion of Cu in their structure. In addition, there was no trace of catalytic graphitization in carbon texture. It is consistent with a very few capability of Cu to promote the effect.

According to N₂ adsorption measurement, texture of Cu-loaded samples is microporous much more than the blank sample. It is further clarified by an analysis with the αs plot. Table 1 summarizes the porosity parameters for the carbonized samples including 0.1wt% Cu and the blank sample. Compared with CA0-1000, micropore volume in Cu-CA0.1-1000 is almost double. It is further noted that this highly developed microporosity at almost the same level was found for the samples heat-treated at 600 and 800 °C.

Difference of pore structure among these samples was also studied by XRD measurement of the samples. Evaluation of the stacking structure becomes possible by STAC-XRD analysis; this method has established by some of the authors as a standardized analysis for coals and related less-crystalline carbon materials. This method is established to characterize stacking structure of aromatic layers in carbonaceous substances or carbon materials with less crystallinity. The process is described in detail elsewhere^{6,7}. Briefly, it includes three steps:

- (1) As-measured XRD pattern is correlated with a polarization factor, an absorption factor, and an atomic scattering factor. Interlayer spacing, d_{002} is given according to the Bragg's law.
- (2) In the corrected profile, a baseline is drawn between two lowest points located at both sides of the 002 peak. Stacking index, SI , is a parameter corresponding to the crystallinity of the samples, and is estimated as the 002 peak area over the baseline to the total area of 002.
- (3) Fourier transformation is performed for the intensity over the baseline to obtain a Patterson function ($P(u)$). The distribution of the number of stacking aromatic layers per stack and the average number of layers, N_{av} , are evaluated from $P(u)$.

We have already reported the numerical relationship between microporosity and stacking structure of aromatic layers for some types of microporous carbon materials. Table 2 shows d_{002} , SI , and N_{av} for each sample. It is obvious that d_{002} for Cu-loaded samples is larger than the blank sample, while SI value is smaller. It means that development of stacking structure in the aerogel samples are restrained by introducing Cu.

Conclusions

Copper-loaded carbon aerogels were prepared by sol-gel synthetic method in Cu(NO₃)₂ solution. According to TEM observations, Cu-loaded samples up to 0.1wt% consists of carbon nano-particles with less-crystalline, isotropic microtexture. Their diameters become larger with higher concentration of Cu, probably associated with pH conditions of solution during sol-gel process.

The αs -plot analysis of N₂ adsorption isotherms indicated that microporous texture was much developed in Cu-loaded samples. The difference of pore structure was also studied by XRD measurement. Followed by STAC-XRD analysis. It is found that basal spacing for Cu-loaded samples is larger than the blank sample, while stacking index is smaller, indicating that development of stacking structure in the aerogel samples are restrained by introducing Cu into their structure.

References

- (1) Pekala, R.W., Alviso, C.T.; Kong, F.M.; Hulsey, S.S. *J.Non-Cryst.Solids* 1992, 145, 90.
- (2) Bekyarova, E.; Kaneko, K. *Langmuir* 1999, 15, 7119.
- (3) Maldonado-Hodar, F.J.; Moreno-Castilla, C.; Rivera-Utrilla, J. *Applied Catalysts* 2000, A203, 151.
- (4) Maldonado-Hodar, F.J.; Moreno-Castilla, C.; Rivera-Utrilla, J.; Hanzawa, Y.; Yamada, Y. *Langmuir* 2000, 16, 4367.
- (5) Sakata, Y.; Muto, A.; Uddin, Azhar, Md.; Yamada, N.; Marumo, C.; Ibaraki, S.; Kojima, K. *Electrochem. Solid-State Lett.* 2000, 3, 1.
- (6) Yoshizawa, N.; Maruyama, K.; Yamada, Y.; Zielinska-Blajet, M. *Fuel* 2000, 79, 1461.
- (7) Yoshizawa, N.; Maruyama, K.; Yamada, Y.; Ishikawa, E.; Kobayashi, M.; Toda, Y.; Shiraishi, M.; *Fuel* 2000, in press.

EFFECT OF MICROSTRUCTURE AND SURFACE CHEMISTRY OF POLYACRYLONITRILE-BASED CARBON ANODE ON THE ELECTROCHEMICAL PERFORMANCE THEREOF

H. J. Lee, Y. J. Kim, *S. W. Lee, *B. W. Cho and C. R. Park

Enviro-Polymers Design Laboratory, Hyperstructured Organic Materials Research Center, School of Materials Science and Engineering, Seoul National University, Seoul 151-744, Korea.

*Battery and Fuel Cell Research Center, Korea Institute of Science and Technology (KIST), Seoul 130-650, Korea.

Introduction

It has been known that the performance of a lithium ion battery is function of various factors, such as particle size, electric conductivity, microstructure, and surface chemistry of the anode materials[1-2]. Among these factors, microstructure and surface chemistry of carbon anode are particularly important since these are directly correlated in lithiation/de-lithiation process and the formation of solid-electrolyte interface (SEI). Many earlier studies have been devoted to elucidating the microstructural effects on the performance of a lithium ion battery[3]. As a result, it is widely accepted that high crystallinity of a graphitic carbon contributes to a good cyclability but comparatively low charge/discharge capacity, and disordered structure of a non-graphitic carbon enhances the capacity with some deterioration of cyclability. However, for the effect of SEI formation, little information is available since much less attention has been paid to this particular issue until now.

So, this study aimed at elucidating the effect of microstructure and surface modification of PAN-based carbon materials on the electrochemical performance thereof, with emphasis on the variation of SEI formation behavior with surface modification with sulfuric acid.

Experimental

Materials. PAN powder, having been commercially used for the manufacture of acrylic fibers, was supplied by Hanil synthetics, Ltd., Korea. PAN contains acrylonitrile of 91.5 wt% and methylacrylate of 8.5 wt%.

Preparation of carbonized PAN film. PAN powder washed with distilled water was dissolved in DMF with stirring at room temperature. After thorough dissolution, the solution was cast to a film on a petri dish and vacuum dried at 55°C for 72hrs. The film placed between alumina plates was then heated up to 250°C with rate of 5°C/min under air atmosphere (1L/min) and held for 5 hrs. The stabilized films were finally heated up to 900 and 1100°C (denoted TAN9 and TAN11), respectively, with rate of 5°C/min under N₂ atmosphere (1L/min) and held for 1 hr, followed by cooling down to room temperature.

Surface modification with sulfuric acid. To modify the surface of carbonized samples, TAN9 and TAN11 samples were treated with 95% sulfuric acid at 80°C for 4, 7, 10 and 20 hrs, respectively (denoted TAN9(or 11)S(time)). After acid treatment, all the samples obtained were washed thoroughly with methanol and then vacuum dried at 70°C over night.

Characterizations. Elemental analysis was carried out with a Carlo Erba 116 Elemental Analyzer(Carlo Erba Instruments, Italy). Wide angle X-ray diffractograms were recorded on an MXP 18X-MF22-SRA diffractometer (MAC/Science, Japan) using Ni-filtered Cu K_α radiation (λ=1.54Å). XPS (XPS, VSW, UK) with Mg K_α X-ray source (1253.6 eV photons, ≤10⁻⁸ bar) was used to obtain S (2p) core-level spectra of the samples. In order to determine the surface

areas, pore size, pore size distribution and total pore volumes, nitrogen adsorption-desorption isotherms were recorded at 77K on an automatic adsorption instrument (ASAP 2010, Micromeritics, USA) in relative pressure ranging from 10⁻⁶ to 1. Prior to the measurement, all the samples were degassed at 250°C under nitrogen flow for at least 3hrs. The amount of surface functional groups was determined using Boehm's method. To measure the electrochemical performance of the surface modified carbons, the carbons were mixed with 3 wt% of acetylene black and 6 wt% of poly(vinylidene fluoride) (PVDF) binder to prepare an anode, and Li metal foil was used as a counter electrode. The electrolyte used was 1M LiPF₆ dissolved in a mixture of ethylene carbonate / dimethyl carbonate / ethyl methyl carbonate (1:1:1 volume ratio). Polypropylene was used as a separator.

Results and Discussion

Surface Chemistry. Analyses for elements and surface functional groups indicated that the carbons prepared at the higher HTT has the less contents of non-carbon atoms such as oxygen and nitrogen. So, as compared with TAN11 sample, TAN9 has the higher non-carbon atoms and thus the higher acidic functional groups after sulfuric acid treatment (see Figure 1). Indeed, FTIR and XPS analyses for TAN9 series indicate that Ph-SO₄H (sulfate) group was introduced by sulfuric acid treatment, evidenced by two peaks at 1170 and 1060 cm⁻¹ from SO₂ stretching in FTIR spectra, and the peak at 168.40 eV arising from S2p absorption in XPS spectrum.

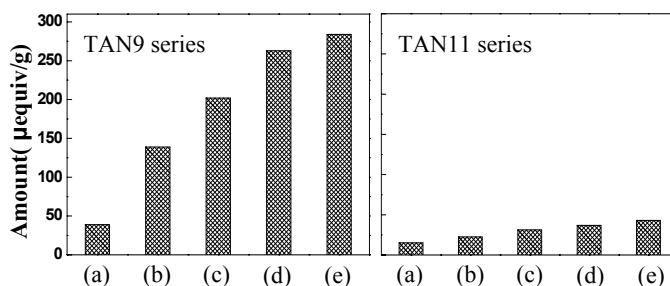


Figure 1. The amounts of acidic surface functional groups of TAN 9 and TAN11 after sulfuric acid treatment for (a) 0 hr, (b) 4 hr, (c) 7 hr, (d) 10 hr, and (e) 20 hr.

Microstructure. As for the microstructural changes with sulfuric acid treatment, XRD indicates that sulfuric acid attacks the carbon layers edgewise, so that the functional groups are introduced at the edge carbon atoms. Between TAN9 and TAN11 series, the more surface functional groups were found on TAN9, indicating that the carbon atoms in TAN11 are comparatively intact to an acid attack, which may suggest that less amount of oxygen containing carbons were in TAN11 samples. Table 1 clearly shows that micro-structural changes are reflected only on the value of L_a , suggesting the acid attack occurred edgewise.

Table 1. Structure parameters of TAN9 and TAN11 series

	d (□)	L_c (□)	L_a (□)		d (□)	L_c (□)	L_a (□)
TAN9	3.56	27	73	TAN11	3.53	33	80
TAN9S4	3.61	27	70	TAN11S4	3.54	33	74
TAN9S7	3.60	28	68	TAN11S7	3.54	32	76
TAN9S10	3.62	27	64	TAN11S10	3.55	33	73
TAN9S20	3.62	27	60	TAN11S20	3.55	34	73

The BET surface areas of the carbon materials were found decreased after sulfuric acid treatment from 7.3 to 5 m²/g and from

16.1 to 13 m²/g for TAN9 and TAN11 series, respectively. Moreover, by acid treatment, the pore size tended to become smaller with concurrent collapse of pre-existing micro-pores, as shown in Figure 2.

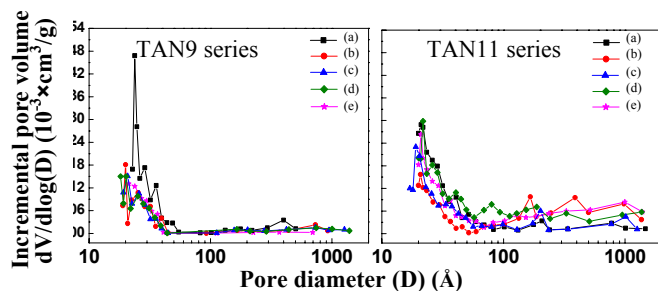


Figure 2. Pore size distribution in TAN 9 and TAN11 after sulfuric acid treatment for (a) 0 hr, (b) 4 hr, (c) 7 hr, (d) 10 hr, and (e) 20 hr.

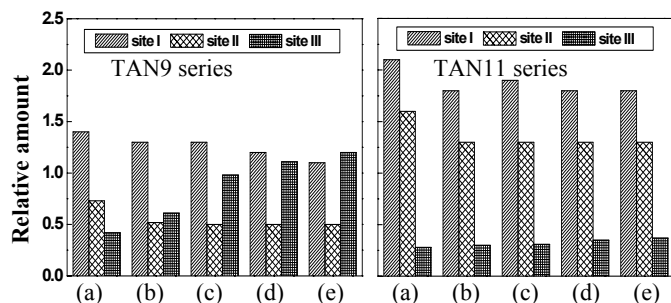


Figure 3. Relative amount of lithiation sites of TAN9 and TAN11 series after sulfuric acid treatment for (a) 0 hr, (b) 4 hr, (c) 7 hr, (d) 10 hr, and (e) 20 hr; Site I : $L_a^2 \cdot L_c$; Site II : BET surface area; Site III: [O]/[C] ratio.

Electrochemical Performance. In Li ion battery, there may be three sites which can be lithiated by Li ion: that is, between carbon layers (Site I), voids or the nano-space in-between carbon crystallites (Site II), and surface functional groups at the carbon surfaces (Site III). Site I, indicative of good cyclability, has been conventionally recognized as a space where intercalation/deintercalation of Li ions is occurring, and can be characterized by the interlayer volume expressed as $L_a^2 \cdot L_c$. Sites II and III that contribute to high discharge capacity and large irreversibility may be characterized with pore surface area and the amount of acidic functional groups, respectively.

Figure 3 shows the relative amount of each site in both TAN9S and TAN11S series. Figure 4 clearly indicates that TAN11 exhibits relatively low discharge capacity but good cyclability due to the dominance of Site I, whereas TAN9 shows high discharge capacity but rather lower cyclability due to rather higher amount of Sites II and III. Figure 5 shows that the surface treatment tends to increase the discharge capacity, although the increment is much less in TAN11S series. In TAN9S series, the discharge capacity decreases with the number of cycles but that after 15 cycles is still higher than the one of TAN9.

This indicates that the additional lithiation sites created by the introduction of acidic functional groups (Site III) contribute to increasing discharge capacity. In addition, Figure 6 exhibits that the initial irreversible capacity is linearly decreasing with increasing amount of Site III, which may be due to the formation of thin SEI around the functional groups distributed somewhat homogeneously along the edges of carbon layers.

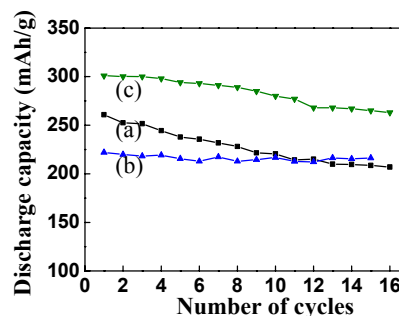


Figure 4. Electrochemical performances of (a) TAN9, (b) TAN11, and (c) MCMB in 1M LiPF₆ in EC:DMC:EMC (1:1:1).

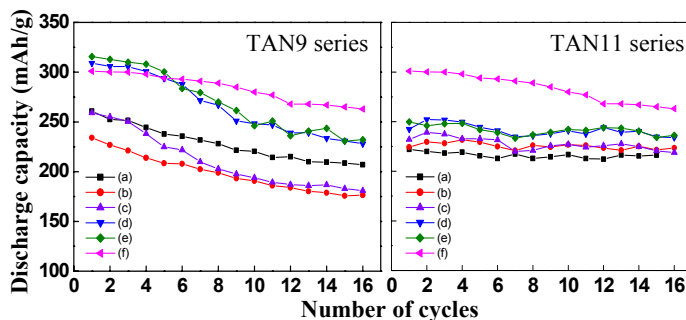


Figure 5. Electrochemical performances of (a) TAN9, (b) TAN9S4, (c) TAN9S7, (d) TAN9S10, (e) TAN9S20, (f) MCMB in 1M LiPF₆ in EC:DMC:EMC (1:1:1).

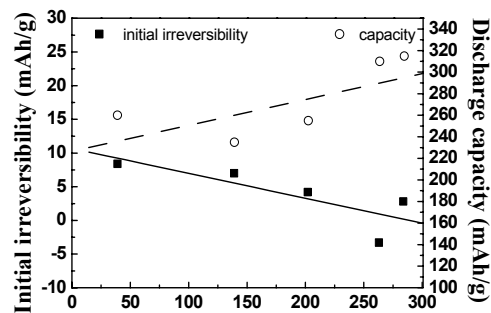


Figure 6. Changes in initial irreversibility and discharge capacity with the amount of acidic functional groups in TAN9S series.

From above-mentioned results, it is clear that the surface modification of carbons for anodic applications in Li-ion batteries can contribute to some extent to improving discharge capacity and reducing initial irreversibility.

Acknowledgement. This work was financially supported by the Hyperstructured Organic Materials Research Center (HOMRC) at Seoul National University (SNU).

References

- (1) Wakihara, M. *Mater. Sci. Eng.* **2001**, *R(33)*, 109-134.
- (2) Endo, M.; Kim, C.; Nishimura, K.; Fujino, T.; Miyashita, K. *Carbon* **2000**, *38*, 183-197.
- (3) Higuchi, H.; Uenata, K.; Kawakami, A. *J. Power Sources* **1997**, *68*, 212-215.

EFFECTS OF LIGNITE CATION CONTENT ON THE PERFORMANCE OF ACTIVATED CARBON PRODUCTS

E.S. Olson, R.S. Sharma, K.E. Eylands, D.J. Stepan

Energy & Environmental Research Center
University of North Dakota
Box 9018
Grand Forks, ND 58202-9018

Introduction

New federal drinking water regulations have been promulgated to restrict the levels of disinfection by-products (DBPs) in finished public water supplies. DBPs are suspected carcinogens and are formed when organic material is partially oxidized by disinfectants commonly used in water treatment. Many small water systems are currently using powdered activated carbon (PAC) for taste and odor control and have the potential to remove naturally occurring organic matter (NOM) from raw waters prior to disinfection, thus controlling the formation of regulated DBPs. Earlier studies at the Energy & Environmental Research Center (EERC) showed that a PAC prepared from North Dakota lignite was highly effective for removal of humate. We hypothesize that the sodium and calcium content of the coal plays a significant role in the development of pore structures and pore-size distribution, ultimately producing activated carbon products that have greater sorption capacity for specific contaminants, depending on molecular size. This paper reports the effects of organically and mineralogically associated sodium and calcium content on pore structure and sorption capacity of activated carbon products from North Dakota lignites.

Experimental

A moderately high-sodium lignite (7.2% sodium oxide in ash) was obtained from the Dakota Gasification Company. The coal was ground and sieved and 8×20 -mesh particles collected. A sample was ion-exchanged with ammonium acetate and mildly heated to produce a low-sodium, low-calcium coal. A portion of that sample was ion-exchanged with calcium acetate to produce the high-calcium sample. The three samples were dried and submitted for surface area and computer-controlled scanning electron microscopy (CCSEM), which is an automated technique that finds, sizes, and determines individual particle chemistry (mineral content and associations) for thousands of particles per sample.

Each sample was carbonized at 400EC in a nitrogen atmosphere for 30 minutes, followed by activation with steam at 750EC for 30 minutes. These conditions produce high-sodium activated carbons with high sorption capacity, but may not be optimal for the preparation of high-calcium or even low-sodium, low-calcium carbons. The low-sodium, low-calcium sample produced the highest yields and the high-sodium samples the lowest. Multiple-point surface area determination and porosity analyses were performed by PACS, Coraopolis, Pennsylvania.

Results and Discussion

Coal Sample Characterization. The mineral weight percent of the original high-sodium feed coal was calculated by the CCSEM process to be approximately 5.2 wt% on a coal basis. The dominant mineral phases were pyrite (FeS), calcite (CaCO_3), quartz (SiO_2), and several clay minerals (primarily aluminosilicates). Sodium and calcium were detected in many of the mineral phases at each of the three size classifications. In the larger particles (22 to 100 μm), Na was most commonly associated with aluminosilicate clay and CaCO_3 .

In the exchanged (low-Na, low-Ca coal, 2.9 wt% ash), Na is still present in many of the phases, but at a considerably lower amount. Some pits observed in the SEM that do not show up on either the feed coal or the high-Ca coal are interpreted as areas where Na-containing mineral phases were removed from the coal. Ca is decreased and mostly in a calcite phase. For the Ca-exchanged coal, increased amounts of Ca are in the clay, but most Ca is concentrated in a CaCO_3 or calcium oxide (hydroxide) phase. Most importantly, no calcium is distributed over the organic carbon phase of the coal. This distribution was unexpected, since it has generally been assumed that the calcium acetate exchange method is effective for adding calcium to coal organic phases.

Activated Carbon Characterization. The BET-specific surface areas of the carbons were low (Table 1), as were the total pore volumes. Because of the long equilibration times observed, the pore dimensions may be as small as 0.35 nm. A sample of the high-sodium, low-calcium carbon was not washed with water after preparation as were the other three samples analyzed. The identical results for this carbon indicate that sodium minerals do not block the micropores. Whether they block macropores is unknown, but they are easily removed in contact with water and will not cause a problem in surface water treatment which is normally conducted at basic pH anyway.

Table 1. Activated Carbon Surface Area and Porosity Data

Carbon-Metal Content	BET Surface Area, m^2/g	Pore Volume, cm^3/g	Avg. Pore Width, nm
High Sodium (feed)	245	0.14	1.2
High Calcium, Low Sodium	370	0.20	1.1
Low Sodium, Low Calcium	349	0.17	1.0
High Sodium, Low Calcium, unwashed	250	0.15	1.2

A greater carbon burnout is expected for the more reactive sodium-containing coal during carbonization. The lower-BET surface area and pore volume for the high-sodium, low-calcium carbon is consistent with a smaller total number of micropores, which can be attributed to a greater loss of carbon in the burnout. The concomitant increase in macropores resulting from this burnout does not show up in the distribution data, since there is a relatively low area associated with these pores. The remaining micropores in the high-sodium, low-calcium carbon are then roughly similar in size to those resulting from carbonization of the other coals. But the average pore width as calculated using a slit model ($w = 2V/S$) is slightly larger for the high-sodium, low-calcium carbon.

SEM photographs of the activated carbons prepared from the raw and exchanged coals were also analyzed, along with the corresponding microprobe data. The carbon resulting from activation of the raw high-sodium coal exhibited some areas with cracks that reveal a complex interior composed of micron-size features. Probe analysis of the grey carbon areas showed that a significant amount of sodium was associated with these carbon phases as well as the mineral phases (as sodium calcium silicates, sodium calcium aluminosilicates, and sodium calcium sulfates). Thus the sodium was not lost from the organic structure during the charring and carbonization process and was available for catalysis of reactions of the steam with the carbon during activation.

SEM photographs of the activated carbon from the calcium-exchanged coal showed a series of parallel micron-sized slits resulting from cleavage of the carbon particles. Inside the slits were

rough-looking submicron features. Probe analysis of the particles showed that the grey carbon phases contained no calcium. Only the white mineral phases contained calcium, as silicates, aluminosilicates, sulfates, and oxide. This finding is consistent with the composition of the original calcium-exchanged coal, which contained calcium only in the mineral phases. Thus since the calcium does not appear to be located close to the carbon structure, it would not be available for catalysis during activation. SEM photographs of the low-Ca, low-Na carbon prepared from the exchanged coal sample indicated that there was little difference in the particles from this and the calcium-exchanged carbon.

Adsorption Isotherms. To determine the adsorption capacities of the prepared carbons for PAC treatment of a surface water supply containing large amounts of peat-derived humate, such as the Red Lake River, the set of carbons was tested for adsorption of a standard humate solution prepared from a commercial (Aldrich) coal-derived (leonardite) humate. Initially for analysis of the adsorption data, $\log x/m$ was plotted versus $\log c$ to determine the fit to the Freundlich equation. The carbons exhibited similar nonlinear Freundlich isotherms. The log-log plots from this set of carbons are characterized by a very steep slope at low carbon amounts (high x/m), and a lower slope at moderate-to-high carbon amounts. Earlier adsorption studies with similar lignite-derived carbons and humate solutions also gave nonlinear plots, and in fact, the slopes and intercepts depended significantly on the starting concentration of humate in the experiments. This is indicative of complex selectivity factors involving adsorption of different portions of the polydisperse humate electrolyte. It appears that a large amount of some component is adsorbed, and then the majority of the humate is adsorbed less effectively. Humate molecules differ greatly in size, shape, and polarity, and each of these factors depends on the pH and ionic strength in the solution. Only a small portion of the humate molecules are expected to bind in micropores; the rest are too large.

To adjust for this complex behavior, the equilibrium concentrations in each experiment were normalized by dividing the unadsorbed humate amount (in mg) by the amount of sorbent (in g) added (1). The logs of these normalized concentrations (c/m) were then plotted versus the logs of the x/m values for each experiment. The improved linearity of the plot shows that the data fit this normalized model approach much better than the conventional Freundlich model. The resulting slope ($n = 0.27$) for the high-sodium carbon is, in fact, not too much different from that obtained in the literature for Calgon F400 activated carbon adsorbent with a humate substrate (1). A different humate was used, so the results cannot be compared exactly. The intercept for the high-sodium carbon isotherm is much larger ($K = 1.2$) than that obtained using the F400 carbon ($K = 0.8$). This is significant because it indicates that the carbon will be more effective in reducing the concentration of the humate at a given carbon dosage.

The normalized isotherm for the high-calcium carbon was plotted using the $\log c/m$ values. Although a higher slope ($n = 0.36$) was obtained for the plot of the high-calcium carbon, the intercept was quite low (0.65). Thus the high-calcium carbon is relatively poor at sorbing humate over most of the carbon dosages. The low-sodium, low-calcium carbon gave a similar slope ($n = 0.29$), and the intercept is low ($K = 0.85$), indicating the poorer sorption of humate by this carbon compared with the high-sodium carbon.

To predict the behavior of these prepared activated carbons for PAC applications in treating wastewater or hydrocarbon-contaminated water, the isotherms were determined for the adsorption of toluene by the set of carbons. These isotherms were also characterized as having a steeper slope at very low carbon loadings. The normalized isotherm slopes were reversed in order

from that observed for the macromolecular humates, consistent with the low surface area of the high sodium carbon.

CONCLUSIONS

The lowest-BET area was obtained for the high-sodium carbon, which can be attributed to enlargement of micropores as a result of sodium-catalyzed gasification reaction of the carbon structure. This hypothesis is consistent with the SEM microprobe analyses, which show that in both the coal and the activated carbon from this coal, the sodium is distributed over both the carbon structure and the mineral particles. Thus it is initially associated with carboxylate groups on the coal and then as sodium oxide or another active form in close proximity to the carbon and readily available for catalysis of gasification. In the exchanged coals, the sodium and other cations are mostly removed from the carbon structure of the coal, but addition of calcium did not effectively introduce calcium into the carbon structure. This was indicated by the SEM microprobe studies. Thus there was little catalysis of gasification during steam activation, and the mild activation conditions that were used did not effectively generate a large micropore volume.

The adsorption activities were determined for the three activated carbons using tests that would represent their use as potential PAC treatment agents for high-NOM surface water, such as that in northern Minnesota which drains from peat deposits. The intercept of the modified Freundlich plot representing the K value for the high-sodium carbon was much larger than that of the commercial Calgon F400 carbon as well as that of the high-calcium and the low-sodium, low-calcium carbon prepared in this work. Thus the high-sodium carbon will be considerably more effective in reducing the humate concentration for a given carbon dosage. The slopes of the normalized Freundlich plots for the various carbons including the Calgon F400 were similar. These results are consistent with the hypothesis that only the larger pores are effective for binding the large humate molecules and that the larger pores developed during activation of the high-sodium char give the appropriate macropore structure for humate binding.

Toluene isotherms were also performed for the set of carbons. These indicated that the high-calcium carbon and the low-calcium, low-sodium carbon were superior to the high-sodium carbon, but not as effective as a Calgon F400. This is consistent with the low-BET surface areas observed for the lignite-derived carbons, and thus there are a lower number of sites for binding the smaller toluene molecule in these carbons.

Acknowledgment. This research was done with the support of the U.S. Department of Energy (DOE) National Energy Technology Laboratory Cooperative Agreement No. DE-FC26-98FT40320. However, any opinions, findings, conclusions, or recommendations expressed herein are those of the authors(s) and do not necessarily reflect the views of DOE.

REFERENCES

- (1) Kilduff, J.E.; Karanfil, T.; Chin, Y.-P.; Weber, W.J. *Environ. Sci. Technol.* **1996**, *30*, 1336.

ENERGY AND ENVIRONMENTAL APPLICATIONS OF CARBON NANOTUBES

Sandeep Agnihotri¹, Massoud Rostam-Abadi^{1,2},
Mark J. Rood¹, and Ramsay Chang³

¹Department of Civil and Environmental Engineering
University of Illinois at Urbana-Champaign
Urbana, Illinois 61801

²Illinois State Geological Survey
Energy and Environmental Engineering Section
Champaign, IL 61822

³EPRI
3412 Hillview Avenue
Palo Alto, CA 94303

Introduction

In 1991, Iijima in Japan discovered carbon nanotubes, which are now known to exist in closed-ended multiple-walled and single-walled arrangements¹. The multi-walled nanotube² (MWNT) is an arrangement of concentric cylinders of carbon atoms with an outer diameter ranging from 5-30 nm, length ranging from 10's of nm to 10's of μm , and intertube distance of approximately 0.34 nm. MWNTs can be envisioned as layers of graphene sheets rolled together to form concentric cylinders (**Figure 1**). Single-walled nanotubes (SWNTs), on the other hand, are cylindrical carbon structures in which each carbon cylinder stands alone (**Figure 2**). Typically, the diameter of SWNTs ranges from 1.2-1.4 nm and the length ranges from 10's of nm to 10's of μm ³. The tips of nanotubes, both SWNTs and MWNTs, are commonly found closed.

Synthesis

Three major processes are currently used to synthesize carbon nanotubes: electric arc-discharge, laser ablation, and chemical vapor deposition (CVD). In the electric arc-discharge method, large currents are passed through two opposing graphite electrodes in an inert atmosphere such as helium. During the arc-discharge, carbon atoms evaporate from the anode (3000 °C) and grow (**Figure 3**) on the cathode in the form of nanotubes². The yield of carbon deposit, which generally contains MWNTs, depends on the experimental conditions such as the arcing current, and pressure and type of gas in which the electric arc is generated. Typically, this process can yield gram-sized quantities of MWNTs with lengths on the order of ten microns and diameters in the range of 10's of nm. For growing SWNTs, graphite electrodes usually are impregnated with metal catalysts such as Co, Cu, and Fe⁴.

The laser ablation process, which is similar to the electric arc-discharge method, uses an intense laser pulse to ablate a carbon target containing 0.5 atomic percent of Ni and Co. The target is heated in a furnace at 1200 °C. An inert gas flow is maintained to carry the grown nanotubes to the colder part of the reactor chamber where they are collected. This process mainly produces ropes of SWNTs in which tens of nanotubes are closely packed in a triangular lattice. The yield of nanotubes obtained by this process can be optimized to gram-sized levels³.

The chemical vapor deposition (CVD) method involves thermal decomposition of hydrocarbons (usually CH_4) at temperatures ranging from 500 to 1000 °C in the presence of a catalyst containing transition metals such as Fe and Mo. This process, which is more energy efficient than the electric arc-discharge and laser ablation methods, is ideal for synthesizing well-defined structures of nanotubes⁵. The yield and structure of nanotubes are affected by the type, purity, and porosity of the catalyst. It has been shown that the

methane CVD process can be used to obtain approximately 200% yields (2 grams of SWNTs per gram of catalyst) of high quality nanotubes⁶. The methane CVD process shows promises for large-scale production of defect-free carbon nanotubes.

The carbon nanotubes produced by these processes typically are closed-ended and associated with other carbonaceous species such as nanoparticles, fullerenes, and catalyst particles. Carbon nanotubes can be treated by acid leaching techniques (purification), which dissolve the graphitic and catalyst particles, to yield high purity materials⁷. In addition, heat treatment in air (<400 °C) followed by acid treatment opens the ends of carbon nanotubes⁸.

Carbon nanotubes possess some peculiar properties. They can be metallic or semiconducting, depending on the diameter and helicity of the nanotube and presence of structural defects on the carbon nanotube surface⁹. Metallic SWNTs that are several microns long exhibit two-terminal resistances on the order of 10 to 100 kilo-ohms. Semiconducting SWNTs of similar configuration have electrical resistance ranging from 100 kilo-ohms to several mega-ohms. Carbon nanotubes also possess intriguing elastic properties. The average value of the Young's modulus (elastic modulus) of SWNTs is several times larger than that of diamond¹⁰, making them the strongest known structures.

Energy and Environmental Applications

Sorbent-based processes for gas storage, separation, and purification have been the subjects of many industrial research and development studies during the past 50 years. This field recently has expanded to explore the potential use of carbon nanotubes for energy and environmental applications.

Hydrogen Storage. The potential use of carbon nanotubes in H_2 storage is receiving considerable interest worldwide because materials that can store large amounts of hydrogen under practical conditions are desirable for emerging fuel-cell-powered vehicles. SWNTs were shown to have the potential of storing up to 4.2 wt % of H_2 at room temperature and at a pressure of about 10 megapascals⁶. Reducing the pressure to 1 atm released over 78% of the gas adsorbed, indicating reversibility of operation. Adsorption capacities as high as 8 wt% at room temperature and moderate pressures have been reported for SWNTs¹¹. Other researchers, however, dispute these results¹¹.

According to one study, SWNTs have larger capacity for H_2 storage than MWNTs¹². It was revealed that H_2 storage capacity increases linearly with diameter of the tube for SWNTs, whereas it is independent of diameter for MWNTs. Additionally, this study concluded that H_2 was adsorbed on sites located on both outside and inside surfaces (walls) of SWNTs, and in the empty spaces inside the SWNTs. In contrast, only the outside surfaces of concentric shells of MWNTs adsorbed H_2 .

A recent study concluded that adsorption sites for well-aligned bundles of MWNTs are on the outside surfaces and in the interstitial channels between closely packed carbon nanotubes¹³. The adsorption data indicated that well-aligned bundles of MWNTs were capable of storing up to 3.5 wt % H_2 , about seven times larger than the amount observed for randomly oriented MWNTs.

Environmental Applications. Research studies in this field have primarily focused on the use of carbon nanotubes in two categories: as novel sorbents for gas and vapor, and as novel materials for development of gas sensors.

The first environmental study evaluated adsorption of trace concentrations (ppb level) of dioxins present in air on MWNTs¹⁴. MWNTs prepared by the methane CVD method were subjected to a

purification process that involved HNO_3 leaching and air treatment at 400 °C. The MWNTs had a N_2 -BET surface area of 155 m^2/g and contained pores ranging from 2.5 to 30 nm. Dioxin adsorption was studied using the temperature-programmed desorption (TPD) method. The data were analyzed using the Langmuir adsorption model. It was concluded that in low-concentration regimes, MWNTs had 10^{34} greater capacity for adsorption of dioxins than a commercial activated carbon tested under comparable experimental conditions.

The second study involved adsorption of NO , SO_2 and CO_2 on MWNTs¹⁵. N_2 -BET surface area and pore volume of the MWNTs were 462 m^2/g and 0.42 cm^3/gm , respectively. MWNTs had a high adsorption capacity for NO , a moderate capacity for SO_2 , and a low capacity for CO_2 . It was revealed that MWNTs had 36 times greater NO adsorption capacity than FeOOH -impregnated activated carbon fiber, which is one of the best-known adsorbents for NO . FTIR examination revealed the presence of NO , NO_2 and N_2O_4 species on the carbon nanotubes that were exposed to NO . Further, it was shown that NO_x desorption was reversible at temperatures below 300 °C.

Electrical transport properties of carbon nanotubes are very sensitive to surface modifications, such as local structural defects, and the presence of adsorbed species on the surface. These properties make carbon nanotubes ideal materials for developing gas sensors. The possibility of using an individual SWNT to develop molecular level sensors for gases such as NO_2 and NH_3 was recently reported¹⁶. Experiments conducted using semiconducting SWNTs (S-SWNT) showed that exposing an individual S-SWNT to 200 ppmv of NO_2 sharply reduced the electrical resistance by three orders of magnitude in less than 10 seconds. Similar experiments conducted for NH_3 indicated an opposite trend in electrical resistance of S-SWNT. Exposing an individual S-SWNT to 1% of NH_3 increased electrical resistance by two orders of magnitude in less than two minutes. It was postulated that unlike conventional NO_2 and NH_3 sensors, which operate only at temperatures above 250 °C, sensors based on carbon nanotubes could operate at ambient temperatures and offer several advantages including reversibility, higher sensitivity, and faster response time.

Another study recently explored the possibility of using MWNTs as an active sensing element for capacitive- and resistance-based sensors for detection of water vapor, NH_3 , CO and CO_2 ¹⁷. MWNT-based sensors were very sensitive to water vapor and NH_3 adsorption. Adsorption of water vapor was reversible and that of the NH_3 was not reversible.

Adsorption of Other Gases. The potential use of nanotubes for environmental applications has only recently been explored. Studies using carbon nanotubes for adsorbing various other gases, such as N_2 , O_2 , and CH_4 , have revealed many other aspects of gas adsorption on these materials. In these studies, experimental and computer simulation techniques were employed to explore the microporous structures of carbon nanotubes and to show the effects of the structure, configuration, and availability of inside and outside surfaces of carbon nanotubes on gas adsorption. Adsorption experiments using N_2 and O_2 showed that heat treatment in air at 350 °C opened the ends of carbon nanotubes and resulted in over two times increase in adsorption capacity⁸. The study hypothesized that adsorption took place on the outside surface of closed-ended nanotubes. However, when the ends were open gas molecules were adsorbed on the outside surface of the carbon nanotube only after the inside surface was saturated.

One study focused on the effects of purification and activation of carbon nanotubes on CH_4 adsorption mechanisms and wetting behavior of the adsorbed films¹⁸. This study concluded that capillary

condensation occurred inside the open-ended carbon nanotubes. This phenomenon was not observed for closed-ended nanotubes. Capillary condensation and wetting behavior are important factors for evaluating the use of carbon nanotubes for making nanowires, which can be prepared by filling internal cavities of carbon nanotubes with other materials such as lead¹⁹.

Another study showed the effect of various acid leaching techniques for preparing pure SWNTs²⁰. SWNTs treated with HCl had higher N_2 adsorption capacity than untreated SWNTs or HNO_3 -treated SWNTs. The researchers hypothesized that after the acid treatment the surfaces of carbon nanotubes contained various functional groups, which affected the adsorption capacity.

Aside from the structure and orientation of nanotubes, another important factor affecting the gas adsorption performance is the actual weight percentage (purity) of nanotubes in a sample. Preliminary experiments conducted by the authors of this paper suggest that N_2 -BET surface areas of carbon nanotubes containing 5 to 95 wt % of randomly oriented MWNT varied from 12 to 43 m^2/g , respectively. Surface areas of the samples containing 5 to 95 wt % of randomly oriented SWNTs varied from 86 to 460 m^2/g , respectively. These values present only the external surface areas of the carbon nanotubes because the samples were not subjected to any treatment for opening the ends of the carbon nanotubes. Interestingly, the surface area of the sample containing only 5% pure SWNTs was larger than that of the sample containing 95% MWNTs. This indicates that either MWNTs do not provide high surface area and/or the presence of carbon nanoparticles (soot) in the SWNTs contributed to the large surface area observed for this sample.

Future Trends

The remarkable physical and electronic properties of carbon nanotubes make these materials excellent candidates for a wide range of applications. Carbon nanotubes are excellent electron emitters and are currently used to manufacture cathode ray lighting elements²¹ and flat panel displays²². Carbon nanotubes are also being considered for energy production and storage e.g., development of nanotube microelectrodes²³, high-energy batteries²⁴, and H_2 storage at room temperature⁶. Applications based on the mechanical properties of nanotubes include development of MWNT reinforced composites²⁵, high sensitivity microbalances²⁶ and tweezers for nanoscale manipulations²⁷. General applications of carbon nanotubes include development of nano electronic components²⁸, use of a single MWNT attached to the end of a scanning probe microscope for high resolution imaging²⁹, and development of one-dimensional nano-wire by filling channels of MWNTs with lead¹⁹.

To date only limited progress has been made in determining the energy and environmental applications of carbon nanotubes. However, because of their unusual structures and properties, it is likely that research to develop carbon nanotube-based technologies for industrial applications in the energy and environmental fields will continue during the next decade.

Acknowledgement

This work was supported by EPRI, under contract WO5755-3.

References

- (1) Iijima, S., *Nature*, **1991**, 354, 56.
- (2) Ebbesen, T.W., P.M. Ajayan, *Nature*, **1992**, 358, 220.
- (3) Thess, A., R. Lee, R.E Smalley, *Science*, **1996**, 273, 483.
- (4) Bethune, D.S., C.H. Kiang, M. DeVries, G. Gorman, R. Savoy, J. Vazquez, R. Beyers, *Nature*, **1993**, 363, 605.
- (5) Kong, J., A.M. Cassell, H. Dai, *Chemical Physics Letters*, **1998**, 292, 567.
- (6) Liu, C., Y.Y. Fan, M. Liu, H.T. Cong, H.M. Cheng, M.S.

- Dresselhaus, *Science*, **1999**, 286, 1127.
- (7) Liu, J., A.G. Rinzler, H. Dia, J.H. Hafner, R.K. Bradley, P.J. Boul, A. Lu, T. Iversen, K. Shelimov, C.B. Huffman, F. Rodriguez, Y.S. Shon, T.R. Lee, D.T. Colbert, R.E. Smalley, *Science*, **1998**, 280, 1253.
 - (8) Fujiwara, A., K. Ishji, H. Suematsu, H. Kataura, Y. Maniwa, S. Suzuki, Y. Achiba, *Chemical Physics Letters*, **2001**, **336**, 205.
 - (9) Saito, R., M. Fujita, G. Dresselhaus, M.S. Dresselhaus, *Applied Physics Letters*, **1992**, 60, 2204.
 - (10) Lu, J.P., *Physical Review Letters*, **1997**, 79, 1297.
 - (11) *Chemical and Engineering News*, January 14, **2002**, pp 25-28.
 - (12) Lee, S.M., K.S. Park, Y.C. Choi et al., *Synthetic Metals*, **2000**, 113, 209.
 - (13) Zhu, H., A. Cao, X. Li, C. Xu, Z. Mao, D. Ruan, J. Liang, D. Wu, *Applied Surface science*, **2001**, 178, 50.
 - (14) Long, R.Q., R.T. Yang, *Journal of American Chemical Society*, **2001**, 123, 2058.
 - (15) Long, R.Q., R.T. Yang, *Industrial and Engineering Chemistry Research*, **2001**, 40, 4288.
 - (16) Kong, J., N.R. Franklin, C. Zhou, M.G. Chapline, S. Peng, K. Cho, H. Dai, *Science*, **2000**, 287, 622.
 - (17) Varghese, O.K., P.D. Kichambre, D. Gong, K.G. Ong, E.C. Dickey, C.A. Grimes, *Sensors and Actuators (B)*, **2001**, 4074 (In press).
 - (18) Mackie, E.B., R.A. Wolfson, L.M. Arnold, K. Lafdi, A.D. Migone, *Langmuir*, **1997**, 13, 7197.
 - (19) Ajayan, P.M., S. Iijima, *Nature*, **1993**, 361, 333.
 - (20) Eswaramoorthy, M., R. Sen, C.N.R. Rao, *Chemical Physics Letters*, **1999**, 304, 207.
 - (21) Saito, Y., S. Uemura, K. Hamaguchi, *Japanese Journal of Applied Physics*, **1998**, 37, L346.
 - (22) Wang, Q.H., A.A. Setlur, J.M. Lauerhaas, J.Y. Dai, E.W. Seelig, R.H. Chang, *Applied Physics Letters*, **1998**, 72, 2912.
 - (23) Britto, P.J., K.S.V. Santhanam, P.M. Ajayan, *Bioelectrochemistry and Bioenergetics*, **1996**, 41, 121.
 - (24) Gao, B., A. Kelnhammes, X.P. Tang, C. Bower, Y. Wu, O. Zhou, *Chemical Physics Letters*, **1999**, 307, 153.
 - (25) Yakobson, B.I., C.J. Brabec, J. Bernholc, *Physics Review Letters*, **1996**, 76, 2511.
 - (26) Poncharal, P., Z.L. Wang, D. Ugarte, W.A. de Heer, *Science*, **1999**, 283, 1801.
 - (27) Kim, P., C.M. Lieber, *Science*, **1996**, 286, 483.
 - (28) Soh, H.T., C.F. Quate, A.F. Morpurgo, C.M. Marcus, J. Kong, H. Dai, *Applied Physics Letters*, **1999**, 75 (5), 627.
 - (29) Dai, H.J., J.H. Hafner, A.G. Rinzler, D.T. Colbert, R.E. Smalley, *Nature*, **1996**, 384, 147.
 - (30) Iijima, S., *Material Science and Engineering*, **1993**, 19, 172.
 - (31) Smalley, R.E., *Material Science and Engineering*, **1993**, 19, 1.

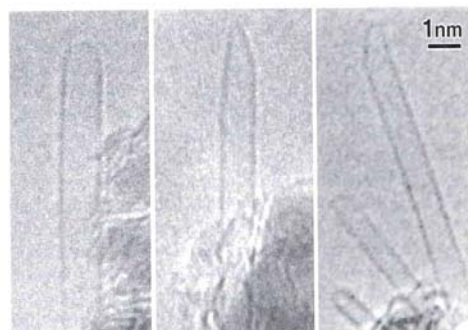


Figure 2. Single wall carbon nanotubes³⁰.

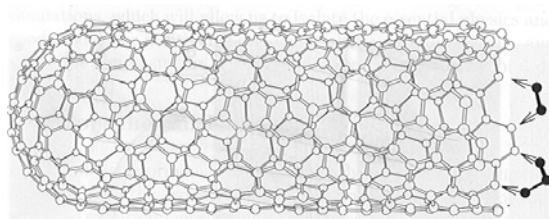


Figure 3. Growth mechanism of nanotubes³¹.

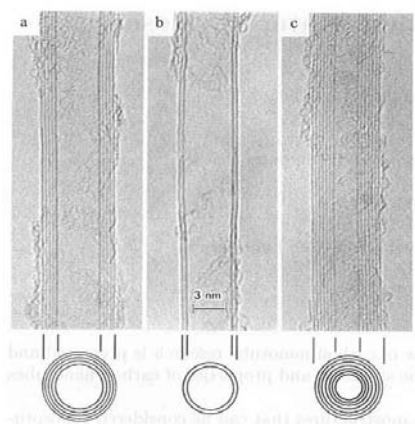


Figure 1. Multiwall carbon nanotubes¹.

HYDROGEN STORAGE IN CARBON NANOMATERIALS AT LOW TEMPERATURE

Bhabendra K. Pradhan*, Avetik R. Harutyunyan and Peter C. Ek-lund

¹Department of Physics, The Pennsylvania State University, University Park, PA16802, USA

ABSTRACT

We report (6 wt %) storage of H₂ at T=77 K in processed bundles of single-walled carbon nanotubes at P=2 atmospheres. The hydrogen storage isotherms are completely reversible. D₂ isotherms confirm this anomalous low-pressure adsorption and further reveal the effects of quantum mechanical zero point motion. We propose that our post-synthesis treatment of the sample not only improves access for hydrogen to the central pores within individual nanotubes, but also may create a roughened tube surface with an enhanced binding energy for hydrogen. Such an enhancement is needed to understand the strong adsorption at low pressure. We obtain an experimental isosteric heat $q_{st}=125 \pm 5$ meV for processed SWNT materials. We also studied H₂ adsorption in SWNTs produced by the High Pressure Carbonyl (HiPCo) process. We found up to ~2.5 wt% H₂ adsorbed on purified HiPCo material at 77K. The experimental isosteric heat for hydrogen storage in this material was found to be 76 ± 5 meV. High surface area activated carbon (SSA~ 1500 to 3200 m²/g) were found to exhibit a reasonably high hydrogen sorption values (~4 to 5 wt %) at 77 K and pressure 16 bar.

INTRODUCTION

The ever-growing demand for energy, mediated by the 1990 Clean Air Act and 1992 Energy Policy Act in the United States has pointed out the need for the developments of cleaner fuels and more efficient engines [1]. Because of a limited supply and adverse environmental problems, fossil fuels must be replaced with pollution-free fuels derived from renewable resources. For these reason, Hydrogen is an ideal candidate providing more energy than fossil fuel on a weight basis. Hydrogen storage in a light weight carbon material would therefore be particularly attractive. The physical adsorption of gases within the micropores (diameter < nm) of carbon materials has been actively studied for more than 50 years [2]. Many such carbon materials have been developed with very high experimental specific surface areas of $A_s \sim 1000$ to 3000 m²/g [3]. These materials tend to be disordered, with convoluted surfaces and predominately sp² C-C bonding. Despite these impressively large surface areas, these materials have not shown promise for hydrogen storage [2,3]. Recently reports of very high, reversible adsorption of molecular hydrogen in nano-carbon materials, i.e., pure carbon nanotubes, alkali-doped graphites, and pure and alkali-doped graphite nanofibers (GNFs) have generated tremendous interest in the research community, stimulating much experimental works and many theoretical studies worldwide[4-9]. In this study, we show that the wt% hydrogen adsorption depends on the post-synthesis treatment of the materials. SWNTs were carefully characterized with HRTEM, Raman scattering, N₂ adsorption isotherms.

EXPERIMENTAL

The SWNTs materials (arc-discharge derived: Ni-Y catalyzed) were obtained from Carboxex. This raw material was processed to remove amorphous and multi-shell carbon and residual catalyst. To accomplish this, the materials were first subjected to a high temperature oxidation under flow of dry air, then refluxed with mild mineral acid (HCl) in order to remove the exposed catalyst particles. The details of the purification is described elsewhere[10]. These samples were characterized by TEM, TPO, Raman scattering and N₂ adsorption isotherms. Transmission electron micrographs were observed on a JEOL JEM 1200EX microscope with electron beam energy of 120 kV. Raman spectra of the SWNTs samples were recorded in the Brewster-angle back scattering geometry for the following laser excitation lines: argon 514 nm (2.41 eV); krypton 647 nm (1.92 eV) and Nd:YAG 1064 nm (1.17 eV). Temperature programmed oxidation (TPO) of the samples were carried in gravimetric analyzer IGA-003 (Hidden Analytical Instruments). N₂ adsorption isotherms were measured at 77K using gravimetric analyzer IGA-003 (Hidden Analytical Instruments), prior to the adsorption, the sample was degassed under high vacuum (10⁻⁷ torr) at 500 K for overnight. The specific surface area and pores size were calculated by using BET and DR equations. Hydrogen uptake/storage measurements also carried out by using the same gravimetric sorption analyzer at 77K, which operate from UHV to 20 bar pressure range. An ultra high purity H₂ was used for the hydrogen uptake study using a oxygen/moisture trap on the delivery line. Prior to the hydrogen adsorption, the sample was degassed under high vacuum (10⁻⁸ torr) at 500-1223K for 12 h. Equilibrium at any pressure was achieved in less than 20 min, for each pressure point the time limit was set to be 30 min. In order to measure isosteric heat, we also measured hydrogen isotherm at 87 K. Most of the experiments were replicated to determine the reproducibility of the adsorption and desorption isotherms

RESULTS AND DISCUSSION

In Fig. 1a-d, we display high-resolution transmission electron microscopy (HRTEM) images for a sample of SWNT as-received (1a), and at successive processing steps (1b-d). For the as-received material, HRTEM images show primarily bundles of nanotubes and carbon-coated Ni-Y catalyst particles. To remove undesirable amorphous carbon that coats the SWNT bundles, we first selectively oxidized the amorphous carbon at T~350 °C in flowing dry air for 30 minutes. This oxidation also weakens the ordered sp² carbon coating passivating most of the metal catalyst particles in the soot, so that to 75 % to 90 % of the metal can be removed via a reflux in a mild mineral acid, i.e., 4.0 M HCl at T=130 °C for 18 h. On the basis of Raman scattering spectra and HRTEM images, it appears that HCl does not react with SWNT, but that HNO₃ does. This is important because the storage performance of the carbon sample is based on wt% uptake of hydrogen. Since our hydrogen storage experiments are conducted at room temperature and below, any metal in the sample can only decrease the wt% storage, as the metal cannot store (as hydride) at these temperatures.

A typical HRTEM image after a selective oxidation/HCl treatment (Fig. 1b) shows significant reduction in the catalyst residue (Ni-Y) content (to ~1.5 at % metal). The amorphous carbon that coats the bundle exterior has also been largely removed. A second sample was selectively oxidized, and then exposed to a considerably more aggressive oxidation in refluxing 2.6 M HNO₃

* email: bkp5@psu.edu

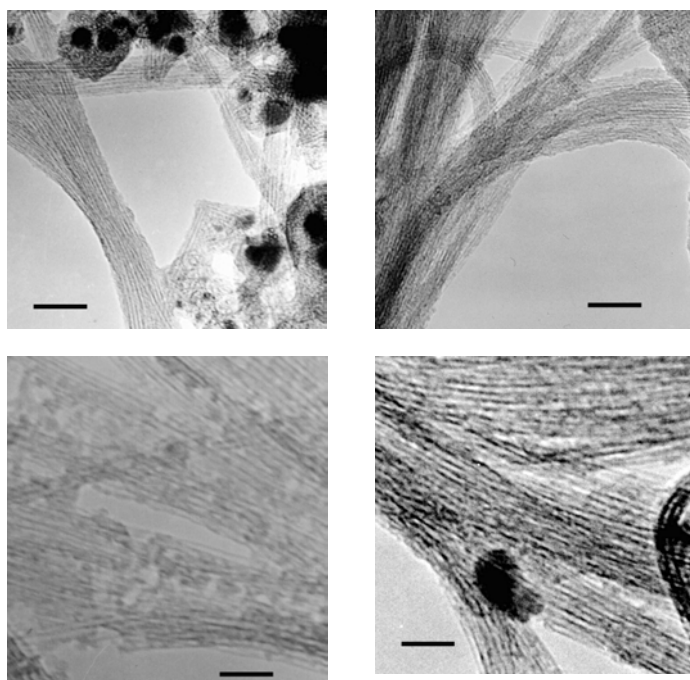


Fig. 1a-d. Transmission electron microscopy images of bundles of arc-derived carbon nanotubes at various stages of post synthesis processing: (a) as-received, (b) after selective oxidation/mild HCl reflux, (c) after selective oxidation followed by aggressive HNO₃ reflux, and (d) after step (c) followed by a heat treatment at 1000 °C in vacuum. Scale bar for (a) and (b) is 20 nm and for (c) and (d) is 10 nm.

at T=130 °C for 28 h. Although HNO₃ reflux removed almost all of the residual catalyst from the SWNT materials (i.e., less than 0.2 at % metal remained), significant damage to the tube wall (holes) can be seen in the HRTEM image (Fig. 1c). This extensive wall damage can be largely reversed by heating the material to 1000 °C in a high vacuum ($P \sim 10^{-8}$ Torr) (Fig. 1d), as was reported earlier [14]. The apparent damage in our sample is considerably higher than reported previously. We also examined samples for H₂ storage that had received this HNO₃ reflux, and that were then vacuum annealed at low T (~300 °C, 12 hrs) or high T (1000 °C: 20hrs). Most of the functional groups attached to the tube ends and at wall defects, are expected to be desorbed in this 1000 °C vacuum treatment [14]. During 1000 °C anneals in our TGA apparatus, we observed sample weight losses in the range 5-45%, depending on the sample and its chemical treatment.

Figure 2 a-d also show Raman scattering spectra of these four sets of sample, taken at room temperature in the range 100 to 1700 cm⁻¹. Raman scattering is a sensitive probe of the structure and bonding in carbon materials, particularly, carbon nanotubes [12-13]. The spectra were excited with 1064 nm (Nd:Yag) laser radiation, which excites only the semi-conducting tubes via resonant Raman scattering [12]. The dominant spectral features include the low frequency radial breathing modes in the range ~150 to 200 cm⁻¹ and the higher frequency tangential displacement modes in the range 1500 to 1600 cm⁻¹ (Fig. 1a). The Raman-active radial breathing mode is the clear spectroscopic signature of the cylindrical seamless SWNT, and the diameter dependence of the mode frequency for tubes in the range 1.0 < d < 1.4 nm is known to be approximately $\omega_R = (224 \text{ cm}^{-1} \cdot \text{nm})/d(\text{nm}) \pm \Delta$, where $\Delta \sim 12 \text{ cm}^{-1}$

corrects for the tube-tube interaction within a bundle [12]. The radial mode frequency and line-width are particularly sensitive to C-atom disorder in the tube wall, and also to changes in the tube “bundling” brought about by post-synthesis treatment.

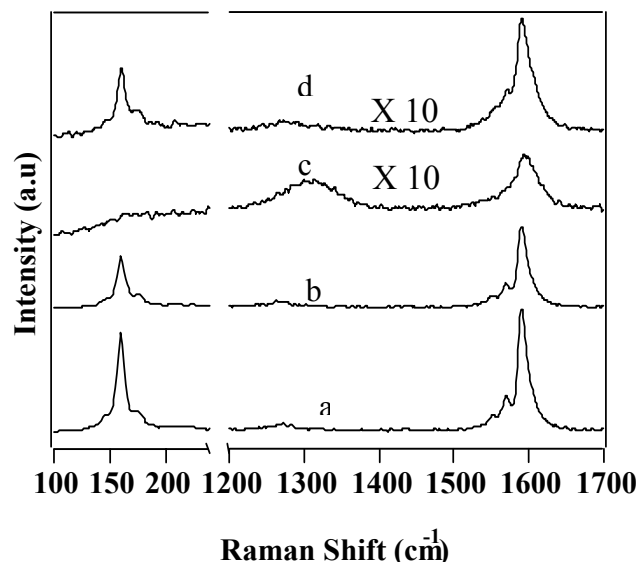


Fig. 2a-d. Room temperature Raman spectra of bundles of arc-derived carbon nanotubes at various stages of post synthesis processing: (a) as-received, (b) after selective oxidation/mild HCl reflux, (c) after selective oxidation followed by aggressive HNO₃ reflux, and (d) after step (c) followed by a heat treatment at 1000 °C in vacuum. The Raman spectra were taken using 1064 nm excitation.

The spectrum shown in Fig. 2a is typical of arc-derived material using a Ni-Y catalyst. In the as-delivered material the broad band centered near ~1300 cm⁻¹ is weak relative to the band at ~1600 cm⁻¹ (Fig. 2a). This band (at 1350 cm⁻¹), commonly called the D-band, has been observed in many sp²-bonded carbon materials and is associated with disorder (D) in the hexagonal carbon network. In the case of a multi-carbon phase SWNT material, the D-band could be identified either with amorphous sp² carbon present in nanoparticles, or in a thin coating on the nanotube bundle exterior. However, a D-band can also arise from disorder within the hexagonal carbon network of the nanotube wall itself. The fact that spectrum (a) has a weak D-band indicates that the sample contains a small amount of amorphous carbon and that the nanotube walls have a low number of defects. Chemical processing (particularly, in case of HNO₃), as shown below, was found to have a dramatic effect on the disorder in the system as seen via the D-band whose intensity correlates with the degree of disorder in the sp² network. Comparing the spectrum of Fig. 2a to that of Fig. 2b, we see that selective oxidation (Table 1), followed by HCl reflux, has no significant effect on the Raman spectrum of the as-prepared material. This was verified by a careful Lorentzian lineshape analysis, by comparison, for the full width at half maximum (FWHM) of the T Raman bands. No change in the FWHM following selective oxidation and HCl reflux was observed.

However, refluxing in the much more aggressive HNO_3 for 28 hrs alters the Raman spectrum dramatically (Fig. 2c): the D-band at $\sim 1350\text{ cm}^{-1}$ is much stronger; the tangential band (or G band) broadens significantly; and the radial band broadens to the point of near invisibility. The HNO_3 reflux has clearly damaged the SWNT, consistent with the TEM images. However, after this treatment we heat the sample *in situ* under vacuum to $\sim 250^\circ\text{C}$. This temperature should be sufficient to remove any residual HNO_3 as NO_x , so the intercalation compound has been essentially destroyed. The functionalization of the tube wall has occurred and does give rise to increased Raman line widths and to an increase in the D band intensity. This is the case because these functional groups do in fact induced disorder on the tube wall. However, it is important to consider the likely wall sites where these functional groups would attach themselves. These sites are at near missing C-atom sites in the tube walls, i.e., on the edges of holes in the tube wall. The disappearance of the radial band can be caused by the disorder in the tube wall via functional groups at the damage sites caused by the acid treatment. This explanation is associated with a softening and broadening of the Raman-active radial mode anticipated from the wall damage/functionalization. It was surprising to us that the final high-T anneal at 1000°C (~ 20 hrs) almost completely restores the Raman spectrum (Fig 2d) to that of the as-prepared (starting) material: The D-band is significantly reduced in intensity; the tangential bands have narrowed considerably; and the radial band regathers strength. The restoration of structural order to the SWNT is remarkable. Apparently, SWNTs can heal at significantly lower temperatures than needed for graphitization ($T > 2000^\circ\text{C}$). However, a careful line-shape analysis of the Raman bands after the vacuum anneal reveals that a residual line broadening associated with remnant disorder in the SWNT wall does indeed exist. A pervasive remnant disorder could enhance the binding energy of H_2 as discussed below.

The post-synthesis processing for each sample is summarized in Table 1, together with the at% metal residue and specific surface area (SSA) (m^2/g). The vacuum heat-treatment and the SSA measurements were made *in situ* in the TGA just prior to H_2 loading. The SSA values ($250\text{--}470\text{ m}^2/\text{g}$) are quite low compared to the maximum geometric surface area of a large bundle of open SWNTs $\sim 1350\text{ m}^2/\text{g}$. Furthermore, we find that the SSA does not correlate

Table 1. Sample history and hydrogen storage at 77 K and 1 atmosphere.

Sample	Sample History	SSA ⁴ (m^2/g)	Vac. Ann T($^\circ\text{C}$)/time (h)	Metal (%) ⁵
A	SWNTs	270	250/12	6
B	SO^1 , HCl^2	470	1000/20	1.5
C	SO^1 , HNO_3^3	250	1000/20	<0.2

¹ (SO) Selective Oxidation at 350°C for 30–45 min in flowing air (100 CCM).

² Reflux in 4M HCl at 120°C for 6 hr.

³ Reflux in 2.6 M HNO_3 at 130°C for 30 hr.

⁴ Specific Surface Area (BET) [15].

⁵ Determined by Temp. Prog. Oxid. (TPO).

with wt% H_2 storage. Although the theoretical SSA associated with the internal pore surface of a $\sim 1.4\text{ nm}$ diameter SWNT is $\sim 1350\text{ m}^2/\text{g}$, no one has yet reported values exceeding $\sim 400\text{ m}^2/\text{g}$ for SWNT materials. This indicates that the N_2 molecule is too large to gain access to many of these internal pores in a real mate-

rial, we conclude that the gateways must be smaller than the kinetic diameter of $\text{N}_2 \sim 0.36\text{ nm}$ [15]. As pointed out previously [14], this restricted gateway may be associated with the presence of carboxylic acid and other functional groups attached to carbon atoms present around holes in the tube walls or at open tube ends. The real gateways to the internal pore of the SWNT are, in many cases, apparently small enough to block entry of N_2 , but not H_2 .

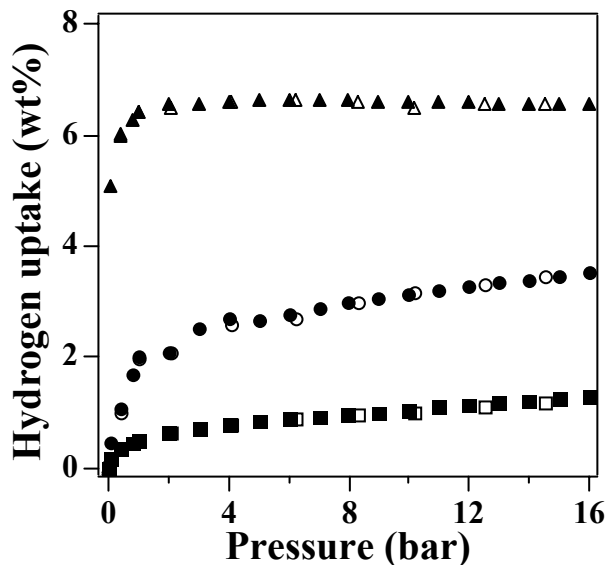


Fig. 3. Hydrogen isotherms ($T=77\text{ K}$) showing progressively better wt% H_2 storage with nanotube processing. From bottom to top, (a) the isotherms were taken on as-received material, (b) after selective oxidation/mild HCl reflux, followed by a heat treatment at 1000°C in vacuum (10^{-7} torr) for 20 hrs and (c) after selective oxidation/mild HNO_3 reflux, followed by a heat treatment at 1000°C in vacuum (10^{-7} torr) for 20 hrs.

In Fig. 3, we show low temperature isotherms for three samples labeled A, B and C (detail sample description in Table 1). The most remarkable feature of the H_2 storage isotherms of Fig. 3 is the very low H_2 overpressure required for significant storage in the processed SWNT material. Furthermore, the open symbols in the figure refer to adsorption, and the closed to desorption data. As can be seen in the figure, the adsorption/desorption data are completely retraceable. This rules out the adsorption at 77 K of gases such as H_2O and O_2 . We can compare our data for the HNO_3 treated material to that of Ye et al [8] who reported a maximum of $\sim 8\text{ wt}\%$ storage at $T=77$ and $\sim 100\text{ atm}$. Their H_2 over-pressures are a factor of 20 - 40 higher than required in our material to achieve similar storage. This remarkable change in the pressure scale suggests to us that the disorder we have created in the individual SWNT and bundling thereof may play an important role in enhancing the binding energy for H_2 adsorption.

Figure 4. compares the $T=77\text{ K}$ isotherms for hydrogen and deuterium (D_2) on the same sample. Data were first collected with H_2 . Next the sample was degassed in vacuum at 250°C for 12 hr and cooled to 77 K to collect the D_2 isotherm. The wt% storage for D_2 confirms the high storage observed for H_2 at low pressure in the same sample. It also reveals the effect of the quantum mechanical zero point motion on the storage. That is, since the

observed wt% (D_2) is more than twice the wt% (H_2), the storage is larger than the simple enhancement stemming from the larger isotopic mass of D_2 . The enhancement in the surface binding energy of deuterium over hydrogen is approximately 1/2 the mean kinetic energy of vibration ($\langle KE \rangle$) of the molecule in the pore. $\langle KE \rangle$ depends on the nature of the confinement of the molecule in the pore (e.g., interstitial channels in the bundle, internal pore of an individual nanotube), and thus the size of the isotope effect can give indirect information on pore volume and shape.

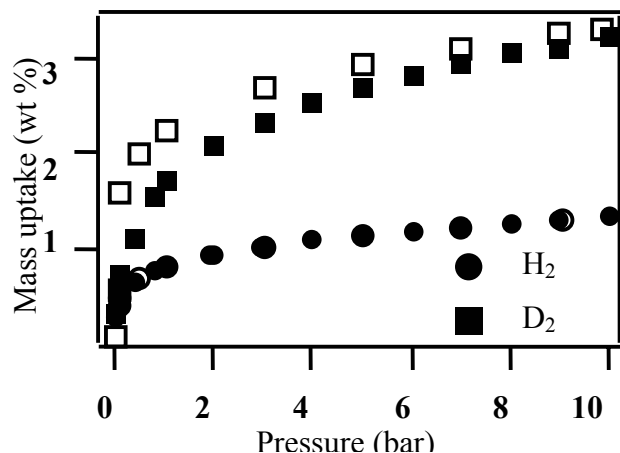


Figure 4. H_2 and D_2 adsorption isotherms on purified SWNTs at 77K, close symbols for adsorption and open symbol for desorption respectively.

The Isosteric heat of adsorption, $q_{st} = R d(\ln P) / d(1/T)$, depends upon the binding energy of the molecule to the surface; R is the gas constant and P is the pressure [15]. We can estimate q_{st} using data from two isotherms collected at $T=77$ and 87 K. For our highest storage sample (C), we find the isosteric heat to be 125 ± 5 meV. The isosteric heat bears a simple relation to the binding energy only within certain models or regimes of behavior. For example, a low density gas on a planar surface obeys $q_{st} = \langle E_z \rangle + (3/2) kT$, where $\langle E_z \rangle$ is the mean binding energy of surface-normal motion, computed quantum-mechanically. At $T=77$ K, $kT \sim 6$ meV, so in our case, we expect that the isosteric heat and the binding energy are nearly equal, independent of the details of the confinement. The magnitude of q_{st} substantially exceeds that expected for adsorption of H_2 to a planar sheet of graphite. This observation motivates a consideration of geometry-specific mechanisms for enhancing adsorption.

The end result of the aggressive HNO_3 treatment is a heavily damaged tube covered with holes of various sizes. This defective structure is far from equilibrium; the system can gain stability by partial healing the holes during the post-treatment anneal. The resulting tubes have irregular shapes and roughened surfaces. Atom transport during the healing must, of geometric necessity, produce pentagonal and heptagonal carbon rings. Pentagonal rings are particularly favored, as they most efficiently cap bonds on edge atoms bordering the holes. Such irregularities might open the small interstitial channels of pristine bundles into wider interstitial galleries, if the surface energy at the inter-tube contact does not dominate atomic rearrangement during annealing.

CONCLUSIONS

These results suggest an intimate connection between structural metastability and enhanced adsorption. A substrate near its global structural ground state has found a very efficient means to self-bind. If some component of the substrate-substrate interactions mimics the substrate-adsorbate interaction (e.g. graphene sheets bind to each other with an interaction mechanism not far removed from that of substrate-adsorbate physisorption), then a nearly-equilibrium self-bound structure will not be optimized for highest adsorption. Instead, a larger adsorption energy may occur in structures wherein the carbon substrate is unable to fully accrue the energetic advantages of self-binding. Our calculations suggest that the aggressive HNO_3 treatment pushes the material far from structural equilibrium by creating large holes in the tube walls. Partial healing during the subsequent anneal then spreads this disequilibrium more evenly throughout the structure and could yield a substrate with enhanced physisorption at low pressure, if the roughening is sufficiently pervasive.

REFERENCES

1. G.D. Berry, S. M. Aceves, *Energy & Fuels*, 12, 49, 1998.
2. S. Hynke, W. Fuller and J. Bentley, *Int. J. Hydrogen Energy*, 22, 601, 1997.
3. R. K. Agarwal, J. S. Noh, J. A. Schwarz and P. Davini, *Carbon*, 25, 219, 1987.
4. A. C. Dillon, K. M. Jones, T.A. Bekkedahl, C. H. Kiang, D. S. Bethune, and M. J. Heben, *Nature* 386, 377-379 (1997).
5. C. Liu, Y. Y. Fan, M. Liu, H. T. Cong, H. M. Cheng, and M. S. Dresselhaus, *Science*, 286, 1127-1129 (1999).
6. P. Chen, X. Wu, J. Lin, and K. L. Tan, *Science*, 285, 91-93 (1999).
7. A. Chambers, C. Park, R. T. K. Baker, and N. M. Rodriguez, *J. Phys. Chem.*, B 102, 4253-4256 (1998).
8. Y. Ye, C. C. Ahn, C. Witham, B. Fultz, J. Liu, A. G. Rinzler, D. Colbert, K. A. Smith, and R. E. Smalley, *Appl. Phys. Lett.* 74, 2307-2309 (1999).
9. M.S. Dresselhaus, K. A. Williams, and P. C. Eklund, *MRS Bull.*, 45, 1999.
10. B.K. Pradhan, A.R. Harutyunyan, P.C. Eklund, PSU Invention Disclosure No. 2001-2445, 2001.
11. CarboLex Inc; web site: www.carbolex.com.
12. M.S. Dresselhaus and P. C. Eklund, *Adv. In Phys.* 49, 705 (2000).
13. M.S. Dresselhaus, G. Dresselhaus, P. C. Eklund, *Science of Fullerenes and Carbon Nanotubes*, (Academic Press, San Diego, 1996).
14. D. B. Mawhinney et al. *Chem. Phys. Lett.*, 324, 213, 2000.
15. S. J. Gregg and K. S. W. Sing, *Adsorption, Surface Area and Porosity*, (Academic Press, 1982).

Acknowledgements: This work was supported by Honda R&D JAPAN.

OXYGEN ADSORPTION ON NITROGEN CONTAINING CARBON SURFACES

Alejandro Montoya[‡], Jorge O. Gil[‡], Fanor Mondragón[‡] and Thanh, N. Truong^{*}

[‡]Institute of Chemistry, University of Antioquia, Medellín, Colombia, A.A 1226, ^{*}Henry Eyring Center for Theoretical Chemistry, Department of Chemistry, University of Utah, Salt Lake City, Utah 84112

Introduction

The reaction of O₂ with carbonaceous surfaces has been widely studied due to its important application in industry. In general, O₂ is first chemisorbed on an electron-rich site of the carbon basal plane of graphite and then, it dissociates into oxygen atoms.^{1,2} Oxygen will diffuse on the surface until finds a structural defect to form covalent bonds. If temperature is appropriated, CO can be released to the gas phase. In char and open nanotubes structures, unsaturated carbon atoms at the edge of the carbon surface can form covalent bonds with oxygen. These sites can chemisorb directly molecular oxygen to form stable carbon-oxygen complexes with a high exothermicity.³ Several ab initio molecular studies have been performed on the O₂-carbon reaction. For instance, Kyotani et al⁴ studied the reaction of O₂ to the edge of a zigzag carbon structure at the DFT/HF level and found that the O₂ side-on adsorption mode is the most exothermic adsorption configuration. The same result was obtained by Zhu et al⁵ in the reaction of O₂ with single wall carbon nanotubes at the DFT level of theory and several carbon-oxygen complexes were found. Although studies on the O₂-carbon system abound, the reaction of O₂ with nitrogen containing carbonaceous surfaces is less known. The importance of nitrogen oxides in global warming and in stratospheric ozone depletion has motivated the study of NO and N₂O evolution in the combustion and gasification. Therefore, our objective is to carry out oxygen adsorption on nitrogen containing carbonaceous surfaces. As a case study, we compare the thermodynamics of this reaction with the O₂-carbon reaction. As a tool we employed electronic structure calculations to get insight into the nature of nitrogen-oxygen complexes.

Computational Details

We analyzed oxygen adsorptions to the edge of a carbon and a pyridine-type structure. The in-plane O₂ side-on approach was used to characterize the nature of carbon and nitrogen-oxygen complexes. Proposed carbon structures have several unsaturated carbon atoms at the edge of a graphene sheet to simulate chemisorption sites. A seven-six member ring structure in zigzag was used in both cases. Reactants, intermediates and products of reaction were fully optimized at the B3LYP density functional⁶ using the 6-31G(d) basis set. Electronic calculations were done using the Gaussian 98 program.⁷

Results and Discussion

Formation of Surface Oxygen Complexes. Initially, we studied the O₂-carbon reaction. Adsorptions on the carbon structure were carried out on the ground state. After approaching the O₂ molecule to the edge of the carbon model, two stable carbon-oxygen complexes were identified. First, the O₂ is adsorbed on two adjacent top sites forming a five member ring with an exothermicity of -112 kcal/mol, Figure 1a. Selected optimized geometrical parameters and Mulliken charges on selected atoms are shown in the same figure. As can be seen, a charge transfer from the carbon structure to the adsorbed gas molecule occurs. Therefore, due to the excess of Mulliken charge on the O₂, the O-O bond is activated and can be expanded from 1.50 to 2.25 Å to form two adjacent semiquinone

groups with an exothermicity of -49 kcal/mol, Figure 1b. This is the most stable carbon-oxygen group identified. The total O₂ adsorption process was found to be -161 kcal/mol exothermic. We found an energy barrier of 1.4 kcal/mol to open the five member ring and form the two semiquinone groups. Notice that the energy barrier is very low and the second intermediate is the most stable. Hence, concentration of the five member ring structure should be low compared with the semiquinone structure at high temperatures.

For adsorption of O₂ on the pyridine-type structure, calculations were also conducted on the ground state. Oxygen adsorption was carried out over a nitrogen atom located at the edge of the carbon model and three stable nitrogen-oxygen groups were identified. First, after approaching the O₂ molecule, an stable structure is found where the N-O distance is longer than the C-O bond distance as depicted in Figure 1c. The adsorption is -46 kcal/mol exothermic. Then, if the N-O distance is further decreased, a stronger bond is obtained forming a five member ring with and endothermicity of 24 kcal/mol, Figure 1d. We found an energy barrier of 25 kcal/mol for this process. Though the energy barrier is large, the total adsorption process is -22 kcal/mol exothermic. Next, the five member is activated by a charge transfer and the O-O bond can be expanded from 1.512 to 2.630 Å to form a semiquinone and a pyridine-N-oxide group with an exothermicity of -73 kcal/mol, Figure 1e. This is the most stable nitrogen-oxygen group identified. We found an energy barrier of 2.9 kcal/mol to open the five member ring. The total O₂ adsorption process was found to be -95.6 kcal/mol exothermic. Then, pyridine-N-oxide complex can be a plausible NO precursor because of the small energy barrier and high exothermicity.

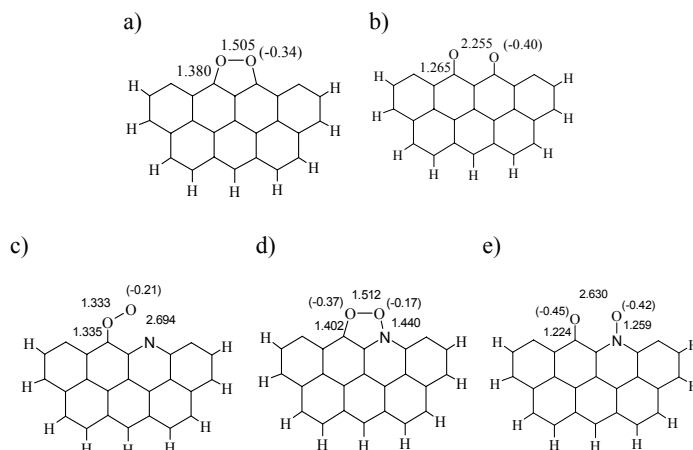


Figure 1. Adsorption of O₂ to the edge of a carbon and a pyridine-type structure. Structures (a) and (b) are intermediates on the O₂-carbon reaction. Structures (c) to (e) are intermediates on the O₂ pyridine-type reaction. Numbers are selected optimized bond lengths in Å. Numbers in parenthesis are Mulliken atomic charges in units of electrons.

NO and CO Desorption. Because of the unpaired electrons located at unsaturated carbon atoms representing the active sites, the molecular system has several low lying electronic states. As molecules desorb from the carbon surface, these electronic states can cross.⁸ Careful examinations of such crossing allow us to correctly determine the potential energy profile. In a previous study we analyzed the desorption mechanism and kinetics of NO from a “clean” carbon structure and in fact electronic crossing occurs as NO

desorb.⁹ The word “clean” is in the sense that no other oxygen groups different than those involved in the desorption process were present. Here, we studied the desorption of CO and NO in the presence of other oxygen groups making emphasis on the electronic states of the reactant molecules. Desorption is modeled from the most stable O₂ complexes obtained in the preceding section, namely the semiquinone and the pyridine-N-oxide structures, Figure 1b and 1e. The carbon and nitrogen atoms of the CO and NO groups, respectively, were pulled along the z axis and the remaining degrees of freedom of the carbonaceous surfaces are optimized, details of the procedure can be found elsewhere.⁸ It was found in both desorbing structures that the carbon surface is relaxed to let CO and NO break away and then closes up to form a five-member ring as seen in Figure 2a-b.

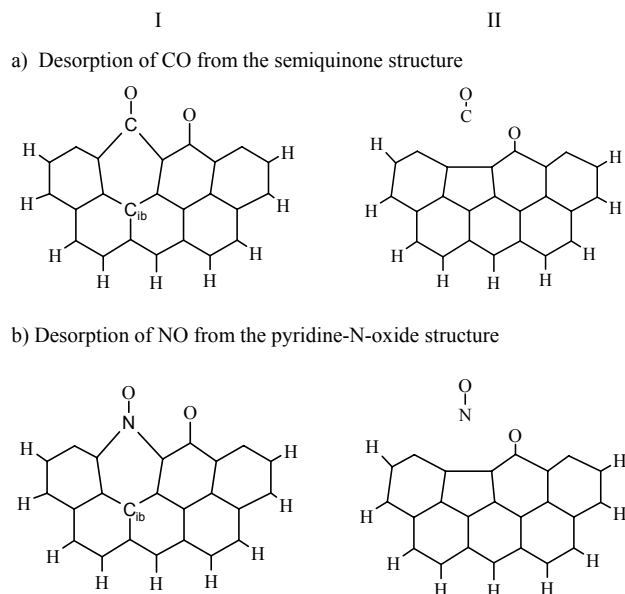


Figure 2. Desorption structures for CO and NO from a semiquinone and pyridine-N-oxide structures. I: The activated complex has a N-Cib and C-Cib distance of 3.8 Å. II: Reaction product.

The desorption energy has its maximum on the activated complex and it decreases as the desorbed specie distance increases from the carbon structure. As low lying electronic states can exist on the reactant molecules, the desorption energy barrier depends on the initial spin multiplicity selected. As comparison purposes, we have optimized the reactant and the activated complex at the two lowest electronic energies. Therefore, the energy difference between the two electronic states can be determined. Table 1 depicts the energy difference due to the change in spin multiplicity of the reactants and activated complexes. For reactants, it is seen that the energy difference between the two lowest electronic states is small. Then, one can expect that both electronic states are populated. As the desorbed molecule start to release, there is a change in the ground state from doublet to quartet and from singlet to triplet for CO and NO desorption structures, respectively. Notice that the energy difference in the activated complexes are larger than those of the reactants.

Table 1. Calculated Electronic Energy Difference for Reactants and Activated Complexes. *

oxygen complex		Reactant	Activated complex
Semiquinone	Ground state $\Delta E(\text{GS-CES})$	Doublet 5	Quartet 18
Pyridine-N-oxide	Ground state $\Delta E(\text{GS-CES})$	Singlet 0.02	Triplet 21

* $\Delta E(\text{GS-CES})$: Energy (kcal/mol) difference between the ground state and the closest electronic state

From the data in Table 1 it is seen that the spin multiplicity has an important effect on the desorption energy barrier. The difference can be as greater as 20 kcal/mol or higher. Electronic crossing not only is limited to clean carbon surfaces, it is also observed in the presence of other oxygen groups on the carbon surface and careful analysis should be done when considering the desorption patterns to obtain first principle kinetics data. Detailed analysis of the activation energies will be further discussed.

Conclusion

Using density functional theories, the nature and the dynamic transformation of different carbon and nitrogen-oxygen complexes were analyzed. pyridine-N-oxide structure seems to be a plausible NO precursor during combustion of carbonaceous materials.

Acknowledgment. T. N. Truong acknowledges financial support from NSF and University of Utah. F. Mondragón and A. Montoya want to thank the University of Antioquia for financial support of the project IN408CE. We also thank the Utah Center for High Performance computing for computer time support.

References

- (1) Beran, S.; Dubsy, J.; Slanina, Z. *Surf. Sci.* **1979**, 79, 39.
- (2) Chen, S. G.; Yang, R. T.; Kapteijn, F.; Moulijn, J. A. *Ind. Eng. Chem. Res.* **1993**, 32, 2835.
- (3) Kelemen, S. R.; Freund, H. *Carbon* **1985**, 23, 619.
- (4) Kyotani, T.; Tomita, A. *Prepr. Symp. - Am. Chem. Soc., Div. Fuel Chem.*, **2000**, 45(2), 221.
- (5) Zhu, X. Y.; Lee, S. M.; Lee, Y. H.; Frauenheim, T. *Phys. Rev. Lett.* **2000**, 85, 2757.
- (6) Becke, A. D. *J. Chem. Phys.* **1993**, 98, 5648.
- (7) Frisch, M. J, et al. *Gaussian 98*, Rev. A.9, Gaussian, Inc., Pittsburgh PA, **1998**.
- (8) Montoya, A.; Mondragón, F.; Truong, T. N. *J. Phys. Chem. A. In press* **2002**.
- (9) Montoya, A.; Mondragon, F.; Truong, T. N. *Fuel Process. Technol. In press* **2002**.

POROUS CARBONS DERIVED FROM PTFE DEFLUORINATED WITH ALKALI METALS

Osamu Tanaike, Noriko Yoshizawa, Hiroaki Hatori,
and Yoshio Yamada

National Institute of Advanced Industrial Science and Technology,
16-1 Onogawa, Tsukuba-shi, Ibaraki 305-8569 Japan

Soshi Shiraishi and Asao Oya

Gunma University, 1-5-1 Tenjin-cho, Kiryu, Gunma 376-8515 Japan

Introduction

Polytetrafluoroethylene(PTFE), a polymer having a polyethylene structure where all the hydrogen atoms are substituted by fluorine, is known to be changed to so-called carbyne-type carbon by its chemical defluorination^{1,2}. This carbyne structure consists of one-dimensional molecular chains of carbon with sp -hybrid orbital, and it is also known to be unstable structure. For example, the carbyne structure obtained from PTFE defluorinated by potassium metal was reported to be easily converted to stable sp^2 carbon in air³.

One of recent interesting attempts for carbyne is to utilize it as a raw material for new functional carbon materials because it is supposed that the carbyne structure is too unstable and easily transformed to other structures and forms of carbon. For example, carbon nanotubes, which are one of carbon materials most attracting attention recently, were reported to be synthesized via the carbyne structure from PTFE⁴.

Porous carbon materials are also known to be synthesized from PTFE via a carbyne structure⁵⁻⁸. In this case, a carbyne-like structure is formed and cross-linked around fluoride by-product during defluorination of PTFE, and the fluoride particles are removed by acid treatment to leave spaces as pores in the carbon matrix. Defluorination of PTFE is carried out by using various reducing agents, such as lithium amalgam^{5,6}, lithium metal⁷, lithium naphthalenide⁷, or potassium metal⁸. The produced porous carbons had both micro- and mesopores with a large surface area, but the porous structure of resultant carbons were often different from each other. We have synthesized porous carbons from PTFE using potassium metal vapor for defluorination and reported their porous structures previously⁸.

In this paper, various alkali metals were used for defluorination of PTFE and the effect on the porous structure of resulting carbons was investigated.

Experimental

Commercially available PTFE powder (MP1500J: DuPont-Mitsui Fluorochemical Co.Ltd.) with a polymerization degree of ca.10⁶, average diameter of 20 μ m and the specific surface area of 8-12m²/g was used as a raw material. Excess amount of lithium, sodium, potassium or rubidium metal and PTFE of 0.6 - 1g were sealed together in a glass tube under vacuum, and then heated at 473K in an oven for several days.

In this process, lithium and sodium metal were directly contacted with PTFE powder but potassium and rubidium needed to be separated from PTFE to react as the vapor because the latter metals were more reactive than the former ones and it was dangerous that molten potassium or rubidium strongly reacted with PTFE to ignite easily. Lithium and sodium, on the other hand, contacted with PTFE without ignition in this temperature range of defluorination. The black color products were taken out from the tube slowly and exposed to air for a while, and then washed by water and immersed in 0.1M HCl aqueous solution for two days to remove alkali metal

fluorides. After the product had been dried thoroughly at 383K in vacuum, nitrogen adsorption/desorption isotherms were measured at 77K. Transmission Electron Microscopic (TEM) bright field images were also observed for the same products with an acceleration voltage of 200kV.

Results and Discussion

Pore Characterization by N₂ Adsorption. Nitrogen adsorption/desorption isotherms of the products from PTFE defluorinated by sodium(Na-PTFE), potassium(K-PTFE) and rubidium(Rb-PTFE) are shown in **Figure 1**, and their BET surface areas calculated using the isotherms in **Figure 1** are summarized in **Table 1**. Lithium metal did not react with PTFE at 473K and

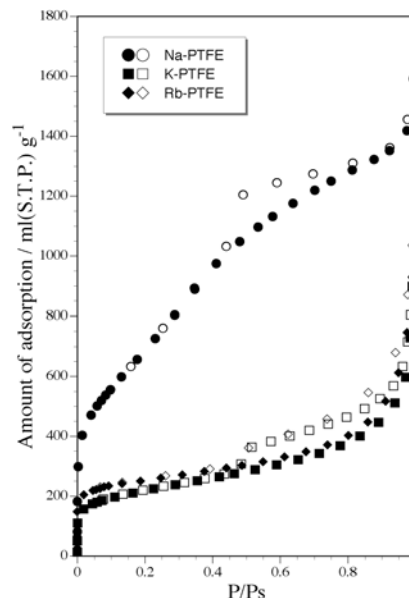


Figure 1. Nitrogen adsorption(closed marks) and desorption (opened marks) isotherms of Na-, K- and Rb-PTFE carbons measured at 77K.

Table 1. BET Specific Surface Areas of Resultant Porous Carbons Using Various Alkali Metals.

Sample	BET specific surface area (m ² /g)
Na-PTFE	2225
K-PTFE	784
Rb-PTFE	898

the defluorination by lithium was impossible. Since all three isotherms in **Figure 1** belong to type IV in the IUPAC classification, mesoporous carbons⁹ were found to be synthesized in all cases.

On the other hand, micropores also developed in the carbons because of a large amount of nitrogen adsorbed at very low relative pressure. When sodium metal was used for defluorination of PTFE, a remarkable isotherm curve was obtained, having a characteristic steep slope line in the relative pressure range 0.1 - 0.4 and a large BET surface area, in contrast to the other two. When potassium metal was used instead, a quite similar isotherm and BET surface

area which we have already reported⁸ were obtained. The reaction with rubidium showed a similar isotherm to that of potassium and the BET surface area slightly increased but it is not much different from potassium compared with sodium. Pore size distribution curves of the three porous carbons defluorinated by Na, K, and Rb calculated from the adsorption branches of each isotherm in **Figure 1** by Dollimore-Heal method^{10,11}, are shown in **Figure 2**. The curve of Na-PTFE has a clear large peak of pore size in 2-3nm which is mesopore range quite near to micropore, while those of K- and Rb-PTFE have no large peak in the mesopore range. These results show that all three carbons, Na-, K- and Rb-PTFE have micropores and mesopores, but only Na-PTFE has a large amount of additional mesopores with a diameter of 2-3nm which makes it comparable with other mesoporous materials, such as mesoporous silica, and some of them have been often given similar N₂ adsorption results to Na-PTFE^{12,13}.

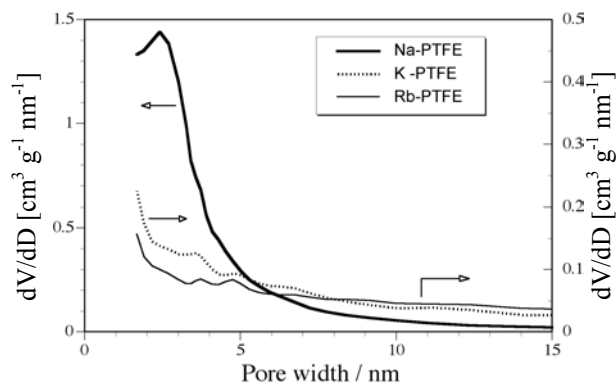


Figure 2. Pore size distribution curves of Na, K- and Rb-PTFE carbons calculated from the adsorption branches in **Figure 1** by Dollimore-Heal method.

TEM Observation. TEM images of Na- and K-PTFE carbons show particles like “foam” containing many circular pore images with diameters of less than 10nm. Since these pores are imaged like round pore entrances, these carbons from PTFE seem to have a three-dimensional network of spherical mesopores, which are the spaces left after fluoride particles were removed. However, there was a tendency that the size of the pores was smaller and the walls of pores were thinner for Na-PTFE than for K-PTFE. Since the walls of the pores were carbon made from PTFE via carbyne, it is supposed that sodium fluoride particles formed during defluorination of PTFE were dispersed better in PTFE than potassium fluoride. Such small particles of sodium fluoride well dispersed in the carbon matrix seem to cause the formation of large amounts of pores with a diameter of 2-3nm and thinner pore walls which develop the porosity of Na-PTFE with a large surface area.

Conclusions

The pore structure of carbons obtained from PTFE via a carbyne structure was found to be strongly governed by alkali metal species used for defluorination of PTFE. This seems to be caused by the dispersion state of alkali metal fluoride particles in PTFE during defluorination due to the different reactivity of each alkali metals with PTFE. Using sodium, which is less reactive with PTFE than potassium and rubidium, resulted in the formation of well developed mesopores with the size range of 2-3 nm, which is near to micropores. These characteristic porous carbons using alkali metals for defluorination of PTFE, particularly using sodium, are expected to

excel in some applications which need mesopores, such as electric double layer capacitance.

Acknowledgement. Part of this work is supported by a grant-in aid for “Research for the Future” Program from the Japan Society for the Promotion of Science.

References

- 1 Heimann, R.B.; Evsyukov, S.E.; Kavan, L., In *Carbyne and Carbynoid Structure, Physics and Chemistry of Materials with Low-dimensional Structures*, Vol. 21, Dordrecht, Kluwer Academic Publication, 1999.
- 2 Kavan, L. *Chem. Rev.*, **1997**, 97, 3061-3082.
- 3 Soneda, Y.; Maruoka, K.; Nakano, M.; Akuzawa, N.; Yamada, Y., *Proc.ADC/FCT '99*, **1999**, 571.
- 4 Yasuda, A.; Kawase, N.; Matsui, T.; Shimidzu, T.; Yamaguchi, C.; Matui, H., *Reactive Funct. Polymers*, **1999**, 41, 13-19.
- 5 Jansta, J.; Dousek, F.P.; Patzelova, V., *Carbon*, **1975**, 13, 377-380.
- 6 Dousek, F.P.; Jansta, J.; Baldrian, J., *Carbon*, **1980**, 18, 13-20.
- 7 Shiraishi, S.; Kurihara, H.; Tsudubota, H.; Oya, A.; Soneda, Y.; Yamada, Y., *Electrochem. Solid-state Lett.*, **2001**, 4(1), A5-8.
- 8 Liang, T.T.; Yamada, Y.; Yoshizawa, N.; Shiraishi, S.; Oya, A., *Chem. Mater.*, **2001**, 13, 2933-2939.
- 9 Sing, K.S.W.; Everett, D.H.W.; Haul, R.A.W.; Moscou, L.; Pierotti, R.A.; Rouquerol, J.; Siemieniewska, T., *Pure and Appl. Chem.*, **1985**, 57(4), 603-619.
- 10 Dollimore, D.; Heal, G.R., *J. Applied Chem.*, **1964**, 14, 109-114.
- 11 Dollimore, D.; Heal, G.R., *J. Colloid Interface Sci.*, **1970**, 33(4), 508-519.
- 12 Setoguchi, Y.M.; Teraoka, Y.; Moriguchi, I.; Kagawa, S.; Tomonaga, N.; Yasutake, A.; Izumi, J., *J. Porous Mater.*, **1997**, 4(2), 129-134.
- 13 Sierra, L.; Guth, J.L., *Microporous and Mesoporous Mater.*, **1999**, 27(2/3), 243-253.

PROGRESS TOWARD CALCULATION OF CARBON GASIFICATION THERMAL RATE CONSTANTS

Terry J. Frankcombe and Sean C. Smith

Department of Chemistry
University of Queensland
St Lucia, Queensland, Australia

Introduction

The gasification of carbonaceous materials is an extremely important process in many applications. As such, there have been many efforts to computationally model the gasification over the past four or five decades. The simplest models assume that the oxidation of the carbon atoms occur on the surface of shrinking solid particles. More complex models take into account reaction on the walls of pores and the growth and evolution of the surface pore structure. More sophisticated still are the models reflecting the observed structure of coal chars—small graphitic layers irregularly stacked into crystallites. Good summaries of the existent models are given in Bhatia and Gupta¹ and Bhatia².

The emergence of models, which involve the microscopic details of the coal char, has raised the importance of understanding the microscopic gasification processes. While developments such as Yang's *unified mechanism* for carbon gasification reactions³ offer insight into the microscopic processes at work during gasification, the opportunity to more directly investigate the properties of the microscopic processes and calculate dynamic quantities such as rate constants is offered by molecular orbital theory.

Advanced molecular orbital theory has been used by several authors to investigate these reactions since the pioneering 1998 work of Chen and Yang^{4,5} which seems to have fixed a standard methodology for the investigation of these reactions. Montoya *et al.*⁶ made the important contribution that overcoming spin contamination is vital in obtaining accurate energies for graphenes, and that the B3LYP formulation does not suffer from excessive spin contamination.

Despite this attention, little progress has been made in elucidating reaction paths with sufficient detail to directly calculate rates of the various microscopic processes in order to compliment or validate gasification modelling. This study presents progress toward that goal.

Methodology

The main gasification reaction of interest in this work is the extraction of a carbon monoxide fragment from an initial state of a graphene with an oxygen atom chemisorbed onto a carbon atom in an exposed "zig-zag" edge site. The enthalpy change for the reaction is easily calculated from the energies (corrected for thermal effects) of the optimized initial state (graphene with chemisorbed oxygen) and the product state (graphene with CO removed plus the CO fragment). The B3LYP hybrid method was used as a compromise between accuracy and tractability. Calculations have been performed using the 3-21G, 3-21+G(d) and 6-31G(d) basis sets.

Essential for the application of transition state theory is the identification of the transition state (TS) for a reaction. For many reactions occurring over a reaction barrier the TS is the geometry corresponding to the highest energy along the minimum energy pathway (MEP), and this serves as a useful first approximation. Hence a major focus of this work is in identifying these saddle point TSs.

A useful way of searching out a MEP with molecular orbital theory calculations without explicitly integrating energy gradients involves first identifying a parameter of the geometry specification

likely to be a reasonable reaction coordinate for the reaction of interest. This coordinate can then be frozen at successively longer values (or shorter values for association reactions) and the remaining coordinates optimized. This manual stepping of the likely reaction coordinate allows the MEP to be followed at an arbitrary level of detail and can easily find unexpected changes in the MEP, particularly if symmetry constraints are relaxed.

Results

The main graphene used in this work has been a C₁₉H₈ molecule similar to that used in previous investigations. The carbon structure is arranged into five aromatic rings, as shown in figure 1. One side of the carbon structure is left exposed to simulate the reactive edge sites during gasification while the other edges are capped with hydrogen atoms in order to minimize truncation effects. In all the calculations reported here spin contamination was acceptably low, with the calculated $\langle S^2 \rangle$ differing from the exact $S(S+1)$ value by around 0.01%.

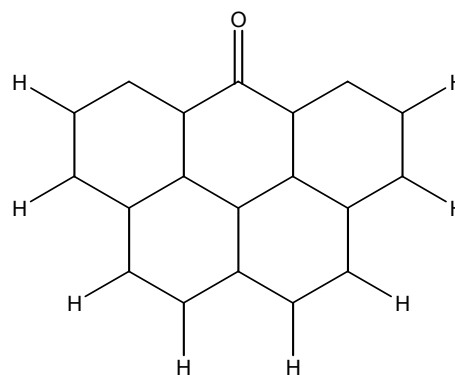


Figure 1. Model C₁₉H₈ graphene with oxygen atom chemisorbed onto the central bare zig-zag site

The ground state of the reactant state (after adding an oxygen atom to the central bare carbon site to make C₁₉H₈O) is the triplet state. However the potential minimum for the reactant in the singlet state is almost degenerate with the triplet, being calculated to be 0.18 kJ/mol higher in energy with the 3-21G and 3-21+G(d) basis sets and 0.076 kJ/mol higher in energy with the 6-31G(d) basis set. As has been pointed out by others⁷ this near degeneracy implies that both the singlet and triplet states need to be investigated as the singlet state will be significantly populated.

Straight gasification. The gasification reaction is assumed to take the CO fragment and pull it directly out of the graphene. A rather substantial complication of following this reaction path is that when all symmetry constraints are removed the actual MEP brings the CO fragment out of the plane of the remaining graphene to a position above the center of the remaining five atoms from the broken C₆ ring. The extent of the movement out of the plane is clearly an artifact of the single plane model being used as neighboring carbon planes in a real graphene would either prevent such motion or recapture the CO fragment. To counter this the geometry has been artificially restricted to C_{2v} or C_s symmetry, maintaining the CO fragment in the plane of the graphene. To follow the restricted MEP the reaction coordinate used was one of the Cartesian coordinates of the extracted carbon atom after aligning the graphene with the Cartesian axes: this single carbon atom coordinate is in effect the perpendicular distance between the extracted carbon atom and the remaining exposed edge. All other coordinates, including the position of the CO fragment relative to the broken C₆

ring, were allowed to relax. It was possible to freeze selected other coordinates to allow grid scanning of the potential.

For the triplet state, the MEP *does not* maintain the C_{2v} symmetry that other studies have suggested. C_{2v} symmetry is maintained as the CO fragment is moved the first 0.7 Å from its potential minimum position. Between 0.7 Å and 0.8 Å the potential well the CO fragment was following flattens and the fragment spills into an adjacent well. Following the adjacent, C_s symmetry well downhill leads back into the C_{2v} symmetry well. Extracting the CO fragment in a similar way on the singlet surface maintains C_{2v} symmetry throughout.

The singlet and triplet TSs are significantly different. While the triplet TS of C_s symmetry presents an energy barrier to reaction of around 500 kJ/mol, the singlet C_{2v} TS occurs at much lower energies, around 380 kJ/mol above the reactant state.

There are significant basis set effects on the calculated potential energy surfaces for both the singlet and triplet states. In the region of the triplet TS the three basis sets used produced significantly different energies, with the inclusion of diffuse functions in the 3-21+G(d) basis (generally required to accurately model such long-range, bond breaking processes) apparently responsible for the increase of the energy in the region of the TS by around 30 kJ/mol. In the singlet case the position of the TS (as measured by the distance of the extracted carbon atom from its reactant state position) changes from 1.10 Å for the 3-21G basis to 0.81 Å for the 6-31G(d) basis.

Multi-step mechanisms. While the direct gasification path is the most obvious, even in the small five-ring model being used here other paths exist. Fixing and stepping the Cartesian coordinate that moves the CO fragment across the exposed edge in a similar way to the direct extraction coordinate reveals that on the triplet surface, motion across the face quickly requires in excess of 500 kJ/mol of energy. However on the singlet surface such motion offers a viable alternate reaction path—possibly even a preferred path. Breaking one carbon-carbon bond and migrating the CO fragment to a carbonyl structure attached to an adjacent zig-zag site passes through a TS significantly lower in energy than the direct gasification barrier, being around 280 kJ/mol above the potential minimum. The migrated carbonyl structure is a stable species 90 kJ/mol above the potential minimum. Chen and Yang⁵ suggest that carbonyl should be significantly easier to gasify than the direct extraction, meaning that this may be an energetically preferred path.

Conclusion

This work supports the notion⁷ that while the ground state of the $C_{19}H_8O$ model molecule is technically a triplet, the very small energy gap to the singlet state and the availability of significantly lower energy reaction pathways on the singlet surface suggests that it is the singlet state that will be react. The near degeneracy of the singlet and triplet states will introduce a factor of two modification into the rate constants eventually calculated for the reaction on the singlet surface.

Basis set effects are very strong in the reasonably small basis sets used here. Adding diffuse functions seem to have a strong effect on the energy in the region of the TS. The position of the highest energy point along the calculated singlet MEP is changed by 30% with the move from the 3-21G basis to the 6-31G(d) basis.

The migration of the CO fragment onto adjacent edge sites has been examined here for the first time and is likely to compete effectively with direct gasification. While dynamical considerations will likely decide which process ultimately facilitates gasification, the existence of paths such as these need to be investigated further. Inter-plane interactions are likely to be important. The out-of-plane nature of the true TS for the single plane model examined here means that multi-plane models must be investigated to successfully model

bulk char edge reactions. Progress towards multi-plane models continues.

Acknowledgements. The authors would like to thank Bo Feng and Suresh Bhatia for useful discussions regarding this work. Computational resources supplied by the University of Queensland and the Australian Partnership for Advanced Computing National Facility.

References

- (1) Bhatia, S. K.; and Gupta, J. S. *Rev. Chem. Eng.*, **1992**, 8, 177.
- (2) Bhatia, S. K. *AIChE J.*, **1998**, 24, 2478.
- (3) Chen, S. G.; Yang, R. T.; Kaptejin, F.; and Moulijn, J. A. *Ind. Eng. Chem. Res.*, **1993**, 32, 2835.
- (4) Chen, N.; and Yang, R. T. *Carbon*, **1998**, 36, 1061.
- (5) Chen, N.; and Yang, R. T. *J. Phys. Chem. A*, **1998**, 102, 6348.
- (6) Montoya, A.; Truong, T. N.; and Sarofim, A. F. *J. Phys. Chem. A*, **2000**, 104, 6108.
- (7) Montoya, A.; Mondragón, F.; and Truong, T. N. Unpublished Results, **2002**.

Trends in Activated Carbon Products Past, Present, and Future

Neal E. Megonnell

Calgon Carbon Corporation
500 Calgon Carbon Drive
Pittsburgh, PA 15205

Introduction

Activated carbon has been utilized for purification of drinking water, wastewater, and various chemical products for many years. The end user of activated carbon products has become so familiar with the material, that activated carbon in general is being handled as a commodity product. For applications such as wastewater treatment and other bulk removal applications, the treatment of activated carbon as a commodity product is acceptable, however, applications such as methyl tertiary butyl ether (MTBE) adsorption from groundwater, and various catalytic processes have shown the need for more specialty carbons not supplied by all activated carbon vendors.

The commoditization of activated carbon has lead to the creation of many activated carbon “brokers” that supply a few types of activated carbon, provide very little to no technical support, and for the most part do not understand activated carbon or adsorption.

The more technically advanced activated carbon suppliers can and will provide the best product for the application technically and economically, and will also provide various technical resources such as adsorption modeling as well as the “non-standard” carbon products. MTBE remediation and hydrogen sulfide oxidation are two examples of applications where the more technically advanced carbon suppliers would offer the end user a more technically sound, cost effective option.

Experimental

Carbon Samples. The activated carbon samples used in these studies were commercially produced materials supplied by various carbon manufacturers and brokers. The activated carbon samples were tested on an as received basis, other than reduction of particle size, to accurately simulate full-scale usage.

Carbon Characterization. The activated carbon samples were characterized using standard activated carbon test methods as described by ASTM. Non-standard tests such as the Trace Capacity Number (TCN), Accelerated Column Test (ACT), and TACTIC^{1,2} were developed in-house by Calgon Carbon Corporation.

Results and Discussion

The removal of MTBE from groundwater has generated some debate in the activated carbon community specifically between carbon manufacturers and carbon brokers. Activated carbon produced from coconut shell has long been believed to be a superior product for removal of low molecular weight, water-soluble compounds such as MTBE and trihalomethanes (THMs). Unfortunately, no standard activated carbon test method can be utilized to determine the best activated carbon for these applications. As shown in Figure 1, iodine number shows a very poor correlation with MTBE adsorption capacity.

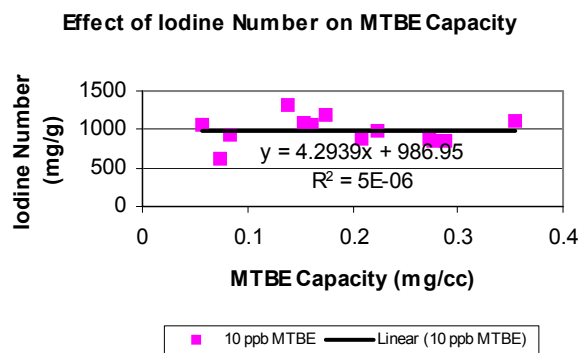


Figure 1. Correlation between iodine number and MTBE adsorption capacity

By fully characterizing an activated carbon via TACTIC and applying Polanyi adsorption theory^{3,4}, a new test method was developed to better predict the adsorption capacity of various activated carbons for applications such as MTBE and THMs. The new test method, the Trace Capacity Number, more accurately predicts the adsorption capacity of MTBE, Figure 2.

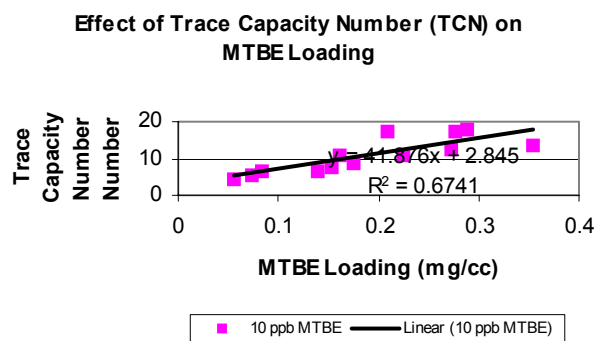


Figure 2. Correlation between Trace Capacity Number and MTBE adsorption capacity

The use of activated carbon for oxidation of hydrogen sulfide is another example of an application where advances have been made by the more technically advanced carbon suppliers. The standard ASTM test method for characterizing activated carbon for hydrogen sulfide capacity is conducted at 10,000 ppmV, well above any “real world” application. The standard activated carbons for this application have been materials impregnated with sodium or potassium hydroxide, or potassium iodide. These materials, although effective for hydrogen sulfide removal have several drawbacks, namely lower ignition temperature, reduced adsorption capacity for organic compounds, and the inability to safely regenerate or reactivate.

The Calgon Carbon Corporation Centaur HSV product offers all the advantages of the impregnated activated carbons, without the disadvantages. Recent studies have shown the ASTM test method has failed to account for a shift in reaction chemistry with hydrogen sulfide concentration. This has lead to unrealistic adsorption capacities as well as reactions that do not occur in the “real world”. The data in Figure 3 show the effect of the oxygen to hydrogen sulfide mole ratio on the formation of elemental sulfur as a reaction product.

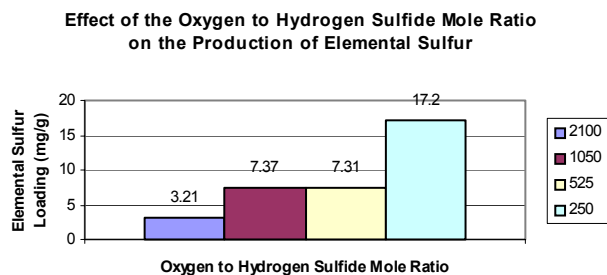


Figure 3. Effect of oxygen to hydrogen sulfide mole ratio on the formation of elemental sulfur

Both elemental sulfur and sulfuric acid are reaction products of the oxidation of hydrogen sulfide. The formation of sulfuric acid, which is water soluble, allows the activated carbon to be regenerated in situ with a simple water washing. The Centaur HSV product can be water regenerated many times, unlike the impregnated products, which must be disposed of in a landfill. The data in Figure 4 show the hydrogen sulfide capacity of Centaur HSV, IVP (sodium hydroxide impregnated), and Norit ROZ3 (potassium iodide impregnated) over various cycles.

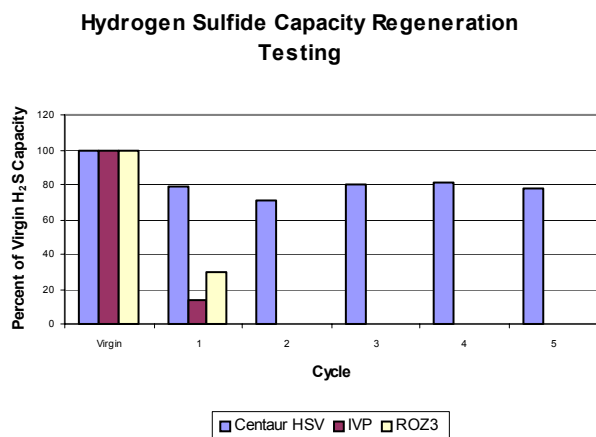


Figure 4. Hydrogen sulfide capacity after regeneration

The data show the effectiveness of the water regeneration for the Centaur HSV product, whereas the impregnated carbons would have been removed and replaced after the virgin cycle. Combining the regeneration with the higher ignition temperature and increase capacity for organic compounds, the Centaur HSV product is a more technically sound, cost effective option.

References

1. Trampusch, W. G., 211th ACS National Meeting, American Chemical Society Division of Fuel Chemistry, March 24-28, 1996, pp. 251-255.
2. Greenbank, M., Matviya, T. M., Trampusch, W. G., "Rapid Carbon Adsorption Characterization Using Temperature Programmed Adsorption and Desorption," 1991 Annual American Institute of Chemical Engineers (AIChE) Meeting, Los Angeles, CA, November 17-22, 1991. Fundamentals of Adsorption and Ion Exchange – I.

3. Manes, Milton, "The Polanyi Adsorption Potential Theory and Its Application to Adsorption from Water Solution onto Activated Carbon," Activated Carbon Adsorption of Organics from the Aqueous Phase, Volume 1, I.H. Suffet and M. J. McGuire, Ann Arbor Science, 1981. pp 43-64.
4. Wohleber, David A., PhD Thesis from Kent State University, "Application of Polanyi Theory to the Adsorption of Organic Liquids from Water onto Activated Carbon," March 1970.

WHAT (EXACTLY) IS ON THE EDGES OF GRAPHENE LAYERS IN CARBON: THE UNFOLDING STORY

Ljubisa R. Radovic* and Bradley Bockrath**

*The Pennsylvania State University, University Park, PA 16802
and

**U.S. Department of Energy, NETL, Pittsburgh, PA

Introduction

Knowledge of the chemical details of edge termination of a graphene sheet continues to be important in all applications of carbon materials (e.g., gasification reactivity, substituent effects in liquid-phase adsorption of aromatic compounds, and perhaps even enhanced gas adsorption potentials). The most recent evidence for this insufficiently recognized fact is the dramatic effect of "simple annealing of SWNT-based p-FETs in a vacuum" (1) on the behavior of carbon nanotubes as inter- and intramolecular logic gates. Perhaps surprisingly, this subject has been discussed in the literature only sporadically, most notably by C. A. Coulson and S. E. Stein. Today, when molecular-scale manipulation of the electronic properties of carbons is attracting much scientific attention and even becoming commercially viable, it is very important to be as specific as possible about the surface chemistry of edge carbon atoms. The common assumptions, that either all edge sites are saturated with heteroatoms or that the free edge sites are conventional (and thus very reactive) free radicals (2), do not appear to be justified (3). Modern quantum chemistry is increasingly providing the tools to confirm this. In this presentation we scrutinize the (relatively scant) literature and discuss our recent Gaussian98 (4) results to argue in favor of the following edge structures: ortho-benzynes at the armchair sites and carbene or m-benzynes at the zigzag sites. Unfortunately, we cannot be more specific in the case of zigzag sites. There is a very rich benzyne and carbene literature today, mostly theoretical but also experimental, so organic chemists will hopefully be comfortable with this proposal; and yet, many carbon scientists may be at least surprised.

The distribution of electron density at these sites is important because it can lead to quantitative indices of carbon atom (re)activity, and the litmus test here is to account for the reactivity differences between zigzag and armchair sites.

Overview of Theoretical Results

The distinction between armchair and zigzag sites is of both fundamental and practical importance; the ultimate goal is to be able to explain the experimental finding (5) that the latter are usually more reactive than the former.

The existence of unpaired σ electrons on armchair sites raises the possibility of the formation of a triple bond. Such a structure has indeed been proposed by Coulson (6), but it has been largely ignored in recent modeling studies of carbon electronic structure and reactivity. The fate of the unpaired σ electron on the zigzag sites is much more controversial (see Figure 1). Here again the most useful literature source is Coulson (6), who proposed the existence of a "divalent state based on s^2p^2 " hybridization. Use of the same model chemistry for the armchair sites – B3LYP/3-21G*/B3LYP/6-31G(d) – does not lead, however, to equally successful geometry optimization. Indeed, the results are very sensitive to the exact location of radical sites in the cluster shown below. However, the presence of preadsorbed oxygen does help to stabilize the zigzag structure, by analogy with the stability of 4-oxycyclohexa-2,5-dienylidene. The existence of the "in-plane σ pair," the somewhat

vague concept dating from the pioneering works of S. Mrozowski and P. L. Walker, is also discussed.

Implications for Carbon Reactivity

The most fundamental definition of reactivity is

$$R = (1/(1-X))(dX/dt) = \{\text{Site reactivity}\} \{\text{Number of reactive sites}\}$$

where X is carbon conversion. In our previous studies (7), as a first approximation, we equated site reactivity with $\Sigma(FV)_i$, where FV is the free valence index from simple Hückel molecular orbital theory. Subsequently, we estimated site reactivity using a Monte Carlo technique (8). Now, we are in a position to use a (unique?) set of fundamental reactivity indices, such as electron density (in the case of adsorption) and bond strength (in the case of desorption), to determine the above two reactivity parameters simultaneously; in such an approach, the number of reactive sites is automatically determined by the threshold level of site reactivity.

Acknowledgment. Partial financial support from the DOE FETC Fossil Energy Faculty Research Participation ORISE Program is gratefully acknowledged.

References

- (1) Derycke, V.; Martel, R.; Appenzeller, J.; and Avouris, P. *Nano Letters*, **2001**, 1 (9), 453.
- (2) Stein, S. E. *Acc. Chem. Res.* **1991**, 24, 350.
- (3) Menéndez, J. A.; Phillips, J.; Xia, B.; and Radovic, L. R. *Langmuir* **1996**, 12, 4404.
- (4) Frisch, A. E.; and Frisch, M. J. *Gaussian98 User's Reference*, 1998, Pittsburgh, Gaussian, Inc.
- (5) Thomas, J. M. In *Chem. Phys. Carbon*, Vol. 1 (P. L. Walker, Jr., Ed.), Marcel Dekker, 1965, 121-202.
- (6) Coulson, C. A. In *Fourth Conference on Carbon* (University of Buffalo), Pergamon Press, 1960, 215-219.
- (7) Kyotani, T.; Leon y Leon, C. A.; and Radovic, L. R. *AIChE J.* **1993**, 39, 1178.
- (8) Kyotani, T.; Ito, K.-I.; Tomita, A.; and Radovic, L. R. *AIChE J.* **1996**, 42, 2303.

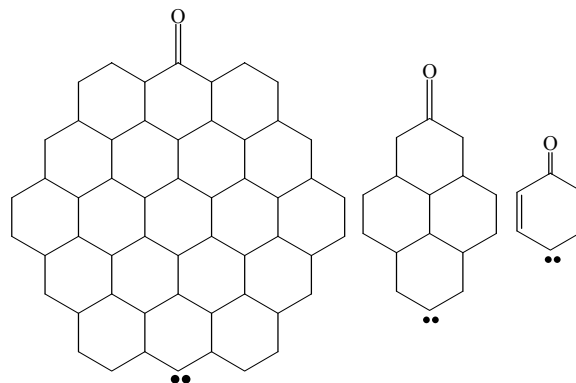


Figure 1. Model carbene structures for zigzag carbon atoms in different-size graphene layers of carbon materials.